Colour-Singlet Exchange and Tests of Models of Diffractive DIS

Jennifer C. Williams
Wadham College

Department of Physics · Theoretical Physics
University of Oxford

Thesis submitted in partial fulfillment of the requirements for the Degree of Doctor of Philosophy at the University of Oxford

· March 2000 ·

Abstract

Diffractive deep-inelastic scattering events observed at the HERA electron–proton collider are interpreted as an interaction involving a virtual photon scattering off a colour-singlet state within the proton. Models which attempt to describe the colour-singlet exchanged in diffractive interactions range from the purely phenomenological Donnachie-Landshoff form factor approach to the QCD-motivated gluon-exchange models and the scalar-pomeron model. It is important to find ways to test these models.

In this thesis colour-singlet exchange models of diffractive DIS are compared with cross section and structure function data from the H1 detector. H1 select diffractive data by requiring there to be a large angle between the forward proton direction and any other significant detector activity. This *pseudo-rapidity gap* cut extracts colour-singlet exchange events from the standard DIS data sample. For a wide range of the parameter space covered by the HERA experiments, however, the pseudo-rapidity gap cuts restrict the final-state phase space available for diffractive scattering. One consequence is that pseudo-rapidity gap cuts can be used to select diffractive events in which the colour-singlet only couples to off-shell partons. To leading order in the strong coupling constant, the diffractive final state consists of a quark–antiquark pair. Higher-order events include diffractive production of quark–antiquark–gluon states. In the region where pseudo-rapidity gap cuts restrict the accessible phase space, the cuts reject low transverse momentum quark–antiquark diffractive events. Pseudo-rapidity gap data selection cuts also allow selection of an enhanced 3-jet data sample.

The structure function and transverse momentum distribution data can be described by either a two-gluon model or by the Donnachie-Landshoff model, both models requiring a significant contribution from quark–antiquark–gluon diffractive final states to fit the full kinematic range of the diffractive data.

Further experiments and analyses are suggested to refine the studies of diffractive DIS and colour-singlet exchange models.

I am an idealist. I don't know where I'm going but I'm on the way.

Carl Sandburg

To Mum,
thanks for everything

Contents

List of Figures

List of Tables

Acknowledgments

Many thanks to Graham Ross for his guidance and supervision and for many enlightening conversations. Thanks also to John Ellis and to many people from H1, ZEUS, DESY Theory and the Oxford University Theoretical Physics and Particle and Nuclear Physics subdepartments for useful conversations and patient explanations.

I am grateful for financial support from a Commonwealth Scholarship (ref.NZD5500011), the New Zealand Vice Chancellors Committee for a Sir William Hartley Scholarship and also for additional support from the New Zealand Federation of University Women through an NZFUW Post Graduate Fellowship and a Sadie Balkind Scholarship. Additional travel assistance supported in part by The British Council DAAD Academic Research Collaboration Programme grant 757 is also gratefully acknowledged.

The work in this thesis benefited from visits to various conferences, workshops and institutes which I visited, all of which extended excellent hospitality.

Finally, many thanks all my friends and family for their support and encouragement. Special thanks to Peter Richardson and Paul Coe for reading this manuscript, and to Todd Huffman and Is Ridge without whom I might never have finished this work.

Publications and Original Work

The large pseudo-rapidity gap structure function analysis of Chap. 4 was done in collaboration with Graham Ross and John Ellis, and is published in [1]. The extension of the original Ellis-Ross calculations of phase space constraints [2] appears in full detail in App. A. The full analysis of the implications of pseudo-rapidity gap cuts and phase space restrictions was presented at workshops in Hamburg [3] (exchanged-quark virtuality constraints) and Berlin [4] (diffractive final-state transverse momentum constraints) and appears in Sects. 2.5 and A.3. Cross section calculations in Chaps. 3 and B are original work except where indicated in the text. Finally, Chap. 5 consists of original work which was published in [5].

Chapter 1

Introduction

1.1 Overview

This thesis is concerned with understanding the physical mechanism behind diffractive deep-inelastic scattering. The aim is to study models of the colour-singlet exchange underlying diffractive electron–proton scattering and to test these models against diffractive deep-inelastic scattering data. A novel aspect of this analysis is the detailed study of phase space effects due to data selection cuts, in particular, the requirement of a large pseudo-rapidity gap between the final-state proton and the diffractive final state. Imposing a large pseudo-rapidity gap cut to select diffractive events leads to an enhancement of the contribution of higher-order processes to the diffractive sample. Pseudo-rapidity gap cuts also remove a significant proportion of low transverse momentum dijet events from the diffractive data sample.

1.2 Deep-Inelastic Scattering and Diffractive DIS

In standard electron–proton deep-inelastic scattering (DIS), a high-energy photon emitted by the incoming electron is used to probe the structure of the proton. This virtual photon scatters off the partonic constituents of the proton producing an hadronic final state consisting of the proton remnant and an hadronic jet produced by the struck parton. Since the final state produced by the photon–parton interaction is connected to the proton remnant by a colour string the probability of there being a large angle devoid of significant hadronic activity, referred to as a pseudo-rapidity gap[1], about the proton remnant direction decreases exponentially with gap size. This is because the struck parton "dresses" its colour by radiating further partons which fill the gap between the proton remnant and the final-state parton. The proton structure function, $F_2(Q^2, x_{\rm Bj})$, describes the momentum distribution between valence and sea partons within the proton [6,7]. The proton structure function is defined in terms of the $e-P$ scattering cross section by

$$\frac{\mathrm{d}^2\sigma}{\mathrm{d}Q^2\,\mathrm{d}x_{\rm Bj}} = \frac{2\pi\alpha_{\rm em}^2}{x_{\rm Bj}Q^4}\left[\left(1+(1-y)^2\right)F_2(Q^2,x_{\rm Bj}) - y^2\,F_L(Q^2,x_{\rm Bj})\right], \tag{1.2.1}$$

where $x_{\rm Bj}$ describes the fraction of proton momentum carried by the struck quark and Q^2 is the negative four-momentum-squared of the virtual photon probe. The proton structure function can be expressed in terms of transverse and longitudinal components by

$$F_2(Q^2,x_{\rm Bj}) = F_T(Q^2,x_{\rm Bj}) + F_L(Q^2,x_{\rm Bj})\,. \tag{1.2.2}$$

At large Q^2 the proton structure function becomes approximately independent of the

[1] The kinematic parameters of standard and diffractive DIS are defined in Sects. 2.2 and 2.3.

photon virtuality, a property known as *scaling*. This indicates that the proton has a hard (partonic) substructure. Scaling violations at small $x_{\rm Bj}$ are due to the gluon content of the proton and higher-order events involving quarks.

The HERA collider at DESY in Hamburg collides 820 GeV protons and 27.5 GeV positrons or electrons[2]. This corresponds to a total centre-of-momentum (CMS) energy of $\sqrt{S_{\rm Tot}} \sim 300$ GeV, providing an excellent testing ground for QCD. HERA provides a fine probe of the proton structure with photons of higher energy than have been available before and smaller $x_{\rm Bj}$ than previously available. Small $x_{\rm Bj}$ allows access to the gluonic structure of the proton. Bunches of electrons (positrons) and protons collide inside the H1 [8] and ZEUS [9] detectors. Since the protons are much more energetic than the positrons, the remnants of the $e-P$ collisions are expected to be strongly peaked in the forward proton direction.

About 10 % of DIS events observed at HERA have a large empty region about the forward proton direction [10–13]. These gap events indicate a *diffractive* interaction in which the incident proton loses a small fraction of its energy, survives the interaction intact and either escapes undetected down the forward beam-pipe or is detected far down-stream from the interaction point [14] and the photon dissociates into an hadronic system. This hadronic system is observed in the H1 and ZEUS detectors. The number of gap events detected is approximately independent of gap size [10, 12]. In one H1 analysis [12], for example, the expectation from standard DIS for events with a gap about the forward proton direction of at least $\theta_{\rm min}$ was 12–53 events; in the data selected by requiring a large gap, however, there were 734 events. The presence of a gap indicates that the photon is probing a colour-singlet component within the proton, generically known as a "Pomeron".

Exchange of colour non-singlet states between the initial proton and the hadronic system produced by photon dissociation leads to a colour connection between the latter hadronic system and the proton remnant and tends to fill the gap. This is because the exchanged parton "dresses" its colour by emitting quark–antiquark pairs and gluons as it propagates. The need for a colourless exchange in diffractive DIS events is shown diagrammatically in Fig 1.1. As a result of soft colour dressing, the presence of a gap in standard DIS exchanges is expected to be exponentially suppressed as a function of gap size. Some gap events will occur due to random colour arrangements of the diffractive final state.

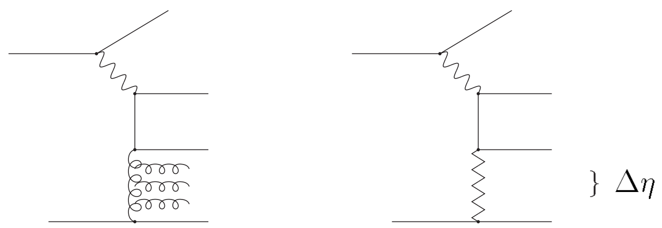

Figure 1.1: *Colour dressing and gap survival in diffractive DIS. The following symbols are used in these diagrams: straight lines represent leptons (top lines in these diagrams), quarks and antiquarks (lines in the centre) and protons (or their quark constituents) (bottom lines), wavy lines represent photons, "springs" represent gluons and the zig-zag lines are used to represent pomerons (or, more generally, the colour-singlet exchange in diffractive DIS).*

The fraction of gap events is independent of the four-momentum transfer from the

[2] Early HERA experiments used 26.7 GeV positrons and 820 GeV protons. Since August 1998 27.5 GeV electrons and 920 GeV protons have been used.

initial electron. That is, the diffractive events exhibit the scaling behaviour found in standard DIS [15]. This suggests that the colour singlet may have a partonic substructure. Diffractive DIS events can be extracted from the fully-inclusive DIS data sample by selecting events where the hadronic system observed in the detector is separated from the proton direction by a large gap [10–12, 16].

The leading-order contribution (to order α_s) diffractive colour-singlet exchange process is shown in Fig. 1.2. In this process the virtual photon dissociates into a quark–antiquark pair which interacts with the proton through the t-channel exchange of a colour-singlet state. This process is interpreted as the photon probing the quark structure of the pomeron. Two hadronic jets, separated from the forward proton direction and the scattered electron are detected. The proton (or low-mass excited state) either escapes undetected down the forward beam-pipe or is detected far down-stream from the interaction point [14]. The two jets result from the hadronization of the quark–antiquark pair, and the event is referred to as a "dijet" event. Higher-order processes include "3-jet" diffractive events, such as gluon Bremsstrahlung, Fig. 1.3(a), in which one of the diffractively-produced quarks radiates a gluon which may then be detected as a third hadronic jet (depending on the resolution of the detector and the proximity to the quark jets), and photon–gluon fusion, Fig. 1.3(b), which is interpreted as the photon probing the gluonic structure of the pomeron. Diffractive events in which the diffractive system contains 3 or more partons are referred to as "multi-jet" events.

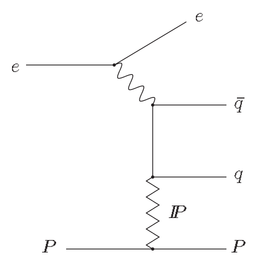

Figure 1.2: *Leading-order contribution to diffractive DIS. The exchanged colour-singlet state is denoted by* $I\!P$.

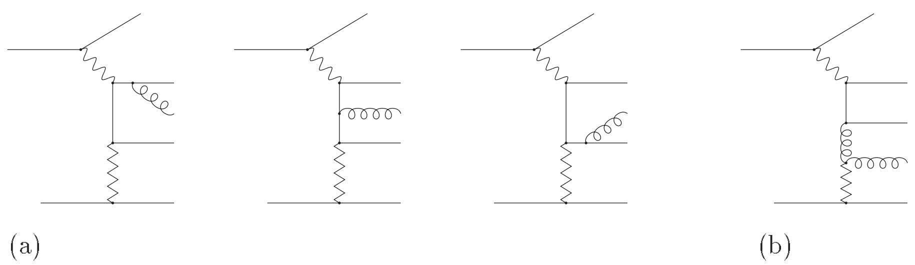

Figure 1.3: *QCD corrections to diffractive deep-inelastic scattering: (a) gluon Bremsstrahlung and (b) photon-gluon fusion.*

Diffractive scattering involves a small momentum transfer from the proton vertex and explores the interface between perturbative (high energy, short distance) physics and non-perturbative (low energy, long distance) physics. The former is well-described by QCD [17], while to describe the latter one requires Regge physics [18–20].

1.3 The Origins of Pomeron Exchange

Regge theory provides a framework in which to study high-energy scattering [18–20]. One of the central results of Regge analysis is that, at large CMS energies, s, the total scattering cross section can be described as a sum of powers of

$$\sigma_{\mathrm{Tot}} \sim s^{\alpha(0)-1}\,, \tag{1.3.1}$$

where the functions $\alpha(t)$ describe the positions of moving poles in the complex angular momentum plane. This result arises from a partial wave analysis of scattering amplitudes [20]. The poles, $\alpha(t)$, are known as Regge trajectories. The dominant contribution comes from the trajectory with the largest $\mathrm{Re}\,\alpha(t)$, the leading Regge trajectory. Contributions from subleading Reggeon exchanges become more important away from asymptotic energies.

The t-channel exchange of a Regge trajectory corresponds to s-channel exchanges of families of hadronic particles [20] apart from the pomeron trajectory, which does not correspond to any known particles, except possibly a glue-ball candidate [21].

For relativistic scattering the Regge trajectories are found to be linear functions of t. Most leading trajectories have a slope of approximately $1\,\mathrm{GeV}^{-2}$ and an intercept of $\alpha(0) \lesssim 0.6$. The exchange of Regge trajectories corresponding to known hadrons therefore leads to total cross sections which fall approximately as $1/\sqrt{s}$. The pomeron trajectory corresponds to the exchange of vacuum quantum numbers. It has a slope of $\alpha'_{I\!P} \sim 0.25\,\mathrm{GeV}^{-2}$ and an intercept of approximately 1.

The pomeron first emerged in experimental particle physics as an explanation for elastic and diffractive hadron–hadron scattering [22, 23]. In this model the exchange of a colour-singlet state with vacuum quantum numbers and with an approximately vector-like coupling to quarks was interpreted as the exchange of a pomeron Regge trajectory. In this interpretation the pomeron behaves like a photon except that it couples to quarks with even charge conjugation parity.

Donnachie and Landshoff [24–27] successfully fitted elastic and diffractive proton–proton and proton–antiproton scattering data with a simple Regge-inspired model of pomeron exchange. The total cross section for proton–(anti)proton scattering rises slowly with increasing CMS energy. The slow rise corresponds to the exchange of a Regge trajectory with an intercept slightly larger than 1. Since one or both of the protons emerges intact, no quantum numbers are exchanged in these interactions. This vacuum exchange was identified as the exchange of a pomeron trajectory.

Donnachie and Landshoff found the data to be well-described by a pomeron trajectory of

$$\alpha_{I\!P}(t) = 1.08 + 0.25t\,, \tag{1.3.2}$$

with a subleading Reggeon trajectory corresponding to ρ exchange with intercept $\alpha_{I\!R}(0) \approx 0.55$ and approximately unit slope. The pomeron–quark vertex is modelled with a point-like vector coupling, $\beta_0\bar{\psi}\gamma^\mu\psi$, with Dirac matrix γ^μ and coupling constant β_0. The coupling constant has inverse energy dimensions. The pomeron coupling has even charge conjugation parity; that is, the pomeron couples with equal sign to particles and their anti-particles.

1.4 Pseudo-Rapidity Gap Cuts

It is common to select diffractive electron–proton scattering events by requiring there to be a large angle about the forward proton direction in which there is no hadronic activity above a low-energy threshold. This angle is expressed in terms of pseudo-rapidity, which is defined in Eq. 2.3.1 in terms of laboratory scattering angles. Fig. 1.4 shows a typical pseudo-rapidity gap event [28]. In this figure the proton enters the detector from the right and there is a large angle about the forward proton direction with little detector activity. The incoming positron enters the detector from the left. The tracks indicate reconstructed paths of charged particles in the central tracking detector (CTD) and energy deposition in the electromagnetic and hadronic calorimeters is shown by light-shaded boxes. The scattered positron is visible in the backward electromagnetic calorimeter and the proton remnant escapes undetected down the forward beam pipe.

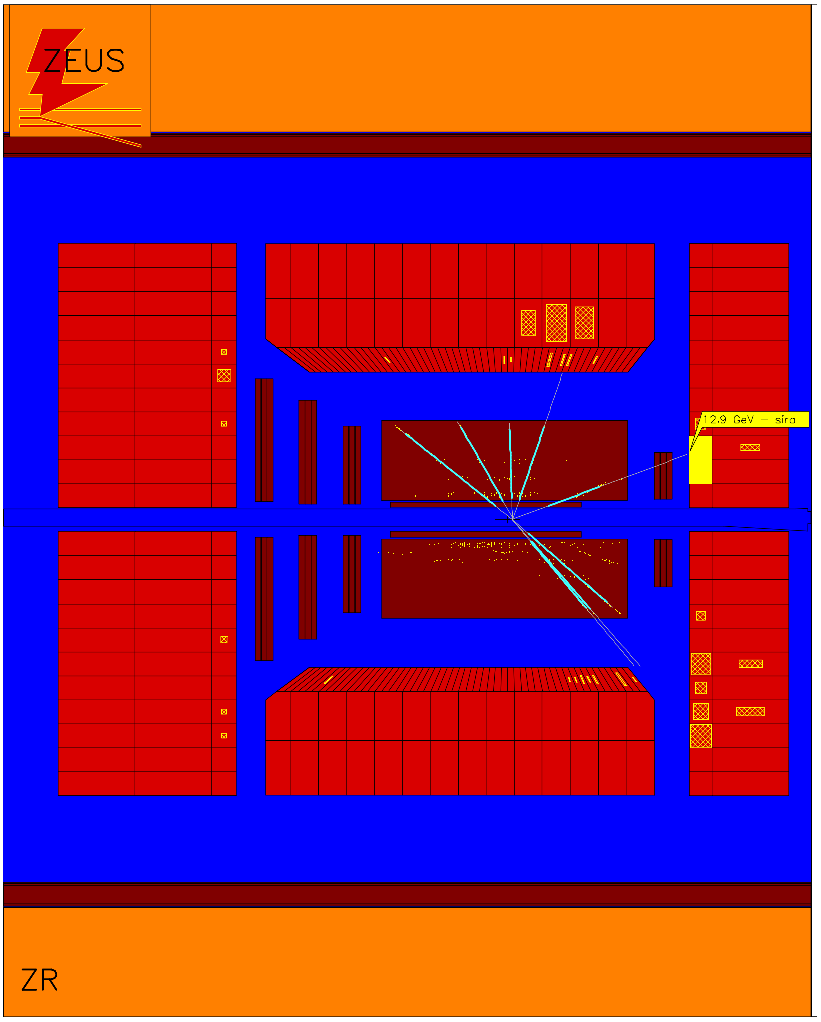

Figure 1.4: *ZEUS pseudo-rapidity gap diffractive DIS event [28]. In this event picture, an 820 GeV proton entering the ZEUS detector from the left collides with a right-moving 27.5 GeV positron. The tracks indicate reconstructed paths of charged particles in the central tracking detector. The resultant diffractively-produced hadronic system is separated from the forward proton direction by a region of pseudo-rapidity. The scattered positron is identified in the backward electromagnetic calorimeter.*

The need for a large pseudo-rapidity gap to select diffractive DIS events at HERA restricts the kinematically accessible phase space for a significant region of HERA parameter space. To understand the physics of diffractive DIS, it is important to understand the effect of data selection cuts so as to be able to distinguish physics effects from phase space effects.

Pseudo-rapidity gap cuts impose a stronger restriction on accessible dijet phase space than on 3-jet phase space and a large pseudo-rapidity gap sample, in which the cuts constrain the available phase space, is therefore expected to have proportionally more quark–antiquark–gluon events than the full diffractive data sample. Since the diffractive structure function, defined in Eq. 2.4.1 analogously to the proton structure function, is calculated by integrating the diffractive scattering cross section over the available final-state phase space, the diffractive structure function extracted after pseudo-rapidity gap cuts have been applied will be smaller than that extracted using other techniques such as leading proton detection. Since the phase space constraints are sensitive to the kinematic parameters of the event, such as exchanged photon virtuality, the magnitude of this reduction will vary across the kinematic parameter space. A further expected consequence of the phase space restrictions from pseudo-rapidity gap cuts is the breakdown of factorization of the diffractive structure function into a pomeron flux factor and a pomeron structure function.

There are several simple experiments that can be carried out to verify these predictions. The consequences of pseudo-rapidity gap cuts are discussed in detail in Chap. 2 and the proposed experiments are described in Chaps. 4 and 5.

1.5 Colour-Singlet Exchange Models

There are many models that attempt either to describe the physical structure of the colour-singlet exchanged in diffractive DIS or simply to parameterize its behaviour. The aim of this thesis is to distinguish between models of diffractive DIS by comparing them with large pseudo-rapidity gap diffractive DIS data.

Ingelman and Schlein [29] suggested treating the pomeron as an hadronic particle with constituent quarks and gluons. This is a "resolved-coupling" scheme in which the pomeron couples only to partons which are near mass shell. In this interpretation, the notion of a "pomeron structure function", analogous to the proton structure function, is well-defined and one can attempt to determine the partonic structure of the pomeron.

The simplest partonic model for pomeron exchange in diffractive DIS is one in which the pomeron constituents are two non-interacting gluons [30–41]. Another model for a resolved-coupling pomeron is single-gluon exchange [42,43]. In this model one gluon carries most of the pomeron momentum, but the pseudo-rapidity gap is preserved by subsequent soft-gluon exchanges. It is assumed that the soft exchanges do not affect the dynamics of the hard scattering. The full perturbative QCD approach to diffraction is found in the BFKL model [44,45] in which the pomeron is modelled by a ladder of interacting gluons.

Ellis *et al* [1,2] showed that the pseudo-rapidity cuts used to extract diffractive data reduce the available final-state phase space. In diagrams such as Figs. 1.2 and 1.3, only the direct pomeron–parton coupling contributions to the diffractive cross section are selected in some regions of HERA parameter space in pseudo-rapidity gap cut experiments, the resolved-coupling component being rejected by the data selection cuts.

An alternative approach to diffractive DIS allows for direct couplings between the pomeron and off-shell partons. Donnachie and Landshoff (D-L) [46,47] extended their successful pomeron description of hadron–hadron scattering to lepton–hadron diffractive DIS. In this model the diffractive interaction is assumed to proceed by the exchange of a vector-like pomeron with even charge conjugation parity. In order to reproduce the observed scaling of the diffractive DIS events, Donnachie and Landshoff included a *form factor* at the virtual quark–pomeron vertex. This suppresses contributions from events where the pomeron couples to large virtuality quarks. Ellis and Ross (E-R) [2] showed that the minimum pseudo-rapidity gap size of a diffractive event is sensitive to the virtuality of the partons coupling to the pomeron. They showed that a minimum gap size implies a minimum parton virtuality. This, combined with the relative insensitivity of the fraction of gap events to gap size observed at HERA [10,12], suggests that one must allow equal contributions to diffractive DIS from large-virtuality partons. To reconcile these results with a Donnachie-Landshoff-type model, Ellis and Ross suggested adopting a harder form factor which leads to a diffractive cross section with logarithmic dependence on parton virtuality. The Ellis-Ross form factor model leads to a pomeron structure function with logarithmic scaling violations. The simplest direct-coupling model is one in which the pomeron is described by a scalar exchange with point-like couplings to quarks and gluons [48]. This model scales without the need for a softening of the virtual parton–pomeron vertex.

The pomeron-exchange models described in detail in Chap. 3 and compared with diffractive DIS data in Chaps. 4 and 5 are: the Donnachie-Landshoff form factor model [46, 47], the Ellis-Ross form factor model [1, 2], a single-gluon exchange model, a scalar-pomeron model [48] and the Landshoff-Nachtmann two-gluon model [34, 35].

1.6 H1 Analysis of Diffractive DIS

Extending the successful QCD analysis of the proton structure function to diffractive DIS, H1 have attempted to determine the partonic content of the pomeron. The H1 analysis [15] assumes the Ingelman-Schlein picture of an hadronic pomeron and attempts to fit the structure function data with the diagrams of Figs. 1.2 and 1.3 (plus sub-leading Reggeon exchange contributions). Scaling violations of the diffractive structure function are used to determine the quark and gluon momentum distributions. The scaling violations in the diffractive data are fitted with a pomeron in which $80-90\,\%$ of the pomeron momentum is carried by a single gluon. This means that the boson–gluon fusion diagram of Fig. 1.3(b) provides the dominant contribution to diffractive DIS and the exchanged gluon carries almost all of the momentum. This anisotropic momentum distribution is similar to the single-gluon exchange model described in Sect. 3.4 in which the pomeron consists of one hard gluon and one or more soft gluons.

1.7 Comparison of Colour-Singlet Exchange Models with Large Pseudo-Rapidity Gap Data

Some early H1 and ZEUS studies of diffractive DIS [10–13, 16] imposed strong pseudo-rapidity gap cuts to select diffractive events from DIS data. The diffractive structure function was extracted from large pseudo-rapidity gap cut data and an attempt was made to extract a pomeron structure function. However, the phase space constraints due to pseudo-rapidity gap cuts introduce systematic effects into the data sample that have not been considered before. In Chap. 4 this data is reanalysed taking into account the phase space effects due to pseudo-rapidity gap cuts. The phase space-constraint structure function data is used to test five models of colour-singlet exchange in diffractive DIS. The main results of this analysis are the failure of the two-gluon and Donnachie-Landshoff dijet production models to describe the low-β diffractive structure function data and the success of the Ellis-Ross dijet model in describing the same data. The two-gluon model and Donnachie-Landshoff model results suggest that a significant contribution from higher-order events is required at low β to describe the data, while the Ellis-Ross model does not require any additional contribution. The dijet components of the scalar-pomeron and single-gluon exchange models both provide a reasonable fit to the diffractive structure function data. Following the discussion of the results of the structure function analysis, further experiments are suggested which would help to confirm the conclusions drawn from this data.

The structure function study explores the transverse momentum-integrated diffractive scattering cross section. A further test of models of diffractive DIS, which appears in Chap. 5, is a study of the unintegrated transverse momentum spectrum.

The data chosen for the study of the transverse momentum distribution spectrum is from an H1 analysis [49] of the thrust distribution of diffractive jet production. A weak pseudo-rapidity gap cut was used to select this data, but there is still a significant range of the parameters for which there are final-state phase space constraints due to the combination of the pseudo-rapidity gap cut and a further kinematic cut employed to select diffractive events.

The results of the transverse momentum distribution analysis superficially appear to contradict the structure function analysis of Chap. 4. The transverse momentum distribution analysis favours a scenario in which the large transverse momentum component of diffractive scattering is due to a two-gluon exchange process or the exchange of a Donnachie-Landshoff-type pomeron. Both of these models predict a quartic fall-off of the cross section with increasing transverse momentum. The Ellis-Ross, single-gluon exchange and scalar-pomeron models predict a quadratic dependence of the diffractive cross section with transverse momentum and do not describe the moderate to large transverse momentum data. The low transverse momentum part of the spectrum cannot be described by dijet production models as the pseudo-rapidity gap data selection cut rejects low transverse momentum dijet final-state events. An additional contribution to diffractive DIS is therefore required, such as multi-jet diffractive final-state events. This contribution is required to be peaked at low transverse momenta.

Both the structure function data and the transverse momentum distribution data can be explained in terms of two of the models of diffractive DIS described in Chap. 3. In this picture, the large transverse momentum data is described by a two-gluon (or Donnachie-Landshoff) pomeron and there is a significant low-β 3-jet (quark–antiquark–gluon) final-state contribution which is peaked near zero transverse momentum. This would account for the failure of the two-gluon model to describe the low-β structure function data as well as the low-$p_\perp$ part of the transverse momentum distribution. Including a 3-jet contribution into the Ellis-Ross model would lead to a low-β enhancement of the structure function predicted by this model which would destroy the fit obtained in Chap. 4. However, a low-$p_\perp$ non-dijet contribution *is* required by all models to describe the transverse momentum distribution.

It is probable that diffractive deep-inelastic scattering is due to the exchange of a predominantly two-gluon colour-singlet state with the large transverse momentum part of the spectrum being described by quark–antiquark final states. Quark–antiquark–gluon diffractive final states are required to explain the low-β data and are expected to be peaked at small thrust transverse momenta relative to the proton–virtual photon axis.

The main problem with the description of diffractive DIS in terms of a two-jet plus three-jet contribution is that there is no model fully within perturbative-QCD in which the strongly-peaked transverse momentum distribution required of the 3-jet contribution can be explained. However, in Chap. 5 it is the thrust transverse momentum which is being studied and there currently exists no full calculation or simulation of the expected thrust transverse momentum spectrum in diffractive DIS.

1.8 Outline

The next chapter contains a discussion of the kinematics involved in diffractive deep-inelastic scattering. Kinematic variables important to the analysis in subsequent chapters are defined and the effects of pseudo-rapidity gap cuts on diffractive DIS phase space are studied.

In Chap. 3, five models of the colour-singlet mechanism underlying diffractive DIS are described in detail. The motivation behind each model is discussed and comparisons and connections are drawn between the different approaches. Details of the structure function and cross section calculations are presented for the form factor pomeron-exchange models and the main results for the other models are summarised.

The first comparison of the diffractive DIS models with data is presented in Chap. 4. In this chapter the predictions of colour-singlet exchange models are compared with HERA diffractive structure function data extracted by imposing a large pseudo-rapidity gap cut. Fits to diffractive and pomeron structure function data are presented and the validity of extracting a pomeron structure function from large pseudo-rapidity gap cut data is discussed. Experiments are suggested which would provide a further test of the conclusions drawn from this analysis.

In Chap. 5, the transverse momentum distribution of the diffractive cross section is studied. The available phase space for these interactions is also studied and implications of the phase space constraints are discussed. The differential cross section predicted by each of the diffractive DIS models is compared with thrust transverse momentum distribution data from an H1 analysis which used pseudo-rapidity gap cuts to extract diffractive DIS data. The results of the transverse momentum distribution analysis are compared with the structure function analysis of Chap. 4. A model is proposed which is consistent with both sets of data and experiments are described to further test the conclusions of the structure function and transverse momentum distribution analyses.

The results of the large pseudo-rapidity gap cut structure function and transverse momentum distribution analyses are summarised in Chap. 6. The main conclusions are reiterated and further experiments and future directions for theoretical analyses are proposed. App. A contains details of the virtuality constraint calculations which underlie the large pseudo-rapidity gap analyses of Chaps. 4 and 5. Details of the cross section and structure function calculations for the models described in Chap. 3 appear in App. B.

The algebraic manipulation package `Mathematica` [50], with the additional package `FeynCalc` [51], was used for many of the calculations and the graphical packages `AXODRAW` [52] and `xfig` were used to create most of the graphs and figures.

Chapter 2

Kinematics, Cuts and Phase Space

2.1 Introduction

The kinematics of diffractive deep-inelastic scattering are described in this chapter. The variables of particular interest in this analysis are defined for the dijet production process of Fig. 1.2, and the extension of these definitions to higher-order processes is explained. Particular attention is paid to the pseudo-rapidity gap cut requirement used in H1 (and early ZEUS) analyses to select diffractive DIS events. It has been shown [1–4] that strong pseudo-rapidity cuts select data from a subset of the phase space available for diffractive DIS for a large region of HERA parameter space. Consequences of this phase space reduction are described in this chapter, including the breaking of the $x_{I\!P}$-factorization of the diffractive structure function into a pomeron structure function and a pomeron flux factor. In this region of parameter space, a well-defined pomeron structure function cannot be extracted from the data.

Since the pseudo-rapidity gap cuts impose stronger constraints on dijet final states than on higher-order diffractive processes, an enhanced 3-jet diffractive data sample can be extracted by using pseudo-rapidity gap cuts. Pseudo-rapidity gap cuts remove part of the low transverse momentum dijet spectrum, enabling a study of the large-$p_\perp$ structure of diffractive DIS.

A simple, model-independent test is outlined to demonstrate the phase space effects due to pseudo-rapidity gap cuts, upon which an empirical study of the effect of phase space constraints on higher-order final state events can be based.

2.2 Kinematics of Standard and Diffractive Deep-Inelastic Scattering

Diffractive $e - P$ scattering proceeds by the interaction

$$e(p_e) + P(P) \to e(p'_e) + P(P') + X(X)\,, \tag{2.2.1}$$

where the four-momenta of the particles are shown in brackets. The hadronic system X is assumed to be separated from the forward proton direction by a large angle. The proton (or low-mass excited state) is only slightly deflected and escapes undetected down the beam-pipe, or is detected far downstream [14]. Diffractive DIS is commonly described by the sub-reaction

$$\gamma^*(q) + I\!P(P_{I\!P}) \to X(X)\,, \tag{2.2.2}$$

where a photon of four-momentum q is emitted by the incident electron and undergoes a hard scattering with a colour-singlet state $I\!P$ within the proton and $P_{I\!P} = P - P'$.

In the HERA laboratory (LAB) frame the positive z-axis is defined by the forward proton direction with the origin at the interaction vertex. Since the $e - P$ CMS is strongly boosted in the forward direction, most final-state particles are found in the forward proton hemisphere.

The kinematic variables used to describe standard deep-inelastic scattering are:

$$Q^2 = -q^2 \qquad \text{(negative four-momentum-squared of photon)}$$

$$x_{\rm Bj} = \frac{Q^2}{2P{\cdot}q} \qquad \text{(Bjorken scaling variable)}$$

$$y = \frac{P{\cdot}q}{P{\cdot}p_e} = \frac{Q^2}{x_{\rm Bj}\, S_{\rm Tot}} \qquad \text{(fractional energy transfer at lepton vertex)}$$

$$W^2 = (P+q)^2 \qquad \text{(mass of the total hadronic system} = \text{squared CMS energy of } \gamma^* - P \text{ system)}$$

Further variables are defined to describe diffractive DIS:

$$t_{I\!P} = (P - P')^2 \qquad \text{(momentum transfer at } P \text{ vertex)}$$

$$x_{I\!P} = \frac{(P{-}P'){\cdot}q}{P{\cdot}q} \approx \frac{Q^2{+}M_X^2}{Q^2{+}W^2} \qquad \text{(fraction of proton longitudinal momentum carried by the pomeron)}$$

$$\beta = \frac{Q^2}{2(P{-}P'){\cdot}q} \approx \frac{Q^2}{Q^2{+}M_X^2} = \frac{x_{\rm Bj}}{x_{I\!P}} \qquad \text{(fraction of pomeron momentum carried by the struck quark)}$$

where M_X^2 is the mass-squared of the diffractive system, X. Acceptance cuts restrict $x_{I\!P}$ to be below about 0.05 (above which the contribution from other Reggeon trajectories becomes significant) and β ranges from 0 to 1. Acceptance cuts also limit the contribution from proton dissociation: if M_Y is the mass of the proton remnant, then for H1 $M_Y \lesssim 1.6\,\mathrm{GeV}$ and for ZEUS $M_Y \lesssim 4\,\mathrm{GeV}$. The data studied in Chaps. 4 and 5 describes events with photon virtualities in the range $5 < Q^2 < 50\,\mathrm{GeV}^2$ and with $0.01 < \beta < 0.9$. The proton mass is neglected throughout this analysis where it is small compared to other energy scales.

In a parton-model interpretation of the lowest-order diagram, shown in Fig. 1.2, β is the fraction of pomeron momentum in the exchanged parton and is the diffractive DIS analogue of $x_{\rm Bj}$. Analogously to standard DIS, the small-β part of the pomeron structure function is driven by the gluon content of the pomeron.

For diffractive events, the four-momentum transfer, $t_{I\!P}$, at the proton vertex is restricted by further data selection cuts to be less than $1\,\mathrm{GeV}^2$. ZEUS have measured the $t_{I\!P}$ dependence of the diffractive scattering cross section and found a good fit with the exponential behaviour

$$\frac{\mathrm{d}\sigma}{\mathrm{d}t_{I\!P}} \propto e^{-b|t_{I\!P}|}\,, \tag{2.2.3}$$

where $b = 7.2 \pm 1.1^{+.7}_{-.9}\ \mathrm{GeV}^2$ [14]. In the present analysis the $t_{I\!P}$-dependence is neglected and an implicit integration over $t_{I\!P}$ is assumed. The main effect of this is to introduce a constant with dimensions of energy^2 into the overall normalisation. This will have no effect on this analysis as the free parameter in all the fits is the overall normalisation.

In the pomeron-exchange interpretation of diffractive DIS for small $t_{I\!P}$, to a good approximation, the pomeron is emitted in the forward proton direction.

2.3 Further Kinematics

There are several other kinematic quantities which are important in the analyses in Chaps. 4 and 5. The first, *pseudo-rapidity*, is defined in the HERA LAB frame, while the others are defined in the virtual photon–pomeron CMS.

2.3.1 Pseudo-Rapidity

The *pseudo-rapidity*, η, of an outgoing particle is defined in the laboratory frame in terms of its polar angle with respect to the proton direction by

$$\eta = -\ln\tan\left(\frac{\theta_{\text{lab}}}{2}\right) . \tag{2.3.1}$$

The LAB angle, θ_{lab}, is shown in Fig. 2.1. Fig. 2.2(a) shows the relationship between η and θ_{lab} and Fig. 2.2(b) shows the direction of outgoing particles corresponding to several values of η.

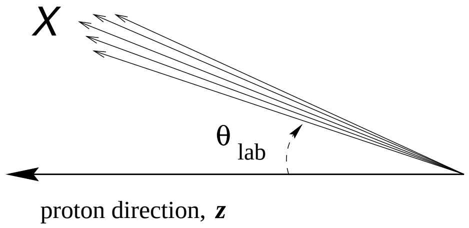

Figure 2.1: *Definition of HERA laboratory angle at hadron level.*

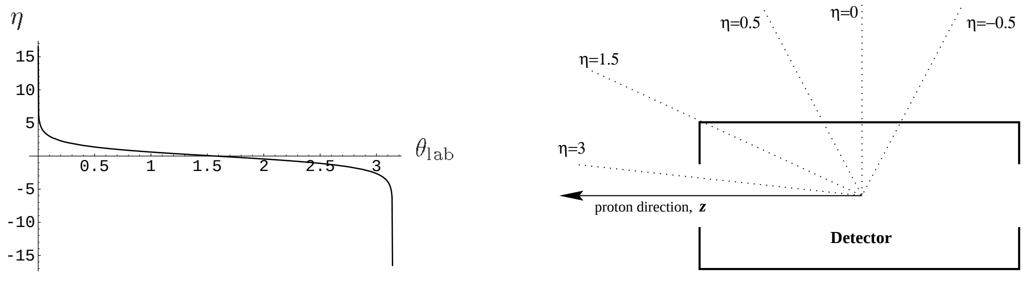

(a) *Relationship between laboratory angle and pseudo-rapidity.*

(b) *Pseudo-rapidity intervals in the H1 and ZEUS detectors.*

Figure 2.2: *Definition of pseudo-rapidity in the HERA laboratory frame.*

There are different definitions of pseudo-rapidity in experiment and at the parton level. Experimentally, a pseudo-rapidity "gap" about the forward proton direction is defined to be the region between the proton direction and the nearest *edge* of the jet formed by the hadronized final-state parton in which there is no hadronic activity above a low-energy cut-off (typically of the order of 400 MeV) in adjacent detector calorimeter cells for η greater than η_{max} [10, 13, 16, 49, 53, 54]. At the parton level, where analytic calculations are made, pseudo-rapidity is defined in terms of the angle between the final-state parton and the proton direction. To relate the two definitions, it is assumed in this analysis that the hadronization radius of a parton spans approximately half a unit in pseudo-rapidity [2,11], that is,

$$\eta_{\max}^{\text{partons}} \approx \eta_{\max}^{\text{hadrons}} - 0.5\,. \tag{2.3.2}$$

Thus, for example, a pseudo-rapidity cut of 1.8 made at hadron level corresponds to a pseudo-rapidity interval of about 1.3 at parton level. This corresponds to an angle of $\theta_{\text{lab}}^{\text{th}} \approx 30°$. This relationship is shown diagrammatically in Fig. 2.3.

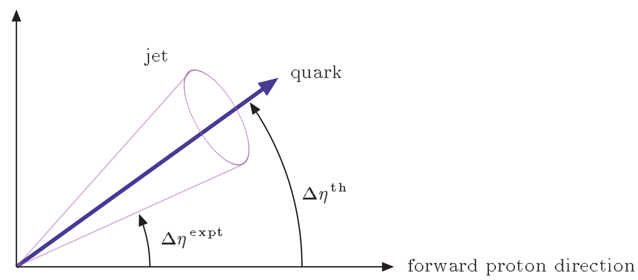

Figure 2.3: *Pseudo-rapidity definition at parton level and at hadron level.*

One way of selecting a diffractive sample from DIS events is to impose a pseudo-rapidity cut. In this case events are selected only if there is no activity observed above a low-energy threshold in a large pseudo-rapidity interval about the forward proton direction. Thus only events with pseudo-rapidity less than some cut-off, $\eta_{\max}$, are accepted. This cut rejects the majority of non-diffractive DIS events. The stronger the pseudo-rapidity gap cut (lower $\eta_{\max}$), the less non-diffractive background in the selected sample. Early pseudo-rapidity gap cuts (at hadron level) by H1 and ZEUS include:

$$\begin{aligned} \text{H1 [12]}:& \quad \eta_{\max} = 1.8 \Rightarrow \theta_{\min} \approx 18° \\ \text{ZEUS [10,11]}:& \; \eta_{\max} = 1.5 \Rightarrow \theta_{\min} \approx 25°\,. \end{aligned} \tag{2.3.3}$$

Since strong pseudo-rapidity cuts reduce the sample size, weaker cuts are favoured in more recent analyses, for example:

$$\begin{aligned} \text{H1 [13]}:& \quad \eta_{\max} = 3.2 \Rightarrow \theta_{\min} \approx 5° \\ \text{ZEUS [53]}:& \; \eta_{\max} = 2.5 \Rightarrow \theta_{\min} \approx 9°\,. \end{aligned} \tag{2.3.4}$$

2.3.2 Exchanged-Quark Virtuality

For the leading-order (to order α_s) diffractive pomeron-exchange process, the four-momentum squared of the struck quark, k^2 (shown in Fig. 2.4), can be expressed in terms of other invariants and the polar angle with respect to the $\gamma^* - I\!P$ axis in the virtual photon–pomeron CMS by

$$k^2 = -\frac{Q^2}{2\beta}(1 - \cos\theta_{\text{cms}})\,. \tag{2.3.5}$$

This is the virtuality of the exchanged parton that couples to the pomeron. In a resolved-coupling scenario, this parton is interpreted as being a constituent of the pomeron and is

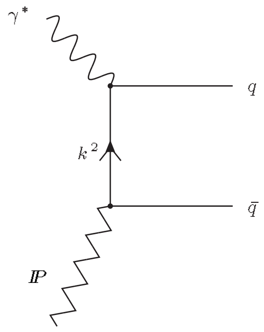

Figure 2.4: *Definition of exchanged-quark virtuality* k^2*.*

therefore expected to be near mass shell. A similar expression can be formed for higher-order diffractive final states, such as those shown in Fig. 1.3.

2.3.3 Thrust and Transverse Momentum

Lower-Quark Transverse Momentum

The first transverse momentum variable of interest is the transverse momentum of the final-state parton which couples directly to the pomeron relative to the virtual photon–pomeron axis in the $\gamma^* - I\!P$ CMS. This transverse momentum variable, $p_\perp$, is shown in Fig. 2.5. For dijet final states $p_\perp$ is related to the diffractive final-state mass, M_X, by

$$p_\perp^2 = \frac{M_X^2}{4} \sin^2 \theta_{\mathrm{cms}} \,, \tag{2.3.6}$$

where θ_{cms} was defined in Sect. 2.3.2.

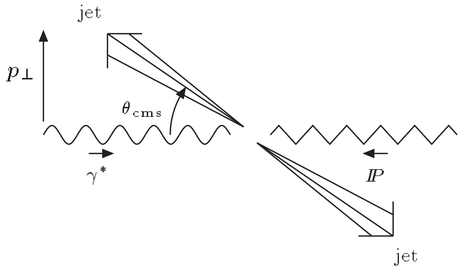

Figure 2.5: *Definition of transverse momentum variable* $p_\perp^2$ *(in* $\gamma^* - I\!P$ *CMS).*

Thrust and Thrust Transverse Momentum

In Chap. 5, the transverse momentum distribution of the thrust axis of the diffractive system predicted by several models of colour-singlet exchange is compared with H1 diffractive DIS data.

The *thrust* variable, T, describes the principal axis of jet momentum and the spread of final-state particles. More formally, the thrust axis is defined to be parallel to the unit vector $\vec{n}$ which maximises the weighted sum

$$T = \left(\frac{1}{\sum_{i=1}^{N} |\vec{p}_i|}\right) \cdot \max_{\vec{n}} \sum_{i=1}^{N} |\vec{p}_i \cdot \vec{n}| \,, \tag{2.3.7}$$

where the sum is taken over the whole diffractive final state and T is the thrust variable[1]. The thrust axis in diffractive dijet production is the axis defined by the back-to-back final-state quarks in the virtual photon–pomeron CMS and is approximated experimentally by the thrust axis described by the (hadronic) diffractive final state. In general, T can take any value between 1/2 and 1. For a dijet event T is equal to 1, for a symmetric 3-jet event $T = 2/3$ and a completely isotropic multi-jet event has $T = 1/2$.

The *thrust transverse momentum*, also denoted by $p_\perp^2$, is defined in the virtual photon–pomeron CMS. For events with dijet final states, $p_\perp$ is the component of momentum of one of the final state quarks which is transverse to virtual photon–proton axis (equivalently, to the virtual photon–pomeron axis) and is therefore equivalent to the lower-quark transverse momentum defined above. In the more general case of final states with two or more partons, the experimentally measured transverse momentum variable is the transverse momentum of the thrust axis with respect to the photon–proton axis. As with the other transverse momentum variable, $p_\perp^2$ ranges from 0 to $M_X^2/4\,\mathrm{GeV}^2$.

For the production of 3-or-more parton diffractive final states, the thrust $p_\perp$ is different from the lower-quark $p_\perp$ definition. In particular, the $p^2_{\perp\,\mathrm{min}}$ cuts on multi-jet events discussed in Sect. 1.4 and App. A apply only to the lower-quark transverse momentum and the restrictions on multi-jet thrust transverse momentum are more subtle and can only be properly explored using Monte Carlo simulations. These effects are discussed in Sect. 2.5.

2.4 Structure Functions

2.4.1 Diffractive Structure Function

In the hadronic picture of the pomeron, one can factorize the diffractive scattering cross section into a sum over the product of the probability to find a parton with momentum fraction β in the pomeron and the cross section for parton–photon hard scattering. In analogy with standard DIS where the photon probes the structure of the proton, one can define a diffractive structure function for these processes in terms of the diffractive cross section

$$\frac{\mathrm{d}^3\sigma^{\mathrm{diff}}}{\mathrm{d}Q^2\,\mathrm{d}\beta\,dx_{I\!P}} = \frac{2\pi\alpha_{\mathrm{em}}^2}{\beta Q^4}[(1+(1-y)^2)F_2^{D(3)}(Q^2,\beta,x_{I\!P}) - y^2 F_L^{D(3)}(Q^2,\beta,x_{I\!P})]\,, \quad (2.4.1)$$

where an implicit integration over the momentum exchange, $t_{I\!P}$, at the proton vertex is assumed. The total diffractive structure function can be written in terms of transverse and longitudinal components by

$$F_2^{D(3)} = F_T^{D(3)} + F_L^{D(3)}\,. \quad (2.4.2)$$

Experimental cuts on the variable y (usually requiring $y \lesssim 0.4$) mean the contribution from $F_L^{D(3)}$ from the second term can be neglected, introducing an uncertainty of less than 17 % [13][2] (radiative corrections are also neglected in this case).

2.4.2 Pomeron Structure Function

Ingelman and Schlein [29] suggested treating the pomeron as an hadronic particle. In this interpretation the diffractive structure function can be factorized into the product of

[1]Some references use a slightly different definition of T. The normalisation of T adopted here is that used by H1 [49].

[2]At present it is not be possible to accurately measure $F_L^{D(3)}$. This will be possible when HERA runs with either polarized beams or variable CMS energy.

a pomeron flux factor, $f_{I\!P/P}(x_{I\!P})$, and an $x_{I\!P}$-independent *pomeron structure function*, $F_2^{I\!P}(Q^2, \beta)$, where

$$F_2^{D(3)}(Q^2, \beta, x_{I\!P}) = f^{I\!P}(x_{I\!P})\, F_2^{I\!P}(Q^2, \beta)\,. \tag{2.4.3}$$

Here β plays the role of the scaling variable $x_{\rm Bj}$ of standard DIS and $F_2^{I\!P}$ is interpreted as the structure function of the pomeron. The normalisation of $F_2^{I\!P}$ is not well-defined.

From Regge theory, the pomeron flux factor is expected to be proportional to

$${x_{I\!P}}^{2\alpha_{I\!P}(t_{I\!P})-1}\,. \tag{2.4.4}$$

This is because there is a factor of $1/x_{I\!P}$ from the phase space contribution to electron–proton diffractive scattering and a further factor of $(1/x_{I\!P})^{2\alpha_{I\!P}(t_{I\!P})-2}$ from the diffractive sub-energy contribution from the pomeron propagator.

Neglecting the $t_{I\!P}$ dependence of the pomeron intercept gives a prediction for the $x_{I\!P}$ dependence of the form ${x_{I\!P}}^{2\alpha_{I\!P}(0)-1}$. This Regge factorization can be tested by fitting structure function data with models with a factorizable power-law $x_{I\!P}$ dependence (with the possible inclusion of additional Reggeon exchanges). The pomeron intercept can also be extracted from this fit. The best measured values of the pomeron intercept from the HERA experiments are currently

$$\begin{aligned} \alpha_{I\!P}(0) &= 1.203 \pm .02\,(\mathrm{stat}) \pm .013\,(\mathrm{syst})^{+.03}_{-.035}\,(\mathrm{model}) \quad \mathrm{H1}\ \ [15]\,, \\ \alpha_{I\!P}(0) &= 1.13 \pm .01\,(\mathrm{stat})^{+.04}_{-.01}\,(\mathrm{syst}) \quad \mathrm{ZEUS}\ \ [55]\,. \end{aligned} \tag{2.4.5}$$

These results suggest that the pomeron intercept appropriate to diffractive DIS is somewhat larger than that extracted from proton–proton scattering experiments by Donnachie and Landshoff of $\alpha_{I\!P}(0) \approx 1.086$ [24–26].

These different measurements of the pomeron intercept suggest that there may be two pomerons [56]. One of these is a soft, non-perturbative pomeron with intercept near the Donnachie-Landshoff value, which is exchanged in hadron–hadron interactions, and the other is a harder, gluonic, perturbative, pomeron which is dominant in HERA interactions. Another possible interpretation is that the soft scattering and DIS experiments are studying different aspects of colour-singlet exchange. Viewed in terms of the structure of the pomeron, soft proton–(anti)proton scattering involves the pomeron coupling to on-shell quarks within the proton. In this case the quarks to which the exchanged pomeron couples may be interpreted as constituents of the pomeron. In diffractive deep-inelastic scattering, the pseudo-rapidity cut analyses presented later in this chapter and in App. A show that for a significant region of HERA parameter space, there exist events in which pomeron–quark couplings require the pomeron to couple directly to off-shell quarks, a scenario which cannot be interpreted in terms of a quark-structure of the pomeron.

Large pseudo-rapidity gap diffractive DIS permits the interaction of the pomeron with off-shell quarks through the exchange of one or more on-shell gluons. This happens, for example, in the two-gluon Landshoff-Nachtmann model, as well as in the QCD interpretation of the Ellis-Ross form factor model. In the latter model, the form factor is interpreted as an effective coupling of a two-gluon component of the pomeron to the partons produced through photon dissociation. In this interpretation soft diffractive scattering events, such as those observed in the proton–(anti)proton analyses of the early Donnachie-Landshoff studies [24–26], are viewed as probing the quark structure of the pomeron, while diffractive deep-inelastic scattering experiments at HERA [10–13] would be interpreted as probing the gluon content of the pomeron. These ideas are discussed further in Chap. 3.

The analyses that follow are restricted to considering just one pomeron, but different choices of intercept are considered to see what value the data favours. A good fit to the large pseudo-rapidity gap cut data can be obtained without a contribution from sub-leading Reggeon exchanges.

2.5 Pseudo-Rapidity Data Selection Cuts

The relationship between pseudo-rapidity cuts and phase space constraints in diffractive DIS and the region of HERA parameter space in Q^2, β and $x_{I\!P}$ in which such effects are observable is calculated in this section. The constraints on kinematic variables are also described and consequences for the extraction of diffractive structure functions and pomeron structure functions are explored.

2.5.1 Introduction

The requirement of an interval of pseudo-rapidity about the forward proton direction in which there is no significant hadronic activity is used in many analyses of HERA data [10–14, 16, 49, 53] to select diffractive DIS events. Since gap events in standard DIS interactions are exponentially suppressed with increasing gap size, this technique is able to remove the majority of the non-diffractive DIS background, particularly if a strong pseudo-rapidity gap cut is applied.

Ellis *et al* [1, 2] have showed that, for a wide region of HERA parameter space in Q^2, β and $x_{I\!P}$, pseudo-rapidity gap cuts restrict the phase space available to the diffractive DIS final state and therefore select only a subset of the diffractive events[3]. Models which propose to describe diffractive DIS should also be able to describe any subset of the data and it is important to understand the consequences of these phase space constraints in order to use large pseudo-rapidity gap cut data to study diffractive DIS.

The pseudo-rapidity data selection cuts restrict the scattering angle of the diffractively produced final-state partons. In interactions such as those shown in Figs. 1.2 and 1.3, this scattering angle can be related to the virtuality of the exchanged parton which couples to the pomeron and also to the transverse momentum of the final-state parton which couples to the pomeron (Eqs. 2.3.5 and 2.3.6). This means that pseudo-rapidity gap cuts restrict the exchanged-quark virtuality and the final-state quark transverse momentum in the diffractive sample. Since the final-state phase space can be expressed in terms of the final-state quark transverse momentum, this means that a pseudo-rapidity gap cut leads to a restriction on the final-state phase space from which the sample is selected[4].

Strong pseudo-rapidity gap cuts can be used to select dijet and higher-order diffractive events for which the virtuality, k^2, of the exchanged parton coupling to the colour-singlet is constrained to be larger than a few GeV^2 and to select events for which the diffractive final state has large transverse momentum relative to the virtual photon–proton axis [1,3]. This means that the pseudo-rapidity gap cut selects a subset of diffractive events which should be well-described by purely perturbative QCD. Large pseudo-rapidity gap cuts can also be used to select an enhanced 3-jet data sample. This enables higher-order QCD processes underlying diffractive DIS to be studied. In particular, an enhanced diffractive DIS sample of gluon-driven events can be selected.

2.5.2 Outline of Phase Space Constraint Calculations

To demonstrate the phase space constraints imposed on the diffractive final state by pseudo-rapidity gap cuts, most of the calculations in this analysis concern dijet diffractive final states. The calculations are extended to consider phase space constraints on multi-jet final states and it is found that weaker constraints are imposed. Full details of the dijet phase space constraint calculations appear in App. A and the corresponding constraints for higher-order diffractive final states are calculated in Sect. A.4.

[3] The original calculation [2] had a small error and an invalid small-angle approximation, both of which were eliminated in [1] and in the present analysis.

[4] It should be noted that for a given pseudo-rapidity gap cut and for a wide range of the parameters, Q^2, β and $x_{I\!P}$, the pseudo-rapidity gap cuts *do* still admit contributions from the whole phase space. This is shown, for example, in Fig. 2.8.

By boosting to the rest frame of the diffractive system ($\gamma^* - I\!P$ CMS), it can be shown that a pseudo-rapidity cut, $\eta_{\rm max}$, in the HERA LAB frame corresponds to a minimum scattering angle, $\theta_{\rm cms}^{\rm min}$, in the CMS. The boost which relates the scattering angles of the diffractively-produced quark–antiquark pair in the two reference frames can be calculated in terms of the parameters Q^2, β and $x_{I\!P}$ and the proton and electron initial energies, E_P and E_e, respectively. In [2] and App. A, the boosts to the diffractive system rest frame are calculated by selecting a LAB reference frame in which the diffractive system has 3-momentum in the xz-plane. The transformation to the CMS is carried out by first boosting in the z-direction and then boosting along the x-direction. The scattering angles $\theta_{\rm cms}$, $\theta_{\rm lab}$ and $\phi_{\rm lab}$, shown in Figs. 2.6(a) and 2.6(b), are related by

$$(1 - \cos\theta_{\rm cms}) = \frac{(1+\beta_1)(1-\beta_2^2)\,(1-\cos\theta_{\rm lab})}{1 - \beta_1\cos\theta_{\rm lab} - \sqrt{1-\beta_1^2}\,\beta_2 \sin\theta_{\rm lab}\cos\phi_{\rm lab}}\,, \tag{2.5.1}$$

where β_1 and β_2 are the boost parameters for boosts in the z- and x-directions, respectively, and

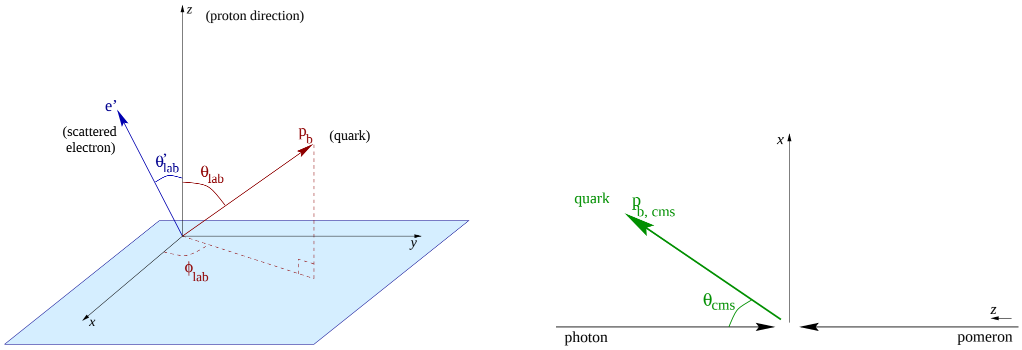

(a) *Definition of angles in the HERA laboratory frame.*

(b) *Definition of angles in the* $\gamma^* - I\!P$ *centre-of-momentum system.*

Figure 2.6: *Angle definitions used in virtuality constraint calculations.*

$$\beta_1 = \frac{-\left[\frac{Q^2}{2}\left(\frac{1}{2E_P\beta x_{I\!P}} + \frac{1}{2E_e}\right) - x_{I\!P}E_P\right]}{\frac{Q^2}{2}\left(\frac{1}{2E_P\beta x_{I\!P}} - \frac{1}{2E_e}\right) + x_{I\!P}E_P}\,,$$

$$\beta_2 = \frac{\beta_1}{\sqrt{1-\beta_1^2}}\;\frac{\left[Q^2\left(1 - \frac{Q^2}{4E_eE_P\beta x_{I\!P}}\right)\right]^{\frac{1}{2}}}{\frac{Q^2}{2}\left(\frac{1}{2E_P\beta x_{I\!P}} + \frac{1}{2E_e}\right) - x_{I\!P}E_P}\,. \tag{2.5.2}$$

The pseudo-rapidity cut, $\eta_{\rm max}$, therefore corresponds to a minimum CMS scattering angle $\theta_{\rm cms}^{\rm min}$ of selected diffractive dijet events of

$$\cos\theta_{\rm cms}^{\rm min} = 1 - \frac{(1+\beta_1)(1-\beta_2^2)\frac{2e^{-2\eta_{\rm max}}}{1+e^{-2\eta_{\rm max}}}}{1 - \beta_1\frac{1-e^{-2\eta_{\rm max}}}{1+e^{-2\eta_{\rm max}}} - \sqrt{1-\beta_1^2}\,\beta_2\frac{2e^{-\eta_{\rm max}}}{1+e^{-2\eta_{\rm max}}}\cos\phi_{\rm lab}}\,. \tag{2.5.3}$$

Pseudo-rapidity gap cuts therefore restrict the minimum exchanged-quark virtuality and lower-quark transverse momentum of events which survive the data selection cuts. The lower limits imposed on these kinematic variables are

$$-k^2_{\min} = \frac{Q^2}{2\beta}\,(1 - \cos\theta^{\min}_{\mathrm{cms}})\,, \tag{2.5.4}$$

$$p^2_{\perp\,\min} = \frac{M_X^2}{4}\,\sin^2\theta^{\min}_{\mathrm{cms}}\,. \tag{2.5.5}$$

For a wide range of Q^2, β, $x_{I\!P}$ and $\eta_{\max}$, $-k^2_{\min}$ and $p^2_{\perp\,\min}$ are constrained to be larger than $1\,\mathrm{GeV}^2$. The consequences of phase space constraints are discussed in terms of the final-state transverse momentum and exchanged-quark virtuality variables in the following sections.

The azimuthal angle ϕ_{lab} of the final-state quarks with respect to direction of the net diffractive final-state momentum is not measured and as a conservative approximation, ϕ_{lab} has been chosen to minimise $-k^2_{\min}$ and $p^2_{\perp\,\min}$. The effect of a non-zero azimuthal angle is considered in Sect. A.3.

2.5.3 Final-State Quark Transverse Momentum Constraints

The phase space constraints imposed on diffractive DIS events selected using large pseudo-rapidity gap cuts can be seen more clearly by examining their effect on the component of momentum of the diffractively produced final-state partons transverse to the virtual photon–proton axis.

The constraint imposed on the transverse momentum of diffractive final-state partons by imposing a pseudo-rapidity gap cut is shown in Eq. 2.5.5. The minimum transverse momentum, $p^2_{\perp\,\min}$, is a function of the pseudo-rapidity cut, $\eta_{\max}$, as well as the kinematic variables Q^2, β and $x_{I\!P}$. In Tables 2.1 and 2.2 the minimum (hadron-level) LAB and CMS scattering angles, $\theta^{\mathrm{exp}}_{\min}$ and $\theta^{\mathrm{cms}}_{\min}$, transverse momentum, $p^2_{\perp\,\min}$, and exchanged-quark virtuality, $|k^2_{\min}|$, for diffractive dijet production events are shown as a function of pseudo-rapidity cut, $\eta_{\max}$, and Q^2, β and $x_{I\!P}$ for two different pseudo-rapidity gap cuts. The $p^2_{\perp\,\min}$ cut-off imposed by pseudo-rapidity gap cuts increases approximately linearly with increasing $x_{I\!P}$ at fixed Q^2 and β. The cut-off also increases approximately linearly with decreasing β at fixed Q^2 and $x_{I\!P}$. The Q^2 dependence is only significant at low photon virtualities.

In the CMS of the two-jet system, a pseudo-rapidity gap cut-imposed condition $\theta^{\mathrm{cms}}_{\min} > 90°$ is equivalent to requiring there to be no particles in the forward interaction hemisphere. Since the two jets must be back-to-back in the dijet CMS, there can be no configuration which simultaneously conserves momentum and satisfies this pseudo-rapidity gap constraint. Table 2.2 contains two points corresponding to the angular restriction $\theta^{\mathrm{cms}}_{\min} > 90°$. These are the only two points in Table 2.2 that have measured values of $F_2^{D(3)}$ which are consistent with zero within the measurement uncertainties.

Pseudo-rapidity cut data for which the $\eta_{\max}$ cut selects only events for which $p^2_{\perp\,\min}$ is larger than a few GeV^2 provides a probe of the large-$p^2_\perp$ (and large-k^2) structure of the colour-singlet exchange models. The transverse momentum dependence of colour-singlet models can also be studied by varying the $\eta_{\max}$ cut and looking in the phase space-constrained region of parameter space.

Figs. 2.7 and 2.8 show the dependence of $p^2_{\perp\,\min}$ on Q^2, β and $x_{I\!P}$ for diffractive dijet production for a pseudo-rapidity gap cut of $\eta_{\max} = 1.8$, corresponding to early H1 analyses [12] and for the weaker cut of $\eta_{\max} = 3.2$ which has been used in more recent analyses [13, 49]. The constraints due to pseudo-rapidity gap cuts are strongest at small β and at large $x_{I\!P}$. This means that, due to the weaker constraint on multi-jet diffractive production, $k^2_{\min\ \mathrm{multi-jet}} \approx 1/3\,k^2_{\min\ \mathrm{dijet}}$, an enhanced 3-jet sample is selected in the region of small β. This is a significant result as the small-β data is already expected to have a large 3-jet component [58–61] since, in diffractive DIS, β is interpreted as the momentum fraction of the struck parton in the pomeron and, in analogy with standard DIS, the pomeron

Q^2 GeV^2	β	x	$x_{I\!P}$	$p^2_{\perp\,\mathrm{min}}$ GeV^2 ($\eta_{\max} = 3.3$)	$\lvert k^2_{\mathrm{min}}\rvert$ GeV^2 ($\eta_{\max} = 3.3$)	$p^2_{\perp\,\mathrm{min}}$ GeV^2 ($\eta_{\max} = 2.0$)	$\lvert k^2_{\mathrm{min}}\rvert$ GeV^2 ($\eta_{\max} = 2.0$)
18	0.04	0.00042	0.0105	0.99	1.04	12.19	13.08
18	0.04	0.00075	0.0188	3.08	3.23	32.79	37.24
18	0.04	0.00133	0.0332	9.16	9.76	70.50	92.41
18	0.1	0.00042	0.0042	0.14	0.16	1.78	2.00
18	0.1	0.00075	0.0075	0.44	0.49	5.13	5.89
18	0.1	0.00133	0.0133	1.32	1.48	13.05	15.90
18	0.1	0.00237	0.0237	3.88	4.42	26.72	37.50
18	0.1	0.00421	0.0421	10.31	12.29	38.64	70.72
18	0.2	0.00042	0.0021	0.03	0.03	0.36	0.45
18	0.2	0.00075	0.0038	0.09	0.11	1.05	1.33
18	0.2	0.00133	0.0067	0.26	0.33	2.85	3.72
18	0.2	0.00237	0.0119	0.79	1.00	6.75	9.43
18	0.2	0.00421	0.0211	2.20	2.84	12.49	20.10
18	0.2	0.00750	0.0375	5.47	7.45	17.03	34.58
18	0.4	0.00042	0.0011	0.004	0.006	0.05	0.08
18	0.4	0.00075	0.0019	0.01	0.02	0.15	0.25
18	0.4	0.00133	0.0033	0.04	0.06	0.42	0.72
18	0.4	0.00237	0.0059	0.11	0.19	1.09	1.89
18	0.4	0.00421	0.0105	0.32	0.54	2.37	4.38
18	0.4	0.00750	0.0188	0.85	1.47	4.15	8.53
18	0.4	0.01330	0.0333	1.96	3.54	5.69	13.57
18	0.65	0.00042	0.0006	0	0	0.006	0.02
18	0.65	0.00075	0.0012	0.002	0.004	0.01	0.06
18	0.65	0.00133	0.0020	0.005	0.01	0.06	0.16
18	0.65	0.00237	0.0036	0.01	0.04	0.15	0.43
18	0.65	0.00421	0.0065	0.04	0.12	0.35	1.03
18	0.65	0.00750	0.0115	0.11	0.33	0.69	2.15
18	0.65	0.01330	0.0205	0.28	0.82	1.13	3.72
18	0.9	0.00075	0.0008	0	0	0.001	0.01
18	0.9	0.00133	0.0015	0	0.002	0.002	0.02
18	0.9	0.00237	0.0026	0	0.006	0.006	0.06
18	0.9	0.00421	0.0047	0.002	0.02	0.02	0.16
18	0.9	0.00750	0.0083	0.005	0.05	0.03	0.34
18	0.9	0.01330	0.0148	0.01	0.13	0.06	0.62

Table 2.1: *Constraints on final-state quark transverse momentum and exchanged-quark virtuality from pseudo-rapidity gap cuts for H1 data from [15].*

Q^2 GeV^2	β	$x_{I\!P}$	$\lvert k^2_{\min}\rvert$ GeV^2	$\lvert k^2_{\max}\rvert$ GeV^2	$p^2_{\perp\min}$ GeV^2	$\theta^{\exp}_{\mathrm{lab}}$ ($\eta^{\exp}_{\max} = 1.8$)	$\theta^{\exp}_{\mathrm{cms}}$	$F_2^{D(3)}$	$\delta F_2^{D(3)}$
8.5	0.065	0.00365	2.31	131	2.1	30	15	3.84	3.07
		0.00649	6.68	131	5.9	30	26	4.49	2.84
12	0.065	0.00649	6.94	184	6.2	30	22	4.26	1.99
		0.01154	18.88	184	15.9	30	37	3.28	2.10
		0.02052	44.22	184	31.4	30	59	0.69	0.45
		0.03648	82.07	184	42.6	30	84	1.07	0.55
	0.175	0.00429	2.47	69	2.0	30	22	7.42	3.31
		0.00762	6.41	69	4.8	30	36	3.28	2.06
		0.01355	14.25	69	9.3	30	54	2.31	0.87
		0.02410	25.51	69	13.2	30	75	0.81	0.69
	0.375	0.00356	1.13	32	0.7	30	22	9.98	3.06
		0.00632	2.71	32	1.6	30	34	5.65	1.69
		0.01125	5.54	32	2.9	30	49	3.53	1.51
	0.65	0.00649	1.17	18	0.4	30	29	4.37	2.48
25	0.065	0.01154	21.21	385	18.7	30	27	2.19	1.03
		0.02052	55.11	385	44.2	30	44	0.84	0.43
		0.03648	119.31	385	77.0	30	68	0.61	0.36
		0.06488	201.36	385	89.7	30	93	0.01	0.12
	0.175	0.00429	2.68	143	2.2	30	16	11.53	3.92
		0.00762	7.42	143	5.8	30	26	3.29	1.29
		0.01355	18.35	143	13.2	30	42	2.22	1.21
		0.02410	37.83	143	22.9	30	62	1.71	0.61
		0.04285	62.20	143	29.0	30	83	0.64	0.41
	0.375	0.00356	1.27	67	0.8	30	16	10.08	2.94
		0.00632	3.30	67	2.0	30	26	4.65	1.47
		0.01125	7.53	67	4.2	30	39	3.06	1.00
		0.02000	14.28	67	7.0	30	55	1.50	0.72
	0.65	0.00649	1.52	38	0.5	30	23	6.57	2.53
		0.01154	3.11	38	1.0	30	33	2.94	1.41
50	0.175	0.00762	8.21	286	6.6	30	20	5.74	3.25
		0.01355	21.86	286	16.7	30	32	2.61	1.73
		0.02410	50.59	286	34.3	30	50	1.46	0.87
		0.04285	95.22	286	52.4	30	71	0.49	0.42
		0.07620	143.28	286	58.9	30	90	0.07	0.40
	0.375	0.00356	1.38	133	0.9	30	12	13.40	6.54
		0.00632	3.79	133	2.3	30	19	10.14	4.27
		0.01125	9.43	133	5.5	30	31	4.54	1.69
		0.02000	20.03	133	10.6	30	46	2.04	0.97
		0.03556	34.98	133	16.1	30	62	1.38	1.17
	0.65	0.00649	1.85	77	0.6	30	18	9.56	4.56
		0.01154	4.16	77	1.4	30	27	2.59	1.78
		0.02052	7.93	77	2.5	30	37	1.49	0.96

Table 2.2: *Large pseudo-rapidity gap cut phase space constraint diffractive structure function data, $F_2^{D(3)}(Q^2, \beta, x_{I\!P})$ [57]. The minimum LAB and CMS scattering angles, exchanged-quark virtualities and final-state quark transverse momentum limits corresponding to diffractive dijet production and a pseudo-rapidity gap cut of $\eta^{\mathrm{expt}}_{\max} = 1.8$ are shown. The statistical and systematic errors in the structure function have been added in quadrature to obtain an estimate of the uncertainty, $\delta F_2^{D(3)}$.*

structure is expected to be driven by gluon-dominated processes at small momentum fractions [6, 17]. Figs. 2.7 and 2.8 also show that there are no constraints due to pseudo-rapidity gap cuts in the photo-production regime ($Q^2 \to 0$).

Since $p^2_{\perp\,\mathrm{min}}$ is largest at large $x_{I\!P}$ and at small β, the data selected by imposing a pseudo-rapidity cut would contain less events at large $x_{I\!P}$ and small β than the full diffractive data sample. (The full diffractive data sample could be selected by imposing a weaker pseudo-rapidity gap cut or by some other means, such as the ZEUS $\ln M_X^2$ method [62] or leading-proton spectrometry [14].) As a result, the diffractive structure function which is extracted from the cross section by integrating over the kinematically accessible range of $p^2_\perp$ will be lower at large $x_{I\!P}$ and small β (in the phase space-restricted region of parameter space) than the true diffractive structure function. The consequences of this result for $x_{I\!P}$-factorization and the extraction of a pomeron structure function from large pseudo-rapidity gap cut data are discussed in Sect. 2.5.5.

Figs. 2.7 and 2.8 show that $p^2_{\perp\,\mathrm{min}}$ is a function of Q^2. Large pseudo-rapidity gap data selection cuts therefore introduce a further Q^2-dependence into the extracted data. This extra dependence is an artifact of the data selection cuts and has nothing to do with the pomeron structure, but could be misidentified as part of the gluonic component of the pomeron. The inclusion of the Q^2-dependent phase space effects could lead to a more isotropic distribution of the pomeron momentum in analyses such as the H1 study [15] discussed in Sect. 1.6. There is a significant difference between the β-dependence of the structure function at low $p^2_{\perp\,\mathrm{min}}$, i.e., in the absence of significant phase space constraints, and at large $p^2_{\perp\,\mathrm{min}}$ in some models of diffractive DIS. This is a further way in which large pseudo-rapidity constraint diffractive DIS data can be used to study colour-singlet exchange models. The large pseudo-rapidity gap constraint β dependence of several models is discussed further in Chap. 3.

It is important to note that for a large range of Q^2, β and $x_{I\!P}$, the minimum final-state transverse momentum is restricted to $p^2_{\perp\,\mathrm{min}} \lesssim 1\,\mathrm{GeV}^2$ and in this region the pseudo-rapidity cuts do not restrict the available phase space. Recent analyses [13, 15] do not have significant effects due to pseudo-rapidity gap cuts except at relatively large pomeron momentum fractions. This is mainly due to the smaller values of $x_{I\!P}$ studied and the weaker pseudo-rapidity gap cuts used.

At small β the dijet component of diffractive events will be strongly suppressed compared to $q\bar{q}g$ and higher-order diffractive final-state events because the lower-parton transverse momentum constraint on multi-jet events is approximately (see [1] and Sect. A.4)

$$p^2_{\perp\,\mathrm{min},\ \mathrm{multi-jet}} \approx \frac{1}{3} p^2_{\perp\,\mathrm{min},\ \mathrm{dijet}} \tag{2.5.6}$$

and $p^2_{\perp\,\mathrm{min}}$ is largest at small β. This result also applies to the limits on minimum exchanged-quark virtuality, k^2_{min}.

Furthermore, since the diffractive dijet final state quark and antiquark are back-to-back in the $\gamma^* - I\!P$ CMS, not only do pseudo-rapidity cuts restrict the CMS diffractive scattering angle θ_{cms} by removing events with $0 < \theta_{\mathrm{cms}} < \theta^{\mathrm{min}}_{\mathrm{cms}}$, where $\theta^{\mathrm{min}}_{\mathrm{cms}}$ can be calculated from the pseudo-rapidity cut, but also the symmetry of the system further restricts θ_{cms}, selecting only events with diffractively-produced quarks in the range $\theta^{\mathrm{min}}_{\mathrm{cms}} < \theta_{\mathrm{cms}} < 180° - \theta^{\mathrm{min}}_{\mathrm{cms}}$. A final-state parton in a multi-jet configuration with $180° - \theta^{\mathrm{min}}_{\mathrm{cms}} < \theta_{\mathrm{cms}} < 180°$ does not have to be balanced by a parton in the pseudo-rapidity cut region and there is no equivalent symmetry restriction on multi-jet production. Imposing a strong pseudo-rapidity gap cut could therefore be used to extract an enhanced 3-jet diffractive data sample.

The 3-jet thrust transverse momentum cannot be fully constrained as there exist final-state configurations in which, for example, $p^2_{\perp\mathrm{thrust}} = 0$ for which the events survive the pseudo-rapidity cuts. However, events where a parton is emitted in the far forward direction are expected to be rejected by the pseudo-rapidity cuts and hence there is likely to be a systematic reduction in the low-$p_\perp$ 3-jet thrust spectrum. This effect is more subtle than the effect of cuts on the dijet thrust-$p_\perp$ spectrum and, at best, could be investigated

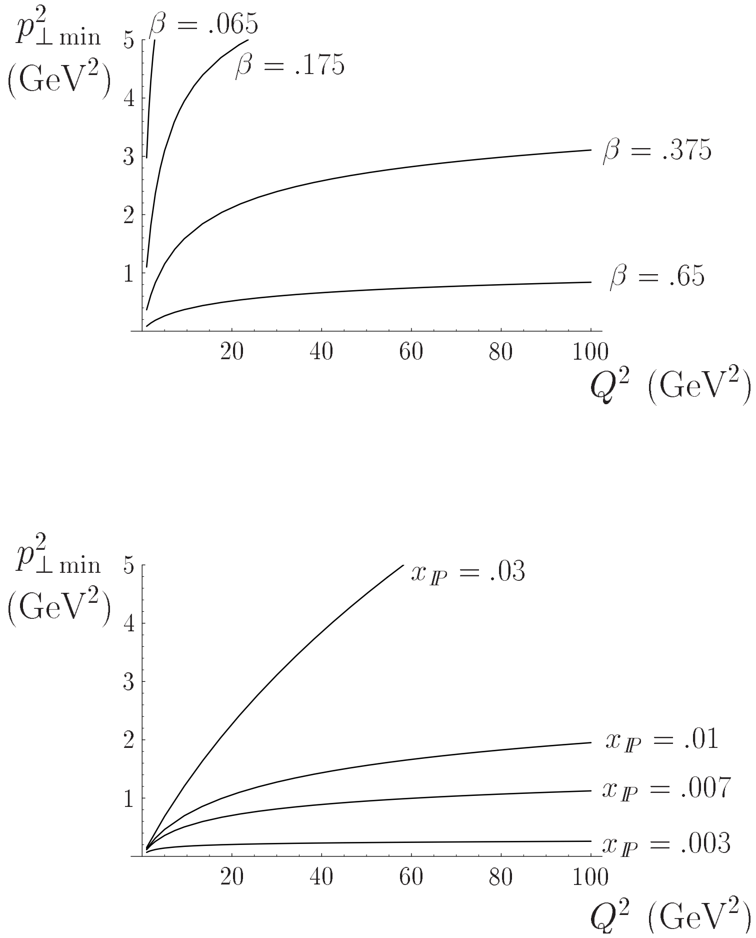

Figure 2.7: *Dependence of minimum transverse momentum, $p^2_{\perp\,\mathrm{min}}$, on the kinematic parameters Q^2, β and $x_{I\!P}$ for a pseudo-rapidity gap cut of $\eta_{\max} = 1.8$. In the top graph $x_{I\!P} = 0.007$, while in the bottom graph $\beta = 0.6$.*

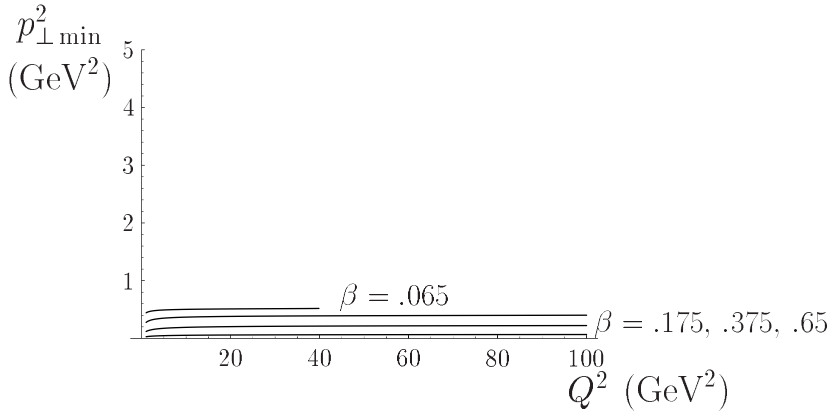

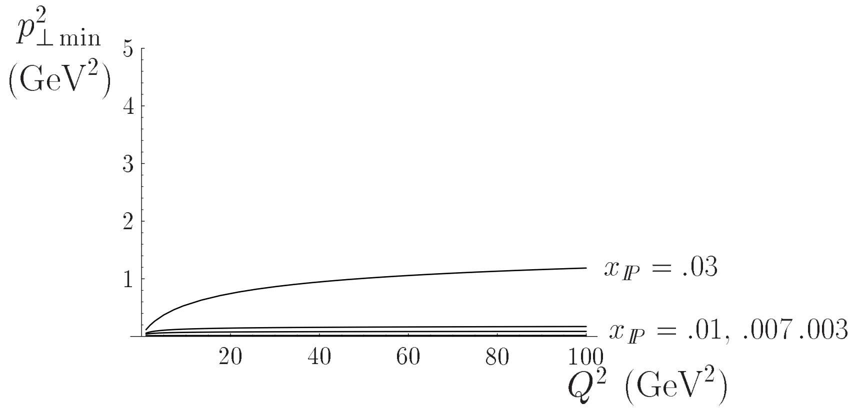

Figure 2.8: *Dependence of minimum transverse momentum, $p^2_{\perp\,\mathrm{min}}$, on the kinematic parameters Q^2, β and $x_{I\!P}$ for a pseudo-rapidity gap cut of $\eta_{\mathrm{max}} = 3.2$. In the top graph $x_{I\!P} = 0.007$, while in the bottom graph $\beta = 0.6$.*

through Monte Carlo studies of diffractive DIS.

2.5.4 Exchanged-Quark Virtuality Constraints

A cut in pseudo-rapidity corresponds to a lower bound on $\theta_{\rm cms}$, which translates into a lower bound, $-k^2_{\rm min}$, on the struck quark virtuality. For a pseudo-rapidity gap cut, $\eta_{\rm max}$, and for a wide range of Q^2, β and $x_{I\!P}$, the struck parton coupling to the pomeron in Figs. 1.2 and 1.3 is forced to be far off mass shell, i.e., $|k^2_{\rm min}| > 1\,{\rm GeV}^2$.[5]

Fig. 2.9 shows the dependence of $k^2_{\rm min}$ on the parameters Q^2, β and $x_{I\!P}$ at $\eta_{\rm max} = 1.8$. The minimum exchanged-quark virtuality, $k^2_{\rm min}$, is a sensitive function of both $x_{I\!P}$ and β; for large $x_{I\!P}$, the virtuality constraints are particularly strong, as for small β. By contrast, Fig. 2.10 shows the virtuality constraints for the weaker cut $\eta_{\rm max} = 3.2$. In this case, for most of the range of Q^2, β and $x_{I\!P}$ used in current HERA analyses, there is no significant phase space reduction imposed by the pseudo-rapidity gap requirement. Figs. 2.9 and 2.10 show approximately the same trend as the transverse momentum constraints, with large $|k^2_{\rm min}|$ at large $x_{I\!P}$ and at small β and no constraint in the photo-production limit of $Q^2 \to 0$.

The weaker constraint,

$$|k^2_{\rm min}|,\ _{\rm multi-jet} \approx \frac{1}{3}|k^2_{\rm min}|,\ _{\rm dijet}\ , \tag{2.5.7}$$

applies to multi-jet events. Table. 2.2 shows that there is still a large range of parameter space for which multi-jet events also have $|k^2_{\rm min}|$ greater than a few ${\rm GeV}^2$, but for which the diffractive structure function is non-zero. This means that large pseudo-rapidity gap cuts also rule out resolved-coupling multi-jet contributions for a wide range of Q^2, β and $x_{I\!P}$, but there is still some, possibly direct-coupling, contribution to diffractive scattering.

In the Ingelman-Schlein picture [29], the pomeron is interpreted as an hadronic particle. This means that the partons which the pomeron couples to are interpreted as being constituents of the pomeron and are necessarily close to mass shell. Fig. 2.9 shows that, for a significant (and calculable) region of HERA parameter space in Q^2, β and $x_{I\!P}$, pseudo-rapidity data selection cuts select only the direct-coupling component of the colour-singlet exchange for diagrams corresponding to Figs. 1.2 and 1.3. That is, the processes shown in Figs. 1.2 and 1.3 cannot contribute to the hadronic picture of resolved pomeron–parton coupling and still describe large pseudo-rapidity gap diffractive DIS. The structure function data shown in Table 2.2 demonstrates that there is a significant cross section even in regions of parameter space in which phase space constraints apply.

This means that one must either abandon the hadronic interpretation of the pomeron or find another way to describe diffractive DIS within the framework of QCD. The approach to the first option is to allow direct pomeron–parton couplings and to adopt a phenomenological model in order to describe the colour-singlet exchange process. This is the approach of the Donnachie-Landshoff [26, 47] model and the scalar-pomeron model [48]. Superficially, the Ellis-Ross form factor model is in the same spirit as the Donnachie-Landshoff model. A possible interpretation of the Ellis-Ross model in terms of a two-gluon component of the pomeron is discussed in Sect. 3.3.2.

2.5.5 Factorization-Breaking Due to Pseudo-Rapidity Gap Cuts

Deviations from $x_{I\!P}$-factorization arise from sub-leading Reggeon exchanges at large $x_{I\!P}$ and from phase space effects due to data selection cuts either at large $x_{I\!P}$ or at small β.

In large pseudo-rapidity gap cut experiments the full structure function is not measured. A more limited quantity, the diffractive scattering cross section integrated over a

[5] These calculations include the approximation described in Sect. 2.3.1 relating $\eta^{\rm exp}$ to $\eta^{\rm lab}$ and their robustness has been tested by also considering the extreme cases where the hadronizing parton is at either edge of the resulting jet. A large lower bound, $|k^2_{\rm min}| \gtrsim 1\,{\rm GeV}^2$, remains, demonstrating that even in the weakest possible case strong pseudo-rapidity gap cuts impose significant phase space restrictions [1].

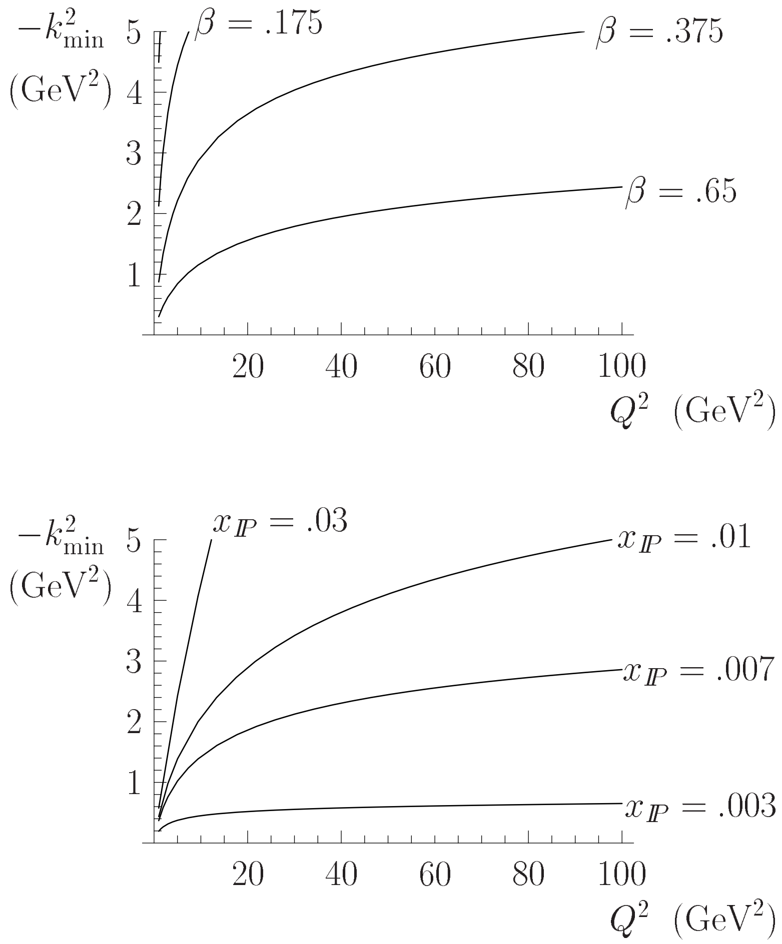

Figure 2.9: *Dependence of minimum exchanged-quark virtuality, $-k^2_{\rm min}$, on the kinematic parameters Q^2, β, and $x_{I\!P}$ for a pseudo-rapidity gap cut of $\eta_{\rm max} = 1.8$. In the top graph $x_{I\!P} = 0.007$, while in the bottom graph $\beta = 0.6$.*

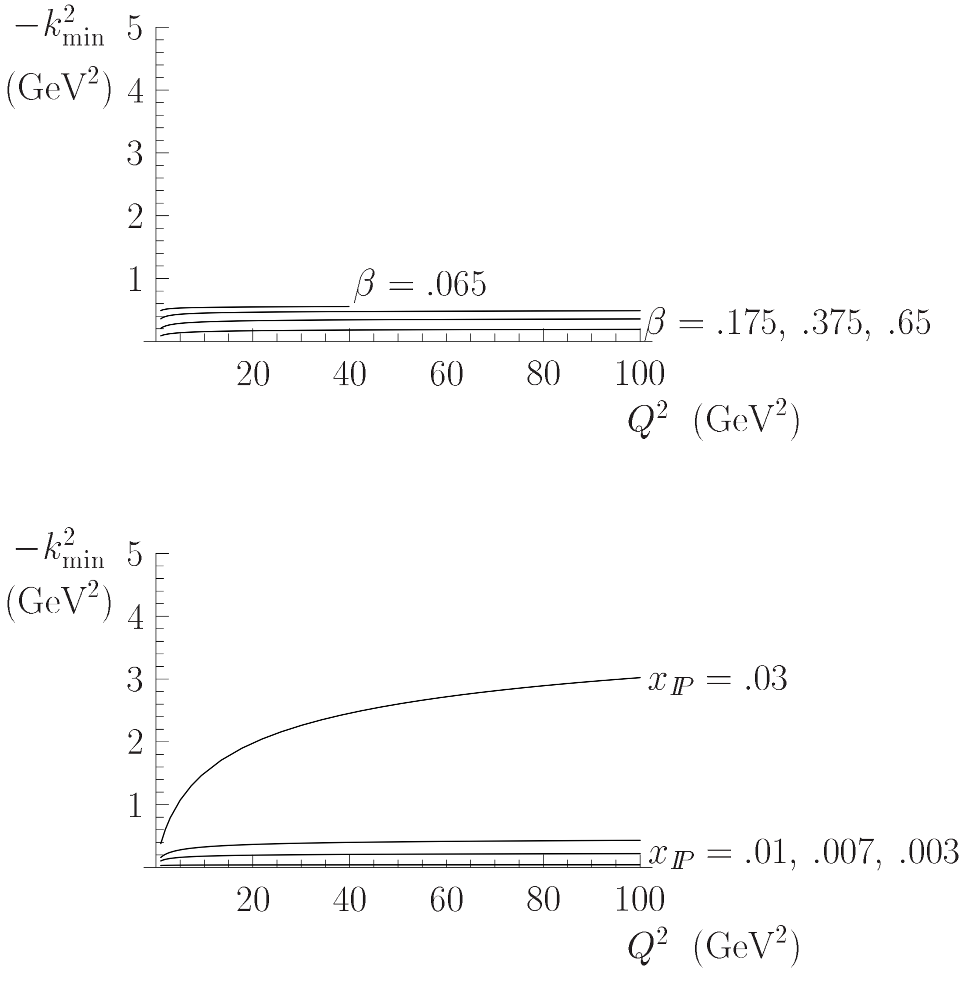

Figure 2.10: *Dependence of $-k^2_{\rm min}$ on the kinematic parameters Q^2, β and $x_{I\!P}$ for a pseudo-rapidity gap cut of $\eta_{\rm max} = 3.2$. In the top graph $x_{I\!P} = 0.007$, while in the bottom graph $\beta = 0.6$.*

restricted region of parameter space, is extracted. Phase space restrictions lead to a relative reduction in $F_2^{D(3)}$ and the magnitude of this reduction will depend on the parameters Q^2, β and $x_{I\!P}$.

In the Ingelman-Schlein interpretation of diffractive DIS, the diffractive structure function factorizes into the product of an $x_{I\!P}$-dependent pomeron flux factor, $f_{I\!P/P}(x_{I\!P})$, and an $x_{I\!P}$-independent pomeron structure function, $F_2^{I\!P}(Q^2, \beta)$. The $x_{I\!P}$-factorization can be spoilt by sub-leading Reggeon exchanges as well as by phase space effects from data selection cuts. Exchanges from sub-leading trajectories become significant at large $x_{I\!P}$ and tend to enhance the diffractive structure function in the large-$x_{I\!P}$ region [15]. Pseudo-rapidity gap cuts introduce a further source of factorization-breaking into the diffractive structure function in the form of a *suppression* of $F_2^{D(3)}$. These effects occur in phase space-restricted regions of parameter space, particularly at large $x_{I\!P}$ and at small β. This is because the experimentally extracted diffractive structure function is obtained by integrating the differential cross section over the kinematically accessible phase space. The diffractive structure function can be expressed in terms of the lower-quark transverse momentum variable, $p_\perp^2$, as an integral over the diffractive scattering cross section by

$$F_2^{D(3)}(Q^2, \beta, x_{I\!P}) \propto \int_{p^2_{\perp\,\mathrm{min}}}^{\frac{M_X^2}{4}} \mathrm{d}p_\perp^2 \, \frac{\mathrm{d}^4\sigma^{\mathrm{diff}}}{\mathrm{d}Q^2 \mathrm{d}\beta \mathrm{d}x_{I\!P} \mathrm{d}p_\perp^2} \,. \tag{2.5.8}$$

In the case that the experimental cuts admit the full range of $p_\perp^2$, i.e. $p^2_{\perp\,\mathrm{min}} \approx 0$, these experiments measure the full diffractive structure function, $F_2^{D(3)}$. For data chosen with strong pseudo-rapidity gap cuts, however, $p^2_{\perp\,\mathrm{min}}$ is non-zero for a wide range of the kinematic variables Q^2, β and $x_{I\!P}$. Further, $p^2_{\perp\,\mathrm{min}}$ is a function of Q^2, β and $x_{I\!P}$. This means that, even if the full diffractive structure function which is integrated over the full final-state phase space is factorizable, the diffraction structure function which is extracted from data selected using large pseudo-rapidity gap cuts will have a further, unfactorizable, $x_{I\!P}$ dependence introduced through the lower limit of the transverse momentum integral.

The pattern of factorization breaking expected from phase space effects can be estimated from the relation between $p^2_{\perp\,\mathrm{min}}$ and $x_{I\!P}$. Figs. 2.9 and 2.10 show that $p^2_{\perp\,\mathrm{min}}$ increases approximately linearly with $x_{I\!P}$. As a result, the phase space constraints become increasingly significant with increasing $x_{I\!P}$. This means that there are stronger factorization-breaking effects at large $x_{I\!P}$. A consequence of this breakdown of $x_{I\!P}$-factorization is that a well-defined $x_{I\!P}$-independent pomeron structure function cannot be extracted from phase space constrained large pseudo-rapidity gap cut data.

Since $p^2_{\perp\,\mathrm{min}}$ varies with Q^2, β and $x_{I\!P}$, there is a systematic decrease in the diffractive structure function extracted using pseudo-rapidity cuts compared to that which would be extracted using techniques which do not constrain the final-state phase space. For the weaker pseudo-rapidity cuts employed in some H1 analyses [13, 49], a reduction in the diffractive structure function extracted at either large $x_{I\!P}$ or at small β, is still expected over that observed with other techniques such as leading proton detection.

2.6 Summary

Pseudo-rapidity gap cuts restrict the available phase space for diffractive DIS in a significant region of parameter space. The region of phase space explored in an H1 data sample taken with strong pseudo-rapidity gap cuts has been calculated. The results of this calculation demonstrate that the cuts reject diffractive final states with low transverse momentum relative to the virtual photon–proton axis, particularly at low β and at large $x_{I\!P}$.

In regions of parameter space where pseudo-rapidity gap cuts constrain the available phase space, one cannot extract a well-defined pomeron structure function, $F_2^{I\!P}$. Since strong pseudo-rapidity gap cuts remove low-transverse momentum diffractive DIS events in a (calculable) region of HERA parameter space, it is possible to extract a diffractive data sample that explores the large-$p_\perp$ behaviour of diffractive DIS. This result suggests a way to study the high-$p_\perp$ structure of diffractive DIS. This is useful because the full diffractive DIS data sample is strongly peaked at low transverse momenta.

Finally, since the phase space constraints due to pseudo-rapidity gap cuts are weaker for multi-jet diffractive final states than for dijet final states, pseudo-rapidity gap data selection cuts provide a technique for extracting an enhanced multi-jet sample from the dijet-dominated full diffractive DIS data.

In the following chapters these results are used to study diffractive DIS and, in particular, to test a range of models of diffractive DIS. The data used corresponds to regions of parameter space in which there are strong restrictions on the diffractive final-state phase space.

Chapter 3

Models of Diffractive DIS

3.1 Introduction

Possible descriptions of the colour-singlet exchange in diffractive DIS can be explored by testing new and existing models of diffractive DIS. By this means, some models can be ruled out and further information can be extracted about diffractive DIS which will help with building future models.

This chapter describes the models of pomeron exchange that are tested against large pseudo-rapidity gap diffractive DIS data in Chaps. 4 and 5. The models broadly fit into two categories: one in which the pomeron has a particle-like interpretation, coupling to partons with resolved (on-shell) couplings and one in which the pomeron has a photon-like behaviour and is allowed to couple directly to off-shell partons. The ideas of direct and resolved pomeron couplings are discussed in some detail and the models are introduced in terms of these classifications.

Five models of diffractive dijet production are described in this chapter: Donnachie-Landshoff and Ellis-Ross form factor pomeron exchange, direct-coupling scalar-pomeron exchange, colour-singlet two-gluon exchange and colour-singlet single-gluon exchange. The description of the models starts with the Ingelman-Schlein interpretation of the pomeron as an hadron-like particle and the connection of this interpretation with the concept of a pomeron structure function. Connections between the individual models and physical interpretations are explored. There exist no complete calculations of multi-jet production which can be compared with phase-space restricted diffractive data, although there is much qualitative information from data corresponding to the full diffractive phase space which can be used to make inferences about higher-order diffractive final states.

The pomeron intercept, described in Sect. 1.3, does not appear analytically in any of the models discussed and is introduced by hand in all of the models. It is included to reproduce the Regge behaviour of the total cross section observed in proton–(anti)proton diffractive and elastic scattering [24–27]. Three choices of pomeron intercept are used in the analyses presented in Chaps. 4 and 5: $\alpha_{I\!P}(0) = 1.08$, which corresponds to the intercept extracted from soft hadron–hadron scattering data by Donnachie and Landshoff [24–27]; $\alpha_{I\!P}(0) = 1.2$, which corresponds to the intercept measured by H1 and ZEUS in diffractive DIS experiments [15,55] (from data which is predominantly unaffected by pseudo-rapidity gap cut-induced phase space constraints); and $\alpha_{I\!P}(0) = 1$. The choice of unit intercept is adopted by Nikolaev *et al* [33] and Hautmann *et al* [63] and corresponds to keeping the $x_{I\!P}$-dependence that is given by calculating the diagrams, rather than altering the $x_{I\!P}$-dependence by hand. However, the choice of unit intercept does not describe the slow rise of total cross sections in proton–(anti)proton elastic and diffractive scattering [24–27].

The Donnachie-Landshoff-type form factor models are not invariant under changes of photon gauge and an alternative choice of photon gauge is discussed in Sect. 3.3.3. This gauge choice is used as well as with the Feynman gauge in the fits in Chaps. 4 and 5.

Finally, this chapter contains a summary of differential cross section and structure function calculations for diffractive dijet production using the models discussed.

3.2 Resolved and Direct Pomeron Coupling

Models of pomeron exchange can be broadly classified into *resolved-* and *direct*-coupling models. The idea of a resolved pomeron coupling follows the proposal of Ingelman and Schlein [29] to treat the pomeron as an hadronic particle with its momentum distributed between constituent partons. In this interpretation those quarks and gluons which the pomeron couples to in interactions can be considered to be constituents of the pomeron and therefore are close to mass shell. In such a scheme the idea of a "pomeron structure function" is well-defined, in direct analogy with the proton structure function. Experimentally, therefore, one can use diffractive scattering data in which a resolved-coupling pomeron is exchanged to extract the quark content of the pomeron and to infer from this the gluonic structure of the pomeron.

In the simplest resolved-coupling colour-singlet exchange model of the pomeron the diffractive interaction proceeds by the exchange of two non-interacting gluons propagating in a colour-singlet state [30–41]. It is difficult, however, to conceive of a non-interacting system of two gluons propagating together in space in such a way as to form a colour-singlet state. The most sophisticated QCD model is the BFKL pomeron [44, 45, 64] in which a ladder of non-interacting gluons is exchanged[1].

Another model for a resolved-coupling pomeron is the "single-gluon" model [42, 43] in which a gluon carrying most of the momentum of the colour-singlet state is exchanged, with further soft gluons present to "dress" the colour of the hard gluon. A recent H1 analysis [15] suggests that the true picture might be somewhere between these two models. The H1 picture of diffractive DIS is of the pomeron as a two-gluon state in which one gluon carries up to 90 % of the pomeron momentum.

Although the idea of a resolved-coupling pomeron is favoured from a purely QCD viewpoint, the analyses by Ellis *et al* [1, 2] show that there must be a significant contribution to diffractive DIS processes in which the exchanged pomeron and virtual photon interact by the exchange of an off-shell quark (see Sect. 2.5.4). It is hard to reconcile this result with the purely hadronic interpretation of the pomeron.

One way around the problem associated with the virtuality-constraint analyses, while keeping dijet production as the dominant exchange (as expected from standard DIS, of which diffractive processes are a subset), is to allow the pomeron to couple to off-shell quarks in a point-like manner. This approach is an extension of the proton–proton scattering analyses of Donnachie and Landshoff [24–27] and has been discussed in terms of a model in which the pomeron has a point-like scalar coupling to quarks and gluons [48] and in terms of a vector-like coupling to quarks [1, 2, 25, 26].

Direct (photon-like) coupling does not correspond to the usual picture of constituent partons and in this formalism it is not clear how the idea of a partonic substructure of the pomeron fits into such a direct-coupling picture. In such a scenario the idea of a "momentum sum rule", in which the momentum of the pomeron is shared by its constituent partons, is not well defined. Instead, direct couplings are more commonly associated with the photon in which the momentum carried by the parent particle cannot be wholly assigned among a distribution of "constituent" partons.

An interpretation of the Ellis-Ross form factor model of pomeron exchange in a resolved-coupling scenario is discussed below, highlighting the interesting possibility that there may be elements of both resolved and direct coupling in the pomeron.

[1] See [64] for a review of the leading-order BFKL pomeron and [65, 66] for discussion of the next-to-leading-order contribution. The BFKL model is not considered further in this analysis.

3.3 Form Factor Models

3.3.1 Donnachie-Landshoff Form Factor Model

Donnachie and Landshoff extended the idea of pomeron exchange from elastic and diffractive proton–(anti)proton scattering to diffractive deep inelastic scattering observed at HERA [26,46,47]. They assumed a vector-like exchange with even charge conjugation parity and a γ_μ quark–pomeron coupling with coupling strength β_0. In this model pomeron exchange was assumed to proceed by the quark-dominated process of Fig. 1.2. Assuming a point-like quark–pomeron coupling leads to a structure function which is proportional to the photon virtuality, Q^2, a quadratic scaling violation which is not observed in the HERA data. In order to generate a cross section consistent with the observed scaling a *form factor*, $f(k^2)$, is introduced at the quark–pomeron vertex. The simplest choice of this form factor which leads to a scale-invariant diffractive structure function is

$$f(k^2) = \frac{\Lambda^2}{\Lambda^2 - k^2}\,, \tag{3.3.1}$$

where k^2 is the four-momentum squared of the exchanged quark coupling to the pomeron (the other quark at this vertex is near mass shell and hence its momentum may be neglected) and $\Lambda^2 = \mathcal{O}(1\,\mathrm{GeV}^2)$. The Donnachie-Landshoff form factor allows the pomeron to couple to off-shell partons, but leads to the dominant contribution to the diffractive cross section coming from small k^2. This means that this model is sensitive to pseudo-rapidity gap cuts.

In order to reproduce the observed Regge behaviour the pomeron propagator is represented by a factor $s^{\alpha_{I\!P}(t_{I\!P})-1}$, where s is the sub-reaction CMS energy for the interaction in which there is a t-channel exchange of a pomeron trajectory with momentum $t_{I\!P}$. A factor of $3F_1(t_{I\!P})$ is included in cross section calculations for vertices where the pomeron couples to a proton rather than a quark. The Dirac elastic form factor of the proton, $F_1(t_{I\!P})$, is parameterized from low energy electron–proton scattering data to be [25,26,47]

$$F_1(t_{I\!P}) = \frac{4m_P^2 - 2.8t}{4m_P^2 - t}\,\frac{1}{(1 - \frac{t}{0.71})^2}\,. \tag{3.3.2}$$

From soft hadron scattering analyses, Donnachie and Landshoff found $\alpha_{I\!P}(0) \approx 1.08$ [24,27], $\Lambda \approx 1.2\,\mathrm{GeV}$ [46] and they extracted an "effective coupling" for single pomeron exchange in diffractive DIS of $\beta_0^2 \approx 3.4\,\mathrm{GeV}^{-2}$.

In the Donnachie-Landshoff model, one might envisage a coupling of the form $\beta_0 + (k_1^2 + k_2^2)\beta_0'$, for example, where k_1 and k_2 are the momenta of the two quarks to which the pomeron couples. In the proton–proton analyses, the two quarks are near mass shell and the second term in the coupling is negligible. In large pseudo-rapidity gap diffractive DIS, however, one of the momenta is constrained to be large ($\gtrsim 1\,\mathrm{GeV}^2$) and the second contribution cannot be ignored. In this analysis only constant pomeron–quark coupling is considered. One could equally consider a phenomenological model with a more general form factor, for example

$$f(k^2) = \left(\frac{\Lambda^2}{\Lambda^2 - k^2}\right)^n\,. \tag{3.3.3}$$

In the analyses in Chaps. 4 and 5, two values for n are considered: $n = 1$ (Donnachie-Landshoff model) and $n = 0.5$ (Ellis-Ross model). In order to be consistent with scaling of the diffractive structure function, n must be in the range of 0.5 to 1.

3.3.2 Ellis-Ross Form Factor Model

The model suggested by Ellis and Ross [2] is motivated by the observation that diffractive DIS is not particularly sensitive to pseudo-rapidity [10,12,16], as well as by the correlation between exchanged-quark virtuality and pseudo-rapidity. This model adopts the harder choice of form factor

$$f(k^2) = \sqrt{\frac{\Lambda^2}{\Lambda^2 - k^2}}\,. \tag{3.3.4}$$

This form factor leads to a cross section with only a logarithmic dependence on k^2 and therefore allows equal contributions from the entire k^2 spectrum.

Both of the form factor models reduce to the original Donnachie-Landshoff model of hadron–hadron scattering [24–27] for the exchange of a pomeron between two on-shell partons, namely, the exchange of a pomeron between the quark constituents of the (anti)protons.

Ellis-Ross Form Factor Model in a Resolved-Coupling Context

The phenomenological Ellis-Ross model for direct pomeron–parton coupling has an interesting interpretation in the context of a resolved-coupling picture. Consider the QCD diagram shown in Fig. 3.1: Compared with Fig. 1.2, the diagram in Fig. 3.1 contains an extra fermion propagator between the two gluon lines. Keeping the two gluons coupled to the pomeron near mass shell, this extra fermion line has momentum similar to that of the exchanged quark, k^2. When this diagram is squared to obtain the scattering amplitude, an additional factor of $1/k^2$ is obtained compared to Fig. 1.2. This factor is identified with $f^2(k^2)$ of Eq. 3.3.4, in which the Ellis-Ross form factor is interpreted as an effective vertex for the pomeron–quark interaction. As yet there is no full QCD calculation of the interaction in Fig. 3.1.

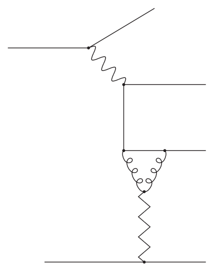

Figure 3.1: *Two-gluon contribution to the Ellis-Ross pomeron form factor.*

In terms of a resolved coupling picture, in the diagram in Fig. 3.1 the two gluons must be near mass shell. This diagram allows the "struck" quark (represented in Figs. 1.2 and 3.1 by vertical lines) to go off mass shell, as off-shell quark–gluon couplings are permitted within QCD. In this diagram, therefore, the struck-quark virtuality is insensitive to large pseudo-rapidity gap cuts. For a wide range of HERA phase space, the diagram of Fig. 3.1 may therefore provide a significant contribution to the pomeron structure.

As with the two-gluon model discussed in Sect. 3.6, this interpretation requires the two gluons to propagate in a colour-singlet state before interacting with the photon system. Since the two gluons in Fig. 3.1 are assumed to be near mass shell, the diagram can be factorized to form a diffractive structure function from which one may attempt to extract a pomeron structure function.

The diffractive DIS model described by the gluon-driven process shown in Fig. 3.1 is attractive as it is physically simple and it also suggests that with a combination of soft scattering experiments and deep-inelastic scattering one can separately probe the quark and the gluon structure of the pomeron. The proton–(anti)proton scattering experiments are interpreted as probing the quark structure of the pomeron, with the exchanged pomeron coupling to constituent quarks within the (anti)protons, and the HERA large pseudo-rapidity gap cut diffractive DIS experiments probe the gluonic structure of the pomeron.

Finally, the two-gluon resolved-coupling picture represented by Fig. 3.1 is expected to have a stronger contribution to the Q^2 evolution of the structure functions than the diagrams of Figs. 1.2 and 1.3 [2]. The inclusion of diagrams such as Fig. 3.1 in the H1 analysis [15] discussed in Sect. 1.6 would lead to a picture of the pomeron with a flatter gluon distribution, as the scaling violations could be accounted for in part by the Q^2 dependence from the additional diagrams.

3.3.3 Non-Covariant Gauge Approach to Form Factor Models

The form factor models of diffractive DIS do not conserve the electromagnetic current and the cross sections calculated in these models depend on the photon gauge used in the calculations [35, 36]. This is because the pomeron couples to partons with the "wrong" charge conjugation parity (C-even coupling, unlike the photon which couples to particles and their anti-particles with the opposite sign). The sum of the diagrams shown in Fig. 3.2 which contribute to two-gluon exchange, however, is an explicitly gauge-invariant quantity. Comparing the two approaches, the diagrams where the colour-singlet exchange is modelled by a hadron-like "pomeron" exclude the two diagrams in which the two gluons do not couple to the same quark line. Furthermore, for large exchanged-quark virtualities the diffractive system is close together and the pomeron would therefore be expected to couple to the quark–antiquark system as a whole [67]. In this case the exclusion of the two non-local coupling diagrams of the two-gluon example is expected to be significant. One might hope for the form factor models to be physically meaningful in a gauge where the contribution from these two diagrams is minimal.

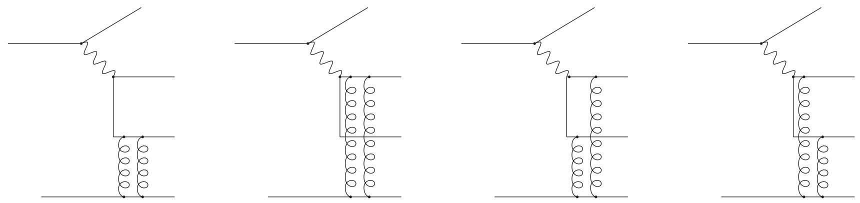

Figure 3.2: *Leading-order diagrams contributing to the two-gluon exchange model of diffractive DIS.*

Diehl [36, 68] has suggested a non-covariant gauge in which the Donnachie-Landshoff form factor model mimics many features of the manifestly gauge-invariant Landshoff-Nachtmann two-gluon model. Diehl's non-covariant gauge choice leads to a tensor structure of the photon propagator of

$$g_{\mu\nu} - \frac{1}{P\cdot q}\left(P^\mu q^\nu + q^\mu P^\nu\right) + \frac{P^2}{(P\cdot q)^2}\, q^\mu q^\nu\,, \tag{3.3.5}$$

where P is the proton momentum and q is the momentum of the photon. The photon propagator tensor structure in the Feynman gauge is $g_{\mu\nu}$. Only one of the extra terms in the non-covariant gauge photon propagator contributes to the scattering cross section when the photon propagator is contracted with the lepton tensor from the upper vertex.

This non-covariant gauge choice, applied to the Donnachie-Landshoff and Ellis-Ross form factor models, amounts to subtracting off the part from the structure function which is of higher twist and which gives an undesirable high-$p_\perp^2$ behaviour. In the Feynman gauge, the form factor models give a contribution to the longitudinal structure function which behaves as $1/Q^2$, which is singular in the photo-production limit [36]. This unphysical behaviour is not present if the models are calculated in the non-covariant gauge. However, since the violation of gauge invariance in these models occurs only in non-leading order in $1/Q^2$, the models calculated in a given gauge may still provide a good approximation to the diffractive scattering cross section, as least for scattering involving highly-virtual photons. In the analyses in Chaps. 4 and 5, the form factor models are calculated in the non-covariant gauge of Eq. 3.3.5 as well as in the Feynman gauge.

An alternative approach to address the gauge-noninvariance of the form factor models is to introduce contact terms [36]. This approach will not be considered in the present analysis.

3.4 Single-Gluon Model

A gauge-invariant model for colour-singlet exchange in diffractive DIS in which the interaction proceeds by the exchange of a single gluon between the proton and the photon diffractive system has been proposed in [42, 43]. In this model, shown in Fig. 3.3, further interactions occur involving soft gluons associated with the colour field of the proton remnant. These additional exchanges are not assumed to affect the dynamics of the interaction, but simply serve to dress the colour of the hard gluon and preserve the pseudo-rapidity gap. In this model, the pseudo-rapidity gap constraints on exchanged-quark virtuality apply to the quark exchanged between the hard gluon and the photon. This picture is consistent with the OPE or related [63, 69] expansions, corresponding to keeping the leading-twist contribution.

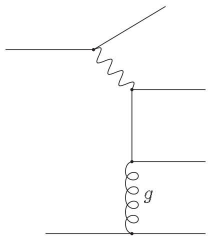

Figure 3.3: *Single-gluon exchange contribution to dijet production in diffractive DIS.*

The single-gluon model arises naturally from a two-gluon scenario such as that discussed in Sects. 3.3.2 and 3.6. In a full two-gluon exchange contribution, as in Figs. 3.1 and 3.2, the diagrams are expected to include the twist-4 operator in OPE language, due to the four-gluon operator in the squared diagram which contributes to the interaction cross section. This contribution would therefore be associated with a $1/Q^2$ suppression of the structure function. However, the diffractive DIS structure function is observed to scale just like the fully-inclusive DIS structure function. This fact suggests that the case in which the single gluon carries the bulk of the pomeron momentum, a single-gluon exchange scenario, is a significant part of the partonic structure of a "two-gluon" model. In a single-gluon exchange leading-twist interpretation, the right-hand gluon in Figs. 3.1 and 3.2 leaves the quark between the two gluons near its mass shell. In this case the hard scattering process involves the left-hand gluon only and the diagram can be identified with the leading twist-two operator. The subsequent soft-scattering process involving the right-hand gluon is included in the soft dressing that is implicitly present in any description of deep-inelastic scattering needed to obtain a final state involving colourless hadrons. Soft final-state parton emissions also contribute to this dressing. In fully-inclusive DIS the sum of such dressing forms a complete sum and thus drops out of the calculation of the total cross section.

Additional soft-gluon exchanges cannot, however, prevent the exponential suppression of the pseudo-rapidity gap in a single-gluon model of soft hadron–hadron scattering and therefore cannot explain the presence of pseudo-rapidity gaps in hadron–hadron data [70].

3.5 Scalar-Pomeron Model

In the scalar-pomeron model [48], the pomeron couples to quarks with a direct point-like coupling, $g_{I\!Pqq}$, and the structure function scales without the need for a form factor at the quark–pomeron vertex. This model features even charge conjugation parity in the pomeron–quark coupling.

The calculations of Vermaseren *et al* [48] include fits also involving the 3-jet diffractive final state. This introduces a further parameter, the pomeron–gluon point-like scalar coupling, $g_{I\!Pgg}$, and a further 800 terms into the calculation which are not readily incorporated into a phase space constraint analysis. In the analyses in Chaps. 4 and 5 only the dijet component of the scalar-pomeron model is studied.

3.6 Two-Gluon Model

Diffractive scattering via the exchange of two non-interacting gluons between the proton and photon systems has been extensively studied [30–36, 38, 42, 43, 59, 60]. This is the simplest partonic model of the pomeron because at least two gluons are needed to produce the colour-singlet exchange required for the presence of a non-suppressed pseudo-rapidity gap.

The leading-order diagrams contributing to two-gluon colour-singlet exchange diffractive DIS are shown in Fig. 3.2. Interpreted in terms of pomeron exchange as a quasi-real particle exchange, only the first two diagrams of Fig. 3.2 are included. The other two diagrams are required to preserve gauge invariance and are expected to be significant for events where there is a small spatial separation of the quark–antiquark pair (in dijet production) because in that case the quark–antiquark system should be considered to be interacting with the gluons as a single object.

The two-gluon model calculations in this chapter and in App. B follow the analysis by Diehl [35] of the Landshoff-Nachtmann model, in which the calculations were presented in a form which is well-suited to a phase-space constraint analysis. In this approach, the colour-singlet system is interpreted as two non-interacting gluons with non-perturbative propagators. The approach of Nikolaev and Zakharov [33] is similar, the main difference being the use of perturbative propagators.

A full two-gluon calculation is non-trivial because the exchange must satisfy physical observations, such as approximate C-even vector-like coupling in proton–proton elastic and diffractive scattering and the two gluons must propagate in a colour-singlet state to produce the observed pseudo-rapidity gap[2].

The behaviour of the two-gluon model at small β is strongly dependent on the low-transverse momentum cut-off imposed by pseudo-rapidity gap cuts. This effect is demonstrated analytically in Sect. 3.8.5 and is noticeable in the structure function analysis in Chap. 4.

3.7 3-Jet Final-State Contribution

Recent H1 analyses [15, 49] suggest that a large proportion of the diffractive DIS sample can be described by diagrams of the form of Fig. 1.3(b), in which the dominant contribution involves a pomeron–gluon coupling. H1 [15] fit diffractive structure function data using

[2] An interesting approach to the problem of creating the gluon pairs in colour-singlet states has been suggested by Hautmann *et al* [63].

the diagrams of Figs. 1.2 and 1.3, which favoured a strongly peaked gluon component with one very hard gluon. However, the H1 calculation considered only the resolved-coupling component of the pomeron, assuming the exchanged gluon in Fig. 1.3 is near mass shell. It is argued in Sect. 2.5.4 and Sect. A.4 that these resolved-coupling diagrams are unable to describe large pseudo-rapidity gap data because the constraints on exchanged-parton virtuality apply to the exchanged parton coupling to the pomeron. Further, it was suggested in [2] that the contribution from Fig. 3.1 might have significant scaling violations which, if included in the H1 fit, would enable a flatter gluon momentum distribution to be fitted to the observed diffractive structure function scaling violations.

There is no prescription in the Ellis-Ross or Donnachie-Landshoff models to calculate the pomeron–gluon coupling in order to calculate the contribution from higher-order diffractive final states. In other models the introduction of gluons in the diffractive final state introduces further parameters, such as the pomeron–gluon coupling constant in the scalar-pomeron model [48]. One comment that can be made about such events is that the contribution from higher-multiplicity diffractive final states is expected to be significant at low β. This conclusion arises from a consideration of fits of diffractive data taken from the full phase space [59–61]. This is also expected from standard QCD, where the gluon drives the proton structure function at low x_{Bj}, as the parameter β plays the rôle of x_{Bj} in diffractive DIS. It is demonstrated in Sects. 2.5 and A.4 that the phase space constraints introduced by large pseudo-rapidity gap cuts are weaker on multi-jet final state events than on dijet production events and therefore the pseudo-rapidity gap cuts lead to an enhanced 3-jet contribution to the diffractive sample in some regions of HERA parameter space.

It is therefore reasonable to conclude that the phase space-constrained large pseudo-rapidity gap data features a significant 3-jet component at low β.

3.8 Calculations of Cross Sections and Structure Functions

3.8.1 Introduction

The cross section and structure function calculations corresponding to the form factor models (in the Feynman gauge) are presented in this section. Results of calculations for the other colour-singlet exchange models are summarised. Details of the other calculations, some useful kinematic results and a table of Feynman rules appear in App. B. A set of pomeron-exchange "Feynman Rules", which enable systematic cross section calculations to be carried out in the form factor model approach, also appear in App. B.

The process considered in all the calculations in this chapter is electron–proton diffractive deep-inelastic scattering,

$$e^- + P \to e^- + P + q + \bar{q}\,, \tag{3.8.1}$$

where the jets produced by the hadronization of the diffractively-produced quark–antiquark pair are separated from the forward proton direction by a pseudo-rapidity gap of at least $\eta_{\max}$.

The cross section describes the probability for a scattering interaction to occur. Calculationally, it consists of three parts: a *flux factor*, F, which describes the incident particles, a *matrix element*, $\mathcal{M}$, which describes the kinematics of the interaction and a *phase space element*, $\mathrm{d}\Gamma$, which contains information about the distribution of particles and energy in the final state. The cross section can be expressed in terms of these three factors as

$$\mathrm{d}\sigma = \frac{1}{F}\,\overline{|\mathcal{M}|}^2\,\mathrm{d}\Gamma\,. \tag{3.8.2}$$

For electron–proton scattering with a fixed CMS energy the flux factor is (for $S_{\mathrm{Tot}} >> m_P^2$, where m_P is the proton mass)

$$F = 2S_{\mathrm{Tot}}\,. \tag{3.8.3}$$

The phase space element for diffractive dijet production is

$$\mathrm{d}\Gamma = \frac{(2\pi)^4}{((2\pi)^3)^4}\frac{\mathrm{d}^3\underline{p}'_e}{2p'^0_e}\,\frac{\mathrm{d}^3\underline{p}_A}{2{p_A}^0}\,\frac{\mathrm{d}^3\underline{p}_B}{2{p_B}^0}\,\frac{\mathrm{d}^3\underline{P}'}{2P'^0}\,\delta^4(p'_e + p_A + p_B + P' - P - p_e)\,, \tag{3.8.4}$$

where the particle momenta are shown in the first diagram of Fig. 3.4. Following the calculations in App. B, the phase space factor is

$$\mathrm{d}\Gamma = \frac{\mathrm{d}Q^2\mathrm{d}M_X^2\,\mathrm{d}p_\perp^2\,\mathrm{d}x_{I\!P}\mathrm{d}t_{I\!P}\mathrm{d}\phi'}{2^5(2\pi)^6 x_{I\!P} S_{\mathrm{Tot}} M_X^2}\,\frac{1}{\sqrt{1-\frac{4p_\perp^2}{M_X^2}}}\,, \tag{3.8.5}$$

where ϕ' is the azimuthal angle of the outgoing electron and the other variables are as defined in Chap. 2. The differential scattering cross section can be expressed in terms of M_X^2 and the transverse and longitudinal contributions to the diffractive structure function by

$$\frac{\mathrm{d}^3\sigma}{\mathrm{d}Q^2\,\mathrm{d}M_X^2\,\mathrm{d}x_{I\!P}} = \frac{4\pi\alpha_{\mathrm{em}}^2}{Q^4(Q^2+M_X^2)}\left\{[1+(1-y)^2]\,\frac{F_T^{D(3)}}{2} + (1-y)\,F_L^{D(3)}\right\}. \tag{3.8.6}$$

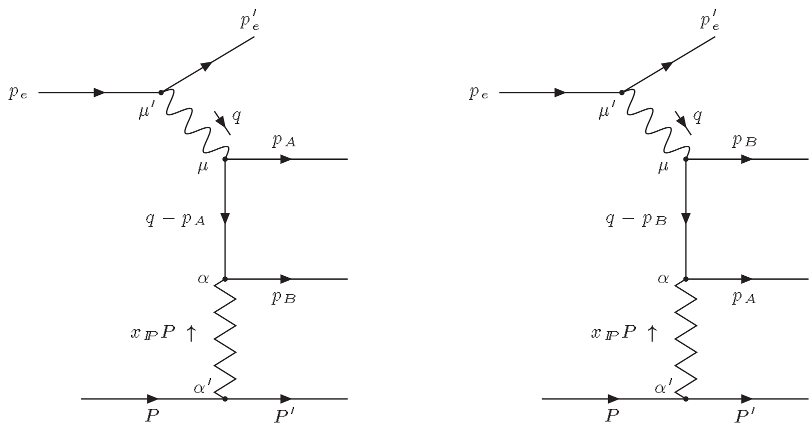

Figure 3.4: *Two diagrams involved in diffractive dijet production via pomeron exchange.*

In the case where the full diffractive DIS sample is extracted from the DIS data, one can determine the approximate behaviour of the diffractive structure function as a function of β, at fixed Q^2 and $x_{I\!P}$, by looking at the behaviour of $F_2^{D(3)}$ at small virtuality, k^2. Equivalently, the structure function can be studied at fixed Q^2 and $x_{I\!P}$ at small $p_\perp^2$. This will also give and approximation of the β dependence of the pomeron structure function, as small k^2 (and small $p_\perp^2$) events provide the dominant contribution to the diffraction structure function. At small exchanged-quark virtualities, k^2 and $p_\perp^2$ are related by

$$p_\perp^2 \approx -(1-\beta)k^2\,. \tag{3.8.7}$$

In data for which large pseudo-rapidity gap cuts impose strong constraints on the phase space through the lower limit of $p_\perp^2$, there is an additional contribution to the β

dependence of the diffractive structure function. Table 2.2 shows that $p^2_{\perp\,\mathrm{min}}$ increases approximately linearly with decreasing β, demonstrating that pseudo-rapidity gap cuts introduce a significant β dependence into the data extracted by this means. There is also a mild Q^2 dependence introduced through $p^2_{\perp\,\mathrm{min}}$. This is an important effect since, in analyses such as [15], the gluon distribution is extracted by fitting the Q^2 and β dependence of the pomeron structure function.

The scaling behaviour and the β-dependence of the dijet component of the colour-singlet models, with and without significant phase space constraints, are discussed below.

3.8.2 Form Factor Models

The invariant matrix element is calculated by squaring the two diagrams in Fig. 3.4. The first diagram represents a quark flowing through the centre of the diagram and in the second diagram the quark line flows in the opposite direction. This leads to four terms, one for the square of each diagram and two mixed terms. The matrix element includes a sum over the spins of the incoming particles and an average over the spins of the final-state particles. The full contribution to the matrix element is therefore

$$\overline{|\mathcal{M}|}^2 = \overline{|\mathcal{M}_1|}^2 + \overline{|\mathcal{M}_2|}^2 + \overline{|\mathcal{M}_{12}|} + \overline{|\mathcal{M}_{21}|}\,, \tag{3.8.8}$$

The first term, $\overline{|\mathcal{M}_1|}^2$, of the invariant amplitude for the form factor model is obtained by squaring the first diagram of Fig. 3.4. Applying the rules in App. B gives

$$\begin{aligned}
\overline{|\mathcal{M}_1|}^2 = & \sum_q e^4 e_q^2 \frac{g^{\mu\mu'} g^{\nu\nu'}}{q^4} \frac{\delta^{\alpha\alpha'}\delta^{\beta\beta'}}{(q-p_A)^4} \frac{1}{2} [3F_1(t_{I\!P})]^2 \beta_0^4 \\
& f((q-p_A)^2) f((q-p_A)^2) s_{D_1}^{2[\alpha_{I\!P}(t_{I\!P})-1]} \frac{1}{2} \mathrm{Tr}\,[\not{p}_e \gamma_{\mu'} \not{p}'_e \gamma_{\nu'}] \\
& \mathrm{Tr}\,[\gamma_\mu (\not{q} - \not{p}_A) \gamma_\alpha \not{p}_B \gamma_\beta (\not{q} - \not{p}_A) \gamma_\nu \not{p}_A]\, \mathrm{Tr}\,[\not{P} \gamma_{\alpha'} \not{P}' \gamma_{\beta'}] \\
= & \sum_q \frac{9}{4} \frac{e^4\, e_q^2\, \beta_0^4\, [F_1(t_{I\!P})]^2}{t^2\, Q^4} f(t)^2\, s_{D_1}^{2[\alpha_{I\!P}(t_{I\!P})-1]} \mathrm{Tr}\,[\not{p}_e \gamma^\mu \not{p}'_e \gamma^\nu] \\
& \mathrm{Tr}\,[\gamma_\mu (\not{q} - \not{p}_A) \gamma_\alpha \not{p}_B \gamma_\beta (\not{q} - \not{p}_A) \gamma_\nu \not{p}_A]\, \mathrm{Tr}\,[\not{P} \gamma^\alpha \not{P}' \gamma^\beta]\,,
\end{aligned} \tag{3.8.9}$$

where t is the t-channel momentum of the $\gamma^* - I\!P$ sub-reaction, s_{D_1} is the sub-energy between the final-state proton and the quark labeled p_B, $f(t)$ is the form factor at the virtual quark–pomeron vertex, $F_1(t_{I\!P})$ is the proton elastic form factor, β_0 is the quark–pomeron coupling constant and e_q is the fraction of electron charge carried by a quark of flavour q. The sum is over the three light quark flavours.

The proton trace can be simplified by using the fact that the quarks are massless, $x_{I\!P}$ is small and the proton mass can be neglected relative to other momentum scales, giving

$$\mathrm{Tr}\,[\not{P} \gamma^\alpha \not{P}' \gamma^\beta] \approx 2[4P^\alpha P^\beta - m_P^2 g^{\alpha\beta}] \approx 8 P^\alpha P^\beta\,. \tag{3.8.10}$$

Momentum conservation in the virtual photon–pomeron system, $q - p_A = p_B - x_{I\!P} P$, allows further simplification since $(\not{p}_A - \not{q})\,\not{P} = (x_{I\!P} \not{P} - \not{p}_B)\not{P} \approx -\not{p}_B \not{P}$. Using the identities in Sect. B.2, the traces in Eq. 3.8.9 can be written

$$\begin{aligned}
& \mathrm{Tr}\,[\not{p}_e \gamma^\mu \not{p}'_e \gamma^\nu] \mathrm{Tr}\,[\gamma_\mu (\not{q} - \not{p}_A) \gamma_\alpha \not{p}_B \gamma_\beta (\not{q} - \not{p}_A) \gamma_\nu \not{p}_A]\, \mathrm{Tr}\,[\not{P} \gamma^\alpha \not{P}' \gamma^\beta] \\
& = \mathrm{Tr}\,[\not{p}_e \gamma^\mu \not{p}'_e \gamma^\nu] \mathrm{Tr}\,[\gamma_\mu (\not{p}_B - x_{I\!P} \not{P}) \gamma_\alpha \not{p}_B \gamma_\beta (\not{p}_B - x_{I\!P} \not{P}) \gamma_\nu \not{p}_A]\, \mathrm{Tr}\,[\not{P} \gamma^\alpha \not{P}' \gamma^\beta] \\
& \approx 2^3\, \mathrm{Tr}\,[\not{p}_e \gamma^\mu \not{p}'_e \gamma^\nu] \mathrm{Tr}\,[\gamma_\mu \not{p}_B \not{P} \not{p}_B \not{P} \not{p}_B \gamma_\nu \not{p}_A] \\
& \approx 2^5 (P \cdot p_B)^2\, \mathrm{Tr}\,[\not{p}_e \gamma^\mu \not{p}'_e \gamma^\nu] \mathrm{Tr}\,[\gamma \not{p} \not{B} \gamma_\nu \not{p}_A]
\end{aligned}$$

$$\approx \frac{2^3 t^2}{x_{I\!P}{}^2}\,\mathrm{Tr}\,[\not{p}_e\gamma^\mu \not{p}'_e\gamma^\nu]\mathrm{Tr}\,[\gamma_\mu\not{p}_B\gamma_\nu\not{p}_A]$$
$$= \frac{2^8 t^2}{x_{I\!P}{}^2}\,[(p_e\cdot p_A)\,(p'_e\cdot p_B)+(p_e\cdot p_B)\,(p'_e\cdot p_A)]\ . \tag{3.8.11}$$

Therefore

$$\overline{|\mathcal{M}_1|^2} = \sum_q 9\frac{2^8 e^4\, e_q^2\,\beta_0^4\,[F_1(t_{I\!P})]^2}{x_{I\!P}{}^2\,Q^4}\,f(t)^2\,s_{D_1}^{2[\alpha_{I\!P}(t_{I\!P})-1]}\,[(p_e\cdot p_A)\,(p'_e\cdot p_B)+ (p_e\cdot p_B)\,(p'_e\cdot p_A)]\ . \tag{3.8.12}$$

The second squared term in the matrix element is obtained by exchanging p_A with p_B and t with u in Eq. 3.8.12, where s, t and u are the usual Mandelstam variables of the $\gamma^* - I\!P$ sub-reaction and introducing the exchanged quark–proton sub-energy s_{D_2} of the second diagram in Fig. 3.4 in place of s_{D_1}, giving

$$\overline{|\mathcal{M}_2|^2} = \sum_q 9\frac{2^8 e^4\, e_q^2\,\beta_0^4\,[F_1(t_{I\!P})]^2}{x_{I\!P}{}^2\,Q^4}\,f(u)^2\,s_{D_2}^{2[\alpha_{I\!P}(t_{I\!P})-1]}\,[(p_e\cdot p_A)\,(p'_e\cdot p_B)+ (p_e\cdot p_B)\,(p'_e\cdot p_A)]\ . \tag{3.8.13}$$

The contribution from the two mixed diagrams must also be calculated. The first of these diagrams gives

$$\begin{aligned}\overline{|\mathcal{M}_{12}|} &= \sum_q (-)e^4 e_q^2\,\frac{g^{\mu\mu'}g^{\nu\nu'}}{q^4}\,\delta^{\alpha\alpha'}\delta^{\beta\beta'}\,\frac{1}{(q-p_A)^2(q-p_B)^2}\\ &\quad f((q-p_A)^2)f((q-p_B)^2)\,\frac{1}{2}\,[3F_1(t_{I\!P})]^2\beta_0^4\,\cdot\\ &\quad s_{D_1}^{\alpha_{I\!P}(t_{I\!P})-1}s_{D_2}^{\alpha_{I\!P}(t_{I\!P})-1}(-)\frac{1}{2}\mathrm{Tr}\,[\not{p}_e\gamma_{\mu'}\not{p}'_e\gamma_{\nu'}]\\ &\quad \mathrm{Tr}\,[\gamma_\mu(\not{q}-\not{p}_A)\gamma_\alpha\not{p}_B\gamma_\nu(\not{p}_B-\not{q})\gamma_\beta\not{p}_A]\,\mathrm{Tr}\,[\not{P}\gamma_{\alpha'}\,\not{P}'\gamma_{\beta'}]\\ &= \sum_q \frac{9}{4}\frac{e^4\,e_q^2\,\beta_0^4\,F_1(t_{I\!P})^2}{tu\,Q^4}\,f(t)\,f(u)\,s_{D_1}^{\alpha_{I\!P}(t_{I\!P})-1}s_{D_2}^{\alpha_{I\!P}(t_{I\!P})-1}\,.\\ &\quad \mathrm{Tr}\,[\not{p}_e\gamma^\mu\not{p}'_e\gamma^\nu]\mathrm{Tr}\,[\gamma_\mu(\not{q}-\not{p}_A)\gamma_\alpha\not{p}_B\gamma_\nu(\not{p}_B-\not{q})\gamma_\beta\not{p}_A]\,\mathrm{Tr}\,[\not{P}\gamma^\alpha\,\not{P}'\gamma^\beta]\,,\end{aligned} \tag{3.8.14}$$

where the trace can be simplified following

$$\begin{aligned}&\mathrm{Tr}\,[\not{p}_e\gamma^\mu\not{p}'_e\gamma^\nu]\mathrm{Tr}\,[\gamma_\mu(\not{q}-\not{p}_A)\gamma_\alpha\not{p}_B\gamma_\nu(\not{p}_B-\not{q})\gamma_\beta\not{p}_A]\,\mathrm{Tr}\,[\not{P}\gamma^\alpha\,\not{P}'\gamma^\beta]\\ &\quad = 8\,\mathrm{Tr}\,[\not{p}_e\gamma^\mu\not{p}'_e\gamma^\nu]\,\mathrm{Tr}\,[\gamma_\mu(\not{p}_B - x_{I\!P}\,\not{P})\,\not{P}\not{p}_B\gamma_\nu(x_{I\!P}\,\not{P}-\not{p}_A)\,\not{P}\not{p}_A]\\ &\quad \approx 8\,\mathrm{Tr}\,[\not{p}_e\gamma^\mu\not{p}'_e\gamma^\nu]\,\mathrm{Tr}\,[\,\gamma_\mu\not{p}_B\,\not{P}\not{p}_B\gamma_\nu\not{p}_A\,\not{P}\not{p}_A]\\ &\quad \approx 2^5\,\mathrm{Tr}\,[\not{p}_e\gamma^\mu\not{p}'_e\gamma^\nu]\,(P\cdot p_B)(P\cdot p_A)\mathrm{Tr}\,[\gamma_\mu\not{p}_B\gamma_\nu\not{p}_A]\\ &\quad \approx \frac{2^3 tu}{x_{I\!P}{}^2}\,\mathrm{Tr}\,[\not{p}_e\gamma^\mu\not{p}'_e\gamma^\nu]\mathrm{Tr}\,[\gamma_\mu\not{p}_B\gamma_\nu\not{p}_A]\\ &\quad \approx \frac{2^8 tu}{x_{I\!P}{}^2}\,[(p_e\cdot p_A)\,(p'_e\cdot p_B)+(p_e\cdot p_B)\,(p'_e\cdot p_A)]\ .\end{aligned} \tag{3.8.15}$$

The other mixed term, $\overline{|\mathcal{M}_{21}|}$, is identical to $\overline{|\mathcal{M}_{12}|}$.

Acceptance cuts restrict $t_{I\!P}$ to $|t_{I\!P}| \lesssim 1\,\mathrm{GeV}^2$, with an approximately exponentially decreasing dependence of the cross section on $t_{I\!P}$ [14]. In the following calculations an implicit integration over $t_{I\!P}$ is assumed. This absorbs the integral over $F_1(t_{I\!P})$ into the overall normalisation. (The overall normalisation is the free parameter of this calculation. The integral over $t_{I\!P}$ introduces an extra dimension of energy^2.) The pomeron trajectory, $\alpha_{I\!P}(t_{I\!P})$, is then approximated by its intercept, $\alpha_{I\!P}(0)$.

The factors involving p'_e can be written in terms of the incoming electron momentum, the diffractive final-state quark momenta and the Mandelstam variables s, t and u of the photon–pomeron scattering sub-process as

$$\begin{aligned}&[(p_e \cdot p_A)\,(p'_e \cdot p_B) + (p_e \cdot p_B)\,(p'_e \cdot p_A)] \\ &\quad = 2[-s\, p_e \cdot p_A - t\, p_e \cdot p_A + Q^2\, p_e \cdot p_B + t\, p_e \cdot p_B + 4\, p_e \cdot p_A\, p_e \cdot p_B]\,.\end{aligned} \tag{3.8.16}$$

The full diffractive scattering cross section for the form factor dijet-production models is therefore

$$\begin{aligned}\mathrm{d}\sigma = 18\, e^4 e_q^2 \beta_0^4\, &\frac{\mathrm{d}Q^2 \mathrm{d}M_X^2 \mathrm{d}p_\perp^2 \mathrm{d}x_{I\!P} \mathrm{d}\phi'}{(2\pi)^6 {x_{I\!P}}^3 {S_{\mathrm{Tot}}}^2 Q^4 M_X^2} \frac{1}{\sqrt{1-\frac{4p_\perp^2}{M_X^2}}} [-s\, p_e \cdot p_A - t\, p_e \cdot p_A + \\ &Q^2\, p_e \cdot p_B + t\, p_e \cdot p_B + 4\, p_e \cdot p_A\, p_e \cdot p_B]\,[f(t)^2\, s_{D_1}^{2(\alpha_{I\!P}(t_{I\!P})-1)} + \\ &f(u)^2\, s_{D_2}^{2(\alpha_{I\!P}(t_{I\!P})-1)} + 2f(t)\, f(u) s_{D_1}^{\alpha_{I\!P}(t_{I\!P})-1} s_{D_2}^{\alpha_{I\!P}(t_{I\!P})-1}]\,,\end{aligned} \tag{3.8.17}$$

where e_q^2 should be summed over the three light quark flavours. The $x_{I\!P}$-dependence, ${x_{I\!P}}^{2\alpha_{I\!P}(0)-1}$, arises because the $s_{D_{1,2}}$ are proportional to $1/x_{I\!P}$ and a factor of $x_{I\!P}$ comes from the phase space element. It can be shown that

$$\begin{aligned}&\int_{\phi'=0}^{2\pi} \mathrm{d}\phi'\,[-s\, p_e \cdot p_A - t\, p_e \cdot p_A + Q^2\, p_e \cdot p_B + t\, p_e \cdot p_B + 4\, p_e \cdot p_A\, p_e \cdot p_B] \\ &= \frac{\pi {x_{I\!P}}^2 s_{\mathrm{Tot}}^2}{(Q^2+M_X^2)^2} \left\{ (Q^2 M_X^2 - 2Q^2 p_\perp^2)\,[1+(1-y)^2] + \frac{2p_\perp^2}{M_X^2}(Q^2 - M_X^2)^2\,(1-y) \right\},\end{aligned} \tag{3.8.18}$$

giving, finally,

$$\begin{aligned}\frac{\mathrm{d}\sigma}{\mathrm{d}Q^2\, \mathrm{d}M_X^2\, \mathrm{d}p_\perp^2\, \mathrm{d}x_{I\!P}} &= \frac{9\, 2^4 e^4 e_q^2 \beta_0^4 b^2}{(Q^2+M_X^2)^2\, Q^4\, x_{I\!P}\, (2\pi)^5 M_X^2} \frac{1}{\sqrt{1-\frac{4p_\perp^2}{M_X^2}}} \\ &\left\{ (Q^2 M_X^2 - 2Q^2 p_\perp^2)\,[1+(1-y)^2] + \frac{2p_\perp^2}{M_X^2}(Q^2 - M_X^2)^2\,(1-y) \right\} \\ &[f(t)^2\, s_{D_1}^{2[\alpha_{I\!P}(0)-1]} + f(u)^2\, s_{D_2}^{2[\alpha_{I\!P}(0)-1]} + 2f(t)\, f(u) s_{D_1}^{\alpha_{I\!P}(0)-1} s_{D_2}^{\alpha_{I\!P}(0)-1}]\,,\end{aligned} \tag{3.8.19}$$

where b is a constant with dimensions of energy which is introduced to account for the integral over $t_{I\!P}$.

The transverse and longitudinal structure function components can be extracted from this form of the cross section and are given by

$$
\begin{aligned}
F_T^{D(3)} \propto \int_{p_\perp^2} & \frac{1}{(Q^2+M_X^2)M_X^2} \frac{1}{x_{I\!P}{}^{2\alpha_{I\!P}(0)-1}} \frac{1}{\sqrt{1-\frac{p_\perp^2}{4M_X^2}}} \{Q^2 M_X^2 - 2Q^2 p_\perp^2\} \\
& [f(t)^2 + 2f(t)f(u) + f(u)^2]\,, \\
F_L^{D(3)} \propto \int_{p_\perp^2} & \frac{1}{(Q^2+M_X^2)M_X^2} \frac{1}{x_{I\!P}{}^{2\alpha_{I\!P}(0)-1}} \frac{1}{\sqrt{1-\frac{p_\perp^2}{4M_X^2}}} \frac{p_\perp^2}{M_X^2}(Q^2 - M_X^2)^2 \\
& [f(t)^2 + 2f(t)f(u) + f(u)^2]\,.
\end{aligned}
\tag{3.8.20}
$$

In both cases the extra t and u dependence from the diffractive energies is small and has been neglected.

In the Donnachie-Landshoff form factor model, in the case that the data selection cuts do not place a significant lower limit on $p_{\perp\,\mathrm{min}}^2$, the structure function behaves at small $p_\perp^2$ and fixed $x_{I\!P}$ approximately as

$$
\begin{aligned}
F_2^{D(3)} &\sim \int_0^{M_X^2/4} \frac{Q^2}{(Q^2+M_X^2)M_X^2} \frac{1}{(\Lambda^2 + \frac{p_\perp^2}{(1-\beta)})^2}\, \mathrm{d}p_\perp^2 \\
&\approx \beta(1-\beta)\,.
\end{aligned}
\tag{3.8.21}
$$

This is the expected β dependence of the Donnachie-Landshoff model for the full diffractive DIS calculation [47]. The diffractive structure function $F_2^{D(3)}$ scales with Q^2.

In the case that the pseudo-rapidity gap data selection cuts restrict the transverse momentum variable by imposing the lower limit $p_{\perp\,\mathrm{min}}^2 \geq$ a few GeV^2, the structure function behaviour is modified to

$$
\begin{aligned}
F_2^{D(3)} &\sim \int_{p_{\perp\,\mathrm{min}}^2}^{M_X^2/4} \frac{Q^2}{(Q^2+M_X^2)M_X^2} \frac{1}{(\Lambda^2 + \frac{p_\perp^2}{(1-\beta)})^2}\, \mathrm{d}p_\perp^2 \\
&\sim \beta(1-\beta) \left[\frac{1}{\Lambda + \frac{p_\perp^2}{1-\beta}} \right]_{p_{\perp\,\mathrm{min}}^2}^{M_X^2/4} \\
&\approx \frac{1}{p_{\perp\,\mathrm{min}}^2} \beta(1-\beta)^2 \\
&\sim \beta(1-\beta)^2\,.
\end{aligned}
\tag{3.8.22}
$$

With the phase space effects, the Donnachie-Landshoff structure function still approximately scales, although there is a Q^2 dependence introduced through $p_{\perp\,\mathrm{min}}^2$.

For the full diffractive DIS contribution the Ellis-Ross form factor model behaves approximately as

$$
\begin{aligned}
F_2^{D(3)} &\sim \int_0^{M_X^2/4} \frac{Q^2}{(Q^2+M_X^2)M_X^2} \frac{1}{(\Lambda^2 + \frac{p_\perp^2}{(1-\beta)})}\, \mathrm{d}p_\perp^2 \\
&\approx \beta(1-\beta)\, \ln\left\{\Lambda^2 + \frac{p_\perp^2}{(1-\beta)}\right\}\Bigg]_0^{M_X^2/4} \\
&\approx \beta(1-\beta)\, \ln\left\{\frac{M_X^2}{4\Lambda^2}\right\}
\end{aligned}
$$

$$= \beta(1-\beta)\ \ln\left\{\frac{Q^2}{4\Lambda^2}\left(\frac{1}{\beta}-1\right)\right\}\,. \tag{3.8.23}$$

The additional Q^2 scaling violations from the choice of Ellis-Ross form factor can be seen in Eq. 3.8.23. There is also a relative enhancement of the diffractive structure function at small β due to the presence of β in the log. The phase space-constrained Ellis-Ross diffractive structure function behaves, at fixed $x_{I\!P}$, approximately as

$$\begin{aligned} F_2^{D(3)} &\sim \int_{p^2_{\perp\,\mathrm{min}}}^{M_X^2/4} \frac{Q^2}{(Q^2+M_X^2)M_X^2}\,\frac{1}{(\Lambda^2+\frac{p_\perp^2}{(1-\beta)})}\,\mathrm{d}p_\perp^2 \\ &\approx \beta(1-\beta)\ \ln\left\{\Lambda^2+\frac{p_\perp^2}{(1-\beta)}\right\}\Bigg]_{p^2_{\perp\,\mathrm{min}}}^{M_X^2/4} \\ &\approx \beta(1-\beta)\ \ln\left\{\frac{M_X^2}{4p^2_{\perp\,\mathrm{min}}}\right\} \\ &= \beta(1-\beta)\ \ln\left\{\frac{Q^2}{4p^2_{\perp\,\mathrm{min}}}\left(\frac{1}{\beta}-1\right)\right\}\,. \end{aligned} \tag{3.8.24}$$

3.8.3 Single-Gluon Model

Details of the single-gluon exchange model calculations appear in Sect. B.3.4. The full single-gluon exchange diffractive scattering cross section is

$$\begin{aligned} \mathrm{d}\sigma = {} & \frac{\mathrm{d}Q^2\mathrm{d}M_X^2\mathrm{d}p_\perp^2\,\mathrm{d}x_{I\!P}\mathrm{d}t_{I\!P}\mathrm{d}\phi}{2^2(2\pi)^6 m_P^2 {x_{I\!P}}^4 {S_{\mathrm{Tot}}}^2 M_X^2 Q^4}\,\frac{e^4 e_q^2}{\sqrt{1-\frac{4p_\perp^2}{M_X^2}}}\Bigg\{4x_{I\!P}S_{\mathrm{Tot}}\left(\frac{p_e\cdot p_A}{t}+\frac{p_B\cdot p_e}{u}\right) \\ & -Q^2\left(\frac{u}{t}+\frac{t}{u}\right)-2\frac{Q^2M_X^2}{tu}+2\mathrm{Tr}\left[\not{p}_A\not{p}_e(\not{q}-\not{p}_A)(\not{p}_B-\not{q})\not{p}_e\not{p}_B\right]\Bigg\}\,, \end{aligned} \tag{3.8.25}$$

where the cross section is to be summed over light quark flavours. This cross section was used in this form in the structure function and transverse momentum distribution calculations of Chaps. 4 and 5.

3.8.4 Scalar-Pomeron Model

Details of the scalar-pomeron model cross section and structure function calculations appear in Sect. B.3.5. The electron–proton diffractive scattering cross section in this model is

$$\begin{aligned} \mathrm{d}\sigma = {} & \frac{\mathrm{d}Q^2\mathrm{d}M_X^2\mathrm{d}p_\perp^2\,\mathrm{d}x_{I\!P}\mathrm{d}t_{I\!P}\mathrm{d}\phi}{2^5(2\pi)^6 9{S_{\mathrm{Tot}}}^2 m_P^2[F_1(t_{I\!P})]^2M_X^2Q^4x_{I\!P}}\,\frac{e^4e_q^2g_{I\!Pqq}^4\,(Q^2+M_X^2)}{\sqrt{1-\frac{4p_\perp^2}{M_X^2}}} \\ & Q^2{x_{I\!P}}^2{S_{\mathrm{Tot}}}^2[1+(1-y)^2]\,, \end{aligned} \tag{3.8.26}$$

where $g_{I\!Pqq}$ is the coupling constant at the quark–antiquark–pomeron vertex, a sum over the light quarks is assumed and terms of order $m_P^2{x_{I\!P}}^2$ are neglected. The scalar-pomeron diffractive structure function is entirely transverse and is evident from Eq. 3.8.26.

There is little effect on the Q^2 or β dependence of the diffractive structure function if the $p_\perp^2$ range is restricted by pseudo-rapidity gap cuts.

3.8.5 Two-Gluon Model

Details of the Landshoff-Nachtmann two-gluon exchange model calculations appear in [35] and in Sect. B.3.6. The full two-gluon exchange pomeron structure function for phase space-constrained large pseudo-rapidity gap cut diffractive scattering is

$$
\begin{aligned}
F_T^{I\!P} &\approx \int_{p_\perp^2} \frac{3\beta_0^2\mu_0^4\beta^3}{\pi^2(Q^2+M_X^2)^2} \frac{1}{\sqrt{1-\frac{4p_\perp^2}{M_X^2}}} \frac{1}{p_\perp^4} \left(M_X^2 - 2p_\perp^2\right) , \\
F_L^{I\!P} &\approx \int_{p_\perp^2} \frac{3\beta_0^2\mu_0^4\beta^2}{\pi^2} \frac{1}{\sqrt{1-\frac{4p_\perp^2}{M_X^2}}} \frac{1}{p_\perp^2} \frac{(Q^2-M_X^2)}{(Q^2+M_X^2)^2} .
\end{aligned}
\tag{3.8.27}
$$

The cross section and structure function results calculated in this chapter are used in Chaps. 4 and 5 to compare the colour-singlet exchange models with large pseudo-rapidity gap cut diffractive DIS data.

Chapter 4

Comparison With Data I: Structure Function Analysis

4.1 Introduction

In this chapter five models of the colour-singlet exchange process underlying diffractive DIS are compared with large pseudo-rapidity gap cut diffractive structure function data. Data is chosen for which the pseudo-rapidity gap cut restricts the available final-state phase space.

A comparison of the structure function calculations from the colour-singlet exchange models with this data provides a new way of testing diffractive DIS models. As discussed in [1, 2] and in Sect. 3.2, events selected using a strong pseudo-rapidity gap cut offer a way of discriminating between models with direct and resolved couplings. Furthermore, large pseudo-rapidity gap data corresponding to significant phase space constraints allows a study of the large transverse momentum structure of the models. This analysis also highlights the discussion of Sect. 2.5.5 in which the breakdown of factorization of the diffractive structure function into a pomeron structure function and a pomeron flux factor is explained.

The structure function analysis results favour a dijet diffractive final state described by the Ellis-Ross form factor model and the fits are marginally acceptable for the colour-singlet single-gluon model and the scalar-pomeron model. The fits for the two-gluon and Donnachie-Landshoff models suggest that a significant contribution is required from high-multiplicity diffractive final states in addition to dijet events. Further experiments are suggested to refine the conclusions of this analysis.

4.2 Description of HERA Structure Function Data

The data used in this analysis [57] is chosen for which the data selection cuts constrain the exchanged quark in diagrams such as Figs. 1.2 to be off mass shell and corresponds to selecting data for which the transverse momentum of the diffractive final state is also large. The parameters of the large pseudo-rapidity gap cut data are shown in Table 2.2. The experimental cut on pseudo-rapidity is $\eta_{\max} = 1.8$, corresponding to a pseudo-rapidity cut at parton level of $\eta^{\rm th}_{\max} \approx 1.3$. The photon virtuality ranges from $8.5\,\mathrm{GeV}^2$ to $50\,\mathrm{GeV}^2$, there are four β values between 0.065 and 0.65 and, apart from two points, $x_{I\!P} < 0.05$. Table 2.2 also shows the minimum exchanged-quark virtuality and transverse momentum corresponding to the pseudo-rapidity gap cut and the kinematic parameters of the data. The virtuality constraints rule out any contribution to this data from resolved-coupling dijet production. Furthermore, 85 % of the data sample corresponds to regions where resolved-coupling multi-jet events are also not selected.

4.3 Fits of Models to Diffractive Structure Function Data

In this section diffractive structure function calculations from the models described in Chap. 3 are compared with large pseudo-rapidity gap cut data.

The solid points in all of the graphs are experimental data and the error bars correspond to statistical and systematic errors added in quadrature. The overall normalisation is the sole parameter of each model and is determined by a fit to all the data points. There were 42 data points appropriate for this study and one parameter, the overall normalisation, giving 41 degrees of freedom in the fits.

4.3.1 Form Factor Models

The form factor model fits to large pseudo-rapidity gap cut structure function data (calculated in the Feynman gauge) are shown in Fig. 4.1. These graphs correspond to a pomeron intercept of $\alpha_{I\!P}(0) = 1.08$ and a low-momentum cut-off in the form factor of $\Lambda = 0.2\,\mathrm{GeV}$. The solid line represents the Ellis-Ross model and the dotted line corresponds to the Donnachie-Landshoff model.

The graphs in Fig. 4.1 show log-linear plots of the diffractive structure function, $F_2^{D(3)}$, as a function of $x_{I\!P}$ for a range of Q^2 and β. If $x_{I\!P}$-factorization, predicted by the Ingelman-Schlein interpretation [29] and discussed in Sect. 2.5.5, were satisfied then, in the absence of contributions from additional Reggeon exchanges, these plots would be straight lines, with the slope related to the pomeron intercept. The contribution from other Reggeon exchanges is significant at large $x_{I\!P}$ and therefore reduces the slope of the $F_2^{D(3)}$ plot at large $x_{I\!P}$. However the factorization-breaking effects discussed in Sect. 2.5.5 lead to the plot of $\ln F_2^{D(3)}$ against $x_{I\!P}$ tending to fall *below* a straight-line fit in the region where k^2_{min} is large. Figs. 2.9 and 2.10 show that this should also occur at large $x_{I\!P}$. The expected trend in the presence of factorization-breaking effects is, therefore, for the $F_2^{D(3)}$ plots to fall off at large $x_{I\!P}$. This behaviour is present in the form factor models, and there is a mild tendency towards this behaviour in the data (although the contribution from sub-leading Reggeon exchanges will tend to mask this effect in the data) in Fig. 4.1.

The form factor models were also calculated in the non-covariant gauge described in Sect. 3.3.3, as well as with the harder pomeron intercept of $\alpha_{I\!P}(0) = 1.2$ and with $\alpha_{I\!P}(0) = 1$. The fits were also carried out with a low-momentum form factor cut-off of $\Lambda = 1.2\,\mathrm{GeV}$, the value of Λ extracted by Donnachie and Landshoff from exclusive ρ-production data [46].

The Ellis-Ross model with a dijet diffractive final state describes the large pseudo-rapidity gap cut data well over the whole kinematic range for all choices of $\alpha_{I\!P}(0)$, Λ and in both the Feynman gauge and the non-covariant gauge. For example, the χ^2/dof for the Ellis-Ross model for a soft pomeron intercept, $\Lambda = 0.2\,\mathrm{GeV}$ and non-covariant gauge choice is equal to 1. The only mild discrepancy in the Ellis-Ross model appears for the harder intercept where χ^2/dof tends to 1.5. The Donnachie-Landshoff dijet model does not describe the data well, having χ^2/dof of 2 or greater. The Donnachie-Landshoff model falls below the data particularly at small β and at large $x_{I\!P}$. This corresponds to regions where k^2_{min} is constrained to be large and is a consequence of the strong k^2-dependence introduced into the cross section by the $1/k^2$ behaviour of the Donnachie-Landshoff form factor.

Although the analytic $x_{I\!P}$ dependence introduced by hand into each model is the same, the $x_{I\!P}$ dependence of the fits is significantly different between the form factor models. This is because the diffractive structure function is only integrated over the kinematically accessible region of phase space and the low-$p_\perp^2$ cut-off introduced by the pseudo-rapidity gap cuts is $x_{I\!P}$-dependent.

There is little difference between the fits obtained with different choices of pomeron intercept. This indicates that the present phase-space constrained large pseudo-rapidity

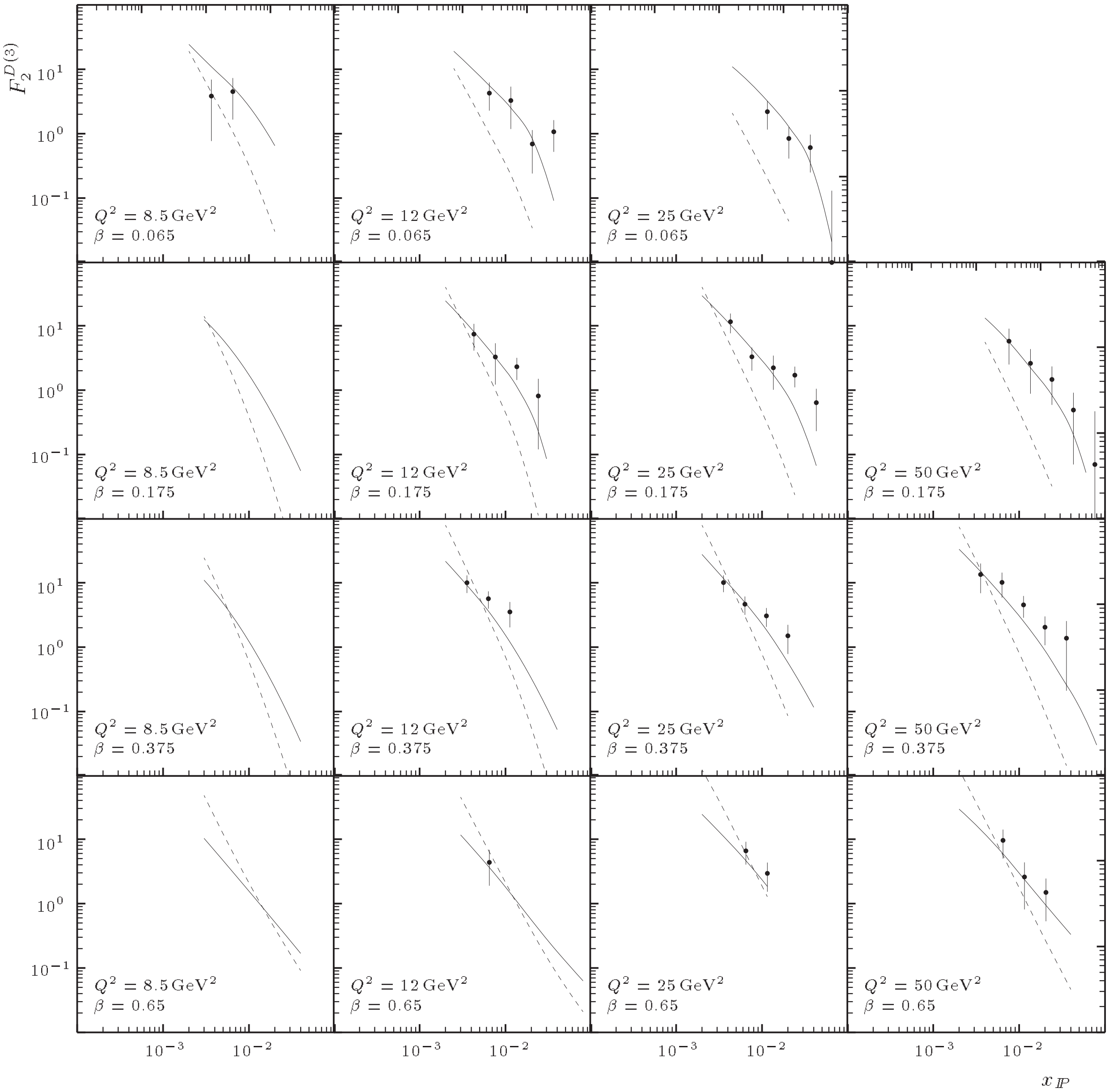

Figure 4.1: *The Ellis-Ross and Donnachie-Landshoff form factor models fitted to diffractive structure function data with a pseudo-rapidity gap cut at hadron level of* $\eta_{\max} = 1.8$. *A pomeron intercept of* $\alpha_{I\!P}(0) = 1.08$ *is assumed and the parameter* Λ *is chosen to be* $0.2\,GeV$ *in the D-L and E-R form factors. The points correspond to H1 data [57] for which the pseudo-rapidity gap cuts impose the constraint* $|k^2_{\min}| > 1\,\mathrm{GeV}^2$ *and the statistical and systematic errors have been added in quadrature. The solid line is the prediction from the E-R model with the overall normalisation determined by a fit to the data points. The dashed line is the D-L model with the same normalisation procedure.*

gap data are not sufficiently precise to improve the present knowledge of the pomeron intercept. The larger low-momentum cut-off in the form factors provides a better fit to the data in the Donnachie-Landshoff model, but does not change the overall qualitative features of the fits. The reason that the models are not sensitive to the low-momentum cut-off is that most of the data studied in this analysis corresponds to an exchanged-quark virtuality of $k^2 \gtrsim$ a few GeV^2 in the form factors, hence changing from $\Lambda = 0.2\,\mathrm{GeV}$ to $\Lambda = 1.2\,\mathrm{GeV}$ has little effect.

The difference in the cross sections calculated in the different gauges is not significant in the structure function analysis as the only effect is at high transverse momenta and the large transverse momentum diffractive final-state events provide a small contribution to the total diffractive DIS data sample. The difference between gauge choices is visible when the unintegrated transverse momentum distribution spectrum of the models is studied and can be seen in the graphs in Chap. 5.

It can be seen from Fig. 4.1 that the inclusion of a large 3-jet diffractive final-state contribution at low β would improve the fit of the Donnachie-Landshoff model to the diffractive structure function data, but would be destructive to the Ellis-Ross form factor model fit. To discriminate between a dijet Ellis-Ross scenario and a dijet plus multi-jet Donnachie-Landshoff scenario further effort is required. This is addressed in the transverse momentum distribution analysis in Chap. 5.

4.3.2 Single-Gluon and Scalar-Pomeron Models

The single-gluon and scalar-pomeron model fits are shown in Fig. 4.2. The single-gluon model returns a χ^2/dof of approximately 1.5 for each choice of pomeron intercept. The curve from the single-gluon model falls below the data slightly at low β, but has a reasonable Q^2 and $x_{I\!P}$ behaviour. The scalar-pomeron model (dijet component) fits the diffractive structure function data well over the whole kinematic range of the data, giving a χ^2/dof of approximately 1 for a soft intercept and 1.5 for the harder intercept of $\alpha_{I\!P}(0) = 1.2$.

4.3.3 Two-Gluon Model

The fit of the two-gluon Landshoff-Nachtmann model (dijet component) to the diffractive structure function data is shown in Fig. 4.3. This model provides a poor fit to the large pseudo-rapidity gap cut data, with a χ^2/dof of 3.3 for all choices of pomeron intercept. The most significant feature of this fit is the failure of the model to describe the small-β dependence of the data. This fall-off was predicted by the investigation of the $p_\perp^2$ behaviour of the two-gluon structure function in Sect. 3.8.5. The reason for this is that for large $p_{\perp\,\mathrm{min}}^2$ the diffractive structure function has a β^3 dependence, leading to a rapid fall-off of the structure function at low β, in disagreement with the relatively flat dependence found experimentally.

One may ask whether this feature persists in all two-gluon exchange models, as the two-gluon model described in Sect. 3.6 assumes a particular form for the "non-perturbative" gluon propagators. In the case of the more phenomenological BEKW model [59–61] it is easy to check that the β^3 behaviour should also apply to the $q\bar{q}$ longitudinal and transverse components. The remaining term in the BEKW model, which might give a better β dependence for the case of a strong $p_\perp^2$ lower bound, is the $q\bar{q}g$ component. This dependence is not known at present, but it would be interesting to be able to include the contribution due to the large-$p_\perp^2$ structure of the three-jet component of two-gluon exchange in the above analysis.

The two-gluon model could fit the large pseudo-rapidity gap cut structure function data with the inclusion of a contribution from higher-multiplicity diffractive final-state events at low β. This is a reasonable possibility as fits by H1 [15] and by Bartels *et al* [59–61] suggest there is a large low-β contribution from quark–antiquark–gluon diffractive final states. In a large pseudo-rapidity gap analysis in which there are significant phase space restrictions

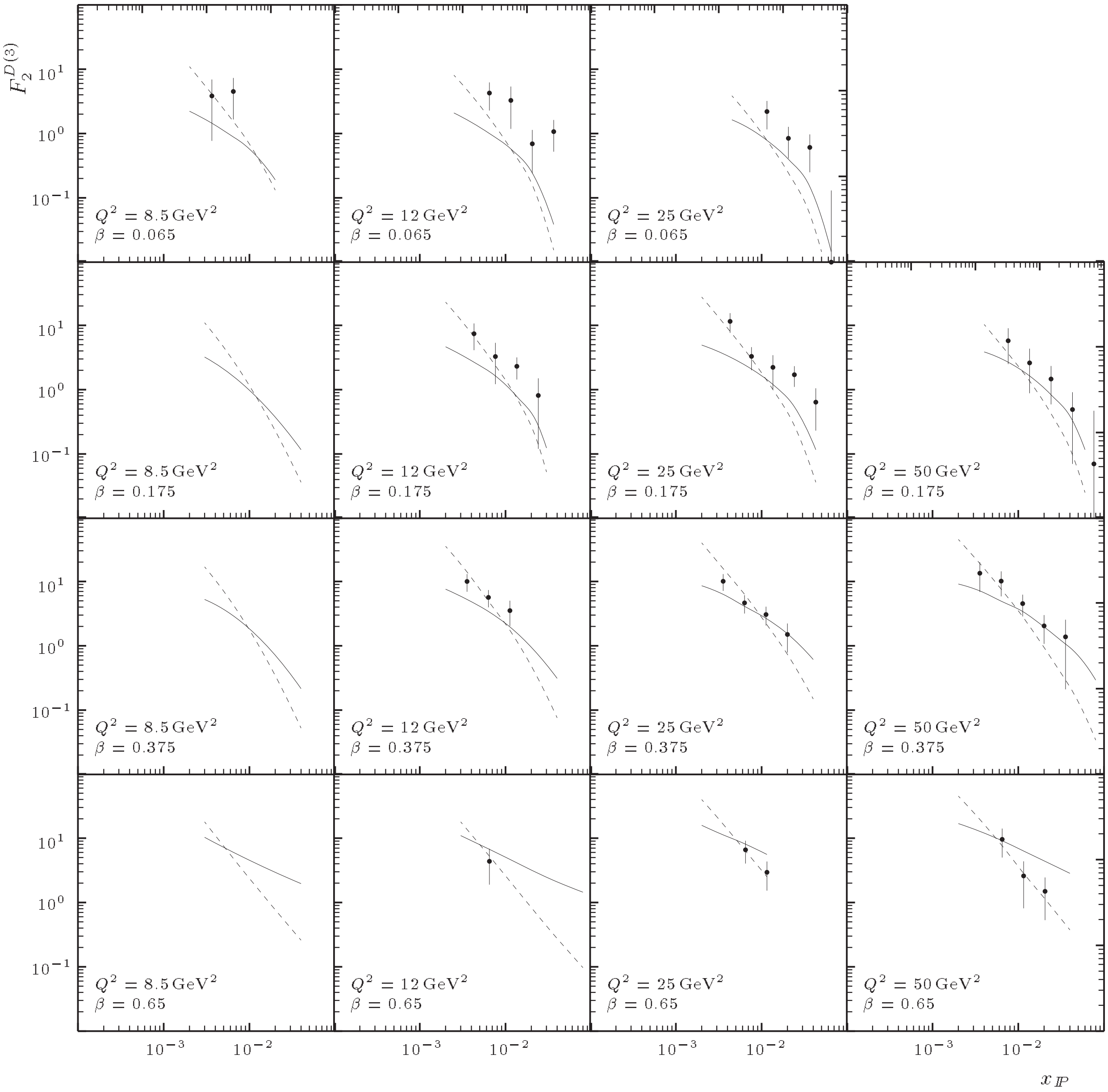

Figure 4.2: *The single-gluon exchange and scalar-pomeron models fitted to diffractive structure function data with parameters as in Fig. 4.1. The solid line is the prediction from the single-gluon exchange model and the dashed line is the scalar-pomeron model.*

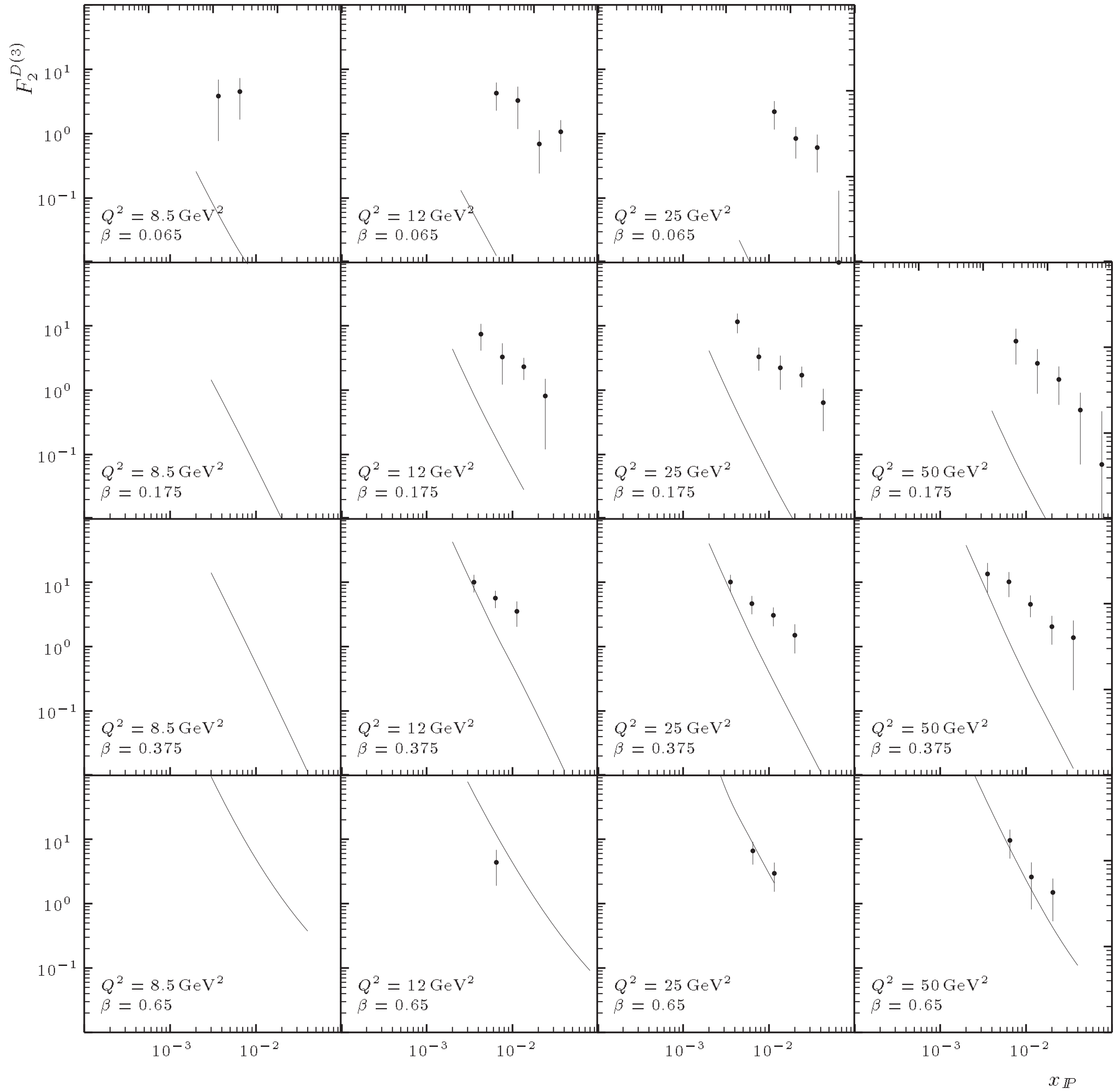

Figure 4.3: *The two-gluon exchange model fitted to diffractive structure function data with parameters as in Fig. 4.1.*

due to the data selection cuts this effect is expected to be particularly enhanced, as the pseudo-rapidity constraints are weaker for three-or-more parton final-state events.

4.3.4 Summary of Structure Function Fits

The results of all the fits are shown in Table 4.1, where the χ^2 for the various fits are given.

	χ^2 for 41 dof		
	$\alpha_{I\!P}(0) = 1.08$	$\alpha_{I\!P}(0) = 1.2$	$\alpha_{I\!P}(0) = 1$
E-R: $f(k^2) = \sqrt{\frac{\Lambda^2}{\Lambda^2 - k^2}}$	39 (37)	57 (54)	30 (30)
D-L: $f(k^2) = \frac{\Lambda^2}{\Lambda^2 - k^2}$	81 (102)	79 (97)	83 (179)
Single-Gluon:	64	57	69
Two-Gluon:	137	136	137
Scalar-Pomeron:	48	61	40
E-R (non-covariant gauge):	41 (41)	56 (55)	34 (34)
D-L (non-covariant gauge):	69 (86)	68 (82)	71 (90)

Table 4.1: *Summary of fits of the colour-singlet exchange models to pseudo-rapidity gap diffractive structure function data from [57]. The low-momentum cut-offs in the form factors are $\Lambda = 1.2\ GeV$ ($\Lambda = 0.2\ GeV$).*

The Ellis-Ross form factor model and the scalar-pomeron model provide a good fit to the large pseudo-rapidity gap structure function data over the entire kinematic range of the data. The Donnachie-Landshoff form factor model, however, fails to fit the low-β structure function data without the need for a significant 3-jet contribution from quark–antiquark–gluon diffractive final states. The two-gluon model has low-β behaviour which is similar to the Donnachie-Landshoff model, though the two-gluon model has a more pronounced fall-off at low β due to its sensitivity to the phase space constraints. Finally, the single-gluon exchange model provides a reasonable fit to the diffractive structure function data.

The different gauge choices for the form factor models did not give significantly different fits to the structure function data. This is because the main effect of the gauge choice is manifest in the large-$p_\perp^2$ tail of the differential cross section while the large-$p_\perp^2$ events constitute only a small amount of the diffractive DIS data. Also interesting is the difference in the $x_{I\!P}$ distributions between the two form factor models. This arises through the $x_{I\!P}$ dependence of $p^2_{\perp\,\mathrm{min}}$.

There are two possible interpretations of the structure function analysis results: The first is that diffractive DIS is dominated by the quark-driven process of Fig. 1.2 and the process may be described by the phenomenological Ellis-Ross form factor model, or possibly the scalar-pomeron or single-gluon models, and that the Donnachie-Landshoff and two-gluon models are ruled out by the data. The other possibility is that the diffractive structure function data requires a large contribution from high-multiplicity diffractive final-states. The Donnachie-Landshoff model or the two-gluon model could fit the data with an additional contribution from quark–antiquark–gluon diffractive processes. This latter possibility is supported by recent experimental [15] and theoretical [59–61] work. Further investigation is necessary in order to discriminate between these two possibilities. This is the object of Chap. 5.

4.4 Pomeron Structure Function Analysis

It was explained in Sect. 2.5.5 and observed in the fits in Sect. 4.3.1 that, as a result of the large pseudo-rapidity gap cuts, a further $x_{I\!P}$ dependence is expected from the lower limit of the phase space integral. This means that a pomeron structure function extracted from the diffractive structure function by multiplying by an appropriate power of $x_{I\!P}$ will not be independent of $x_{I\!P}$. One can, however, consider the diffractive structure function data at fixed $x_{I\!P}$ and see how it varies with Q^2 and β. This will remove the $x_{I\!P}$-factorization-breaking effects, but not the effects due to the sensitivity of the phase space boundaries $k^2_{\rm min}$ (equivalently, $p^2_{\perp\,{\rm min}}$) to Q^2 and β. Fixing $x_{I\!P}$, therefore, gives the phase-space restricted pomeron structure function, $F_2^{I\!P}$, which can be compared with the large pseudo-rapidity gap cut data.

The (restricted) pomeron structure function, $F_2^{I\!P}$, is shown for the 5 models in Figs. 4.4, 4.5 and 4.6 where the data for which $x_{I\!P} \approx 0.0065$ is plotted. The model curves are calculated at the corresponding $x_{I\!P}$ values and where there is no data in Q^2 and β with appropriate $x_{I\!P}$, the theory points are calculated using the value $x_{I\!P} = 0.00649$, which is the most common value of $x_{I\!P}$ of the plotted data points.

Fig. 4.4(a) shows the pomeron structure function, $F_2^{I\!P}$, up to the normalisation determined from the diffractive structure function fits in Sect. 4.3, as a function of Q^2 at fixed β and Fig. 4.4(b) shows the β dependence of $F_2^{I\!P}$ at fixed Q^2 for the Donnachie-Landshoff and Ellis-Ross form factor models. The Ellis-Ross model provides a good description of the pomeron structure function data. The failure of the Donnachie-Landshoff model to describe the small-β structure function data is highlighted in Fig. 4.4(b). Table 2.2 shows that, at fixed Q^2 and $x_{I\!P}$, $k^2_{\rm min}$ decreases approximately linearly with increasing β. Hence for the D-L model, in which the form factor introduces an approximately $1/k^4$ dependence into the cross section, a significant suppression is expected in the pomeron structure function at small β. This is evident in the dotted curve of Fig. 4.4(b). The Ellis-Ross form factor model has an approximately $1/k^2$ dependence introduced by the form factor, so such a strong suppression is not expected. Furthermore, this choice of form factor leads to a $\ln(Q^2/\mu^2)$ behaviour in the diffractive and pomeron structure functions, which is visible in Fig. 4.4(a). Fig. 4.4(b) shows that, even for data with a relatively large pseudo-rapidity cut, the Ellis-Ross model predicts a rather flat β distribution of $F_2^{I\!P}$, in better agreement with the experimental data.

Fig. 4.5 shows the pomeron structure function fit for the single-gluon exchange model (solid line) and for the dijet contribution to the scalar-pomeron model (dotted line). As with the diffractive structure function fits in Sect. 4.3.2, the scalar-pomeron model describes the pomeron structure function well and the single-gluon model also gives a reasonable fit.

The restricted pomeron structure function for the two-gluon model is shown in Fig. 4.6. This demonstrates where the model fails to describe the structure function data. The rapid fall-off in the structure function at small-β discussed in Sect. 3.8.5 can be seen in Fig. 4.6(b) and it is also obvious from Fig. 4.6(a) that the dijet component of two-gluon exchange does not describe the Q^2 structure of the large pseudo-rapidity gap structure function data.

The factorization-breaking effects from the additional $x_{I\!P}$-dependence introduced by pseudo-rapidity gap cuts mean that $F_2^{I\!P}$ can only be "extracted" by considering data at fixed $x_{I\!P}$. Most importantly, it is not possible to cleanly extract the pomeron intercept from the data, which is usually done by fitting a straight-line curve to a log-linear plot of $F_2^{D(3)}$ against $x_{I\!P}$. However, by taking into account the phase space effects, it is possible to extract the pomeron intercept from large pseudo-rapidity gap cut data by fitting the diffractive structure function with the pomeron intercept as a free parameter. This is a

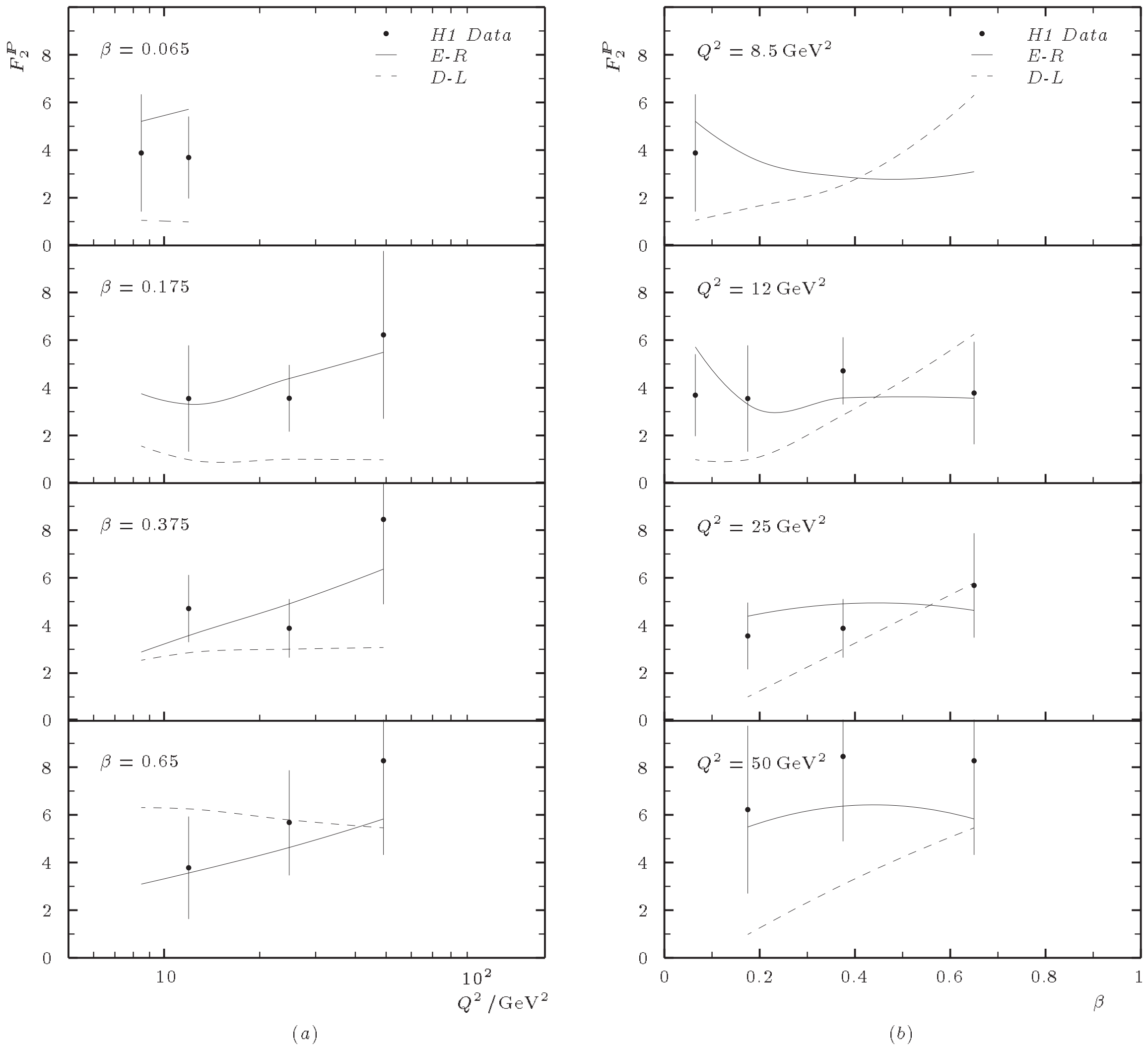

Figure 4.4: *The Ellis-Ross and Donnachie-Landshoff form factor models fitted to pomeron structure function data, with parameters as in Fig. 4.1. The solid line is the prediction from the Ellis-Ross model as determined in Fig. 4.1 and the dashed line is the Donnachie-Landshoff model.*

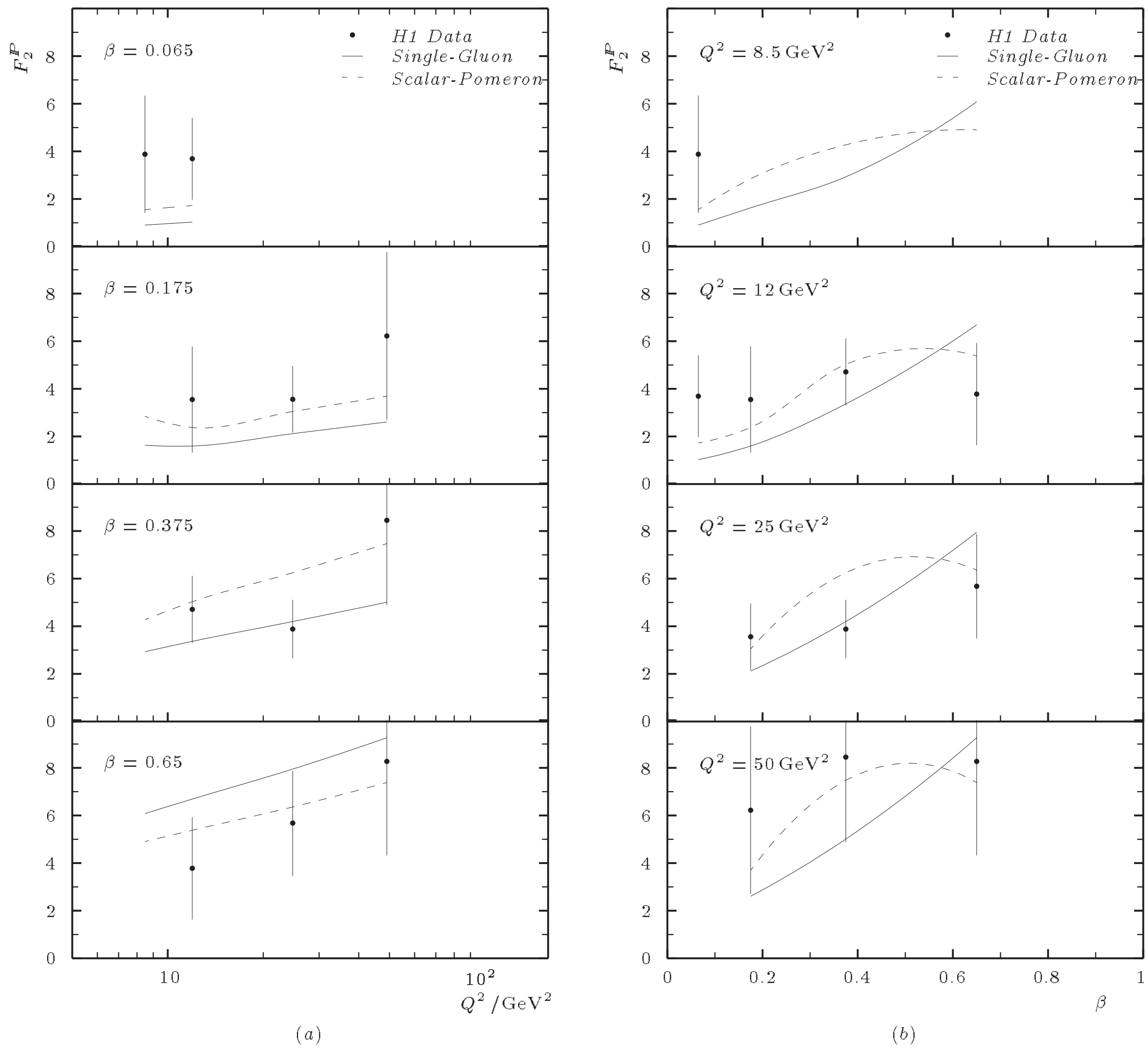

Figure 4.5: *The single-gluon exchange and scalar-pomeron models fitted to pomeron structure function data with parameters as in Fig. 4.1. The solid line is the prediction from the single-gluon exchange model and the dashed line is the scalar-pomeron model.*

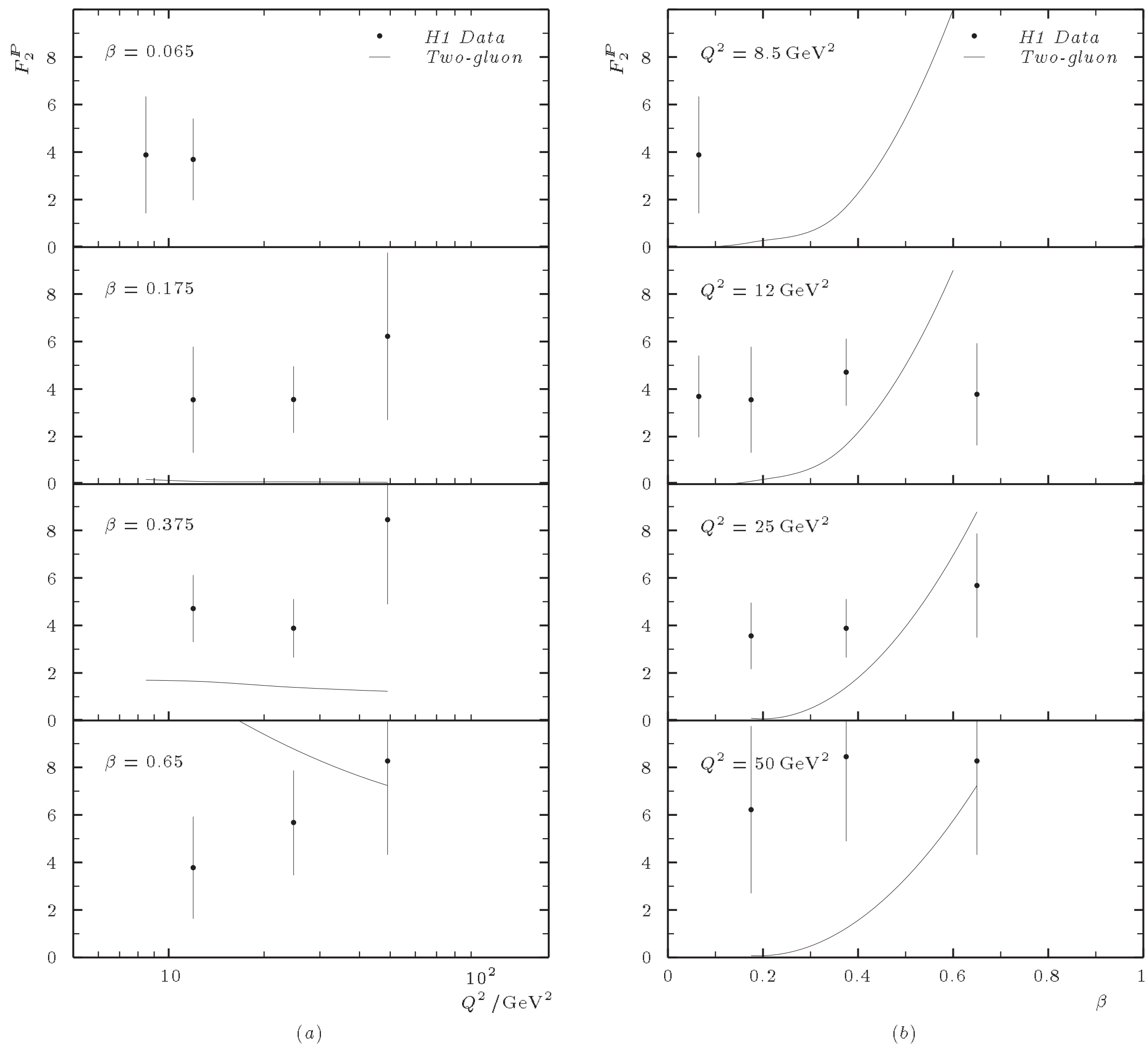

Figure 4.6: *The two-gluon model fitted to pomeron structure function data with parameters as in Fig. 4.1.*

difficult procedure as the phase space constraints are complicated functions of $x_{I\!P}$ and therefore, since the large pseudo-rapidity gap events form a subset of the full diffractive DIS sample, it is most sensible to use data without phase space effects to extract $\alpha_{I\!P}(0)$.

4.5 Future Pseudo-Rapidity Gap Structure Function Analyses

It was shown in [1, 2] and Sect. 2.5 that H1 and ZEUS analyses in which only events with large pseudo-rapidity gaps are selected are not described by resolved-coupling processes as previously formulated [29], because the cuts select only events in which the partons coupling to the pomeron to have large virtualities. For a given pseudo-rapidity gap cut, the boundaries of the region of parameter space in Q^2, β and $x_{I\!P}$ in which pseudo-rapidity gap cuts impose strong virtuality constraints can be calculated. The reduction in the available phase space can be calculated using the results in App. A. These experiments select data from a region of parameter space which is sensitive to the large transverse momentum structure of the diffractive final state. Furthermore, data taken with strong pseudo-rapidity gap cuts contains an enhanced multi-jet diffractive final-state component. These experiments therefore provide a strong test of models of the colourless component of the pomeron coupling to the virtual quark. Tests of both the $p_\perp^2$ structure of diffractive DIS models and of the relative contribution from multi-parton diffractive final states, can be made more stringent by relatively straightforward measurements.

Data taken using different pseudo-rapidity gap cuts in which the cuts restrict the kinematically-accessible phase space can be used in two ways: The first would verify the conclusion of the calculations in App. A that strong pseudo-rapidity gap cuts restrict the accessible $p_\perp^2$ of diffractive DIS events, since a relative reduction of the diffractive structure function would be observed in data taken with a stronger pseudo-rapidity gap cut. Second, the relative reduction of the diffractive structure function predicted by a given model of diffractive scattering can be tested against the data for a range of pseudo-rapidity gap cuts. This latter test provides a strong discriminator between the various models proposed to describe diffractive DIS, particularly as the models are sensitive to the exchanged-quark virtuality and the transverse momentum of the diffractive final state.

The dependence of exchanged-parton virtuality on pseudo-rapidity gap cuts and kinematic parameters would best be studied by examining two samples of data. The first should be chosen with a pseudo-rapidity cut to select data for which $|k^2| \gtrsim$ a few GeV^2. The second set should be chosen to differ from the first only in the strength of the pseudo-rapidity gap cut. The data from the sample corresponding to the stronger pseudo-rapidity gap is predicted to show a relative reduction in the extracted diffractive structure function due to there being less phase space available for the scattering interaction. This is a model-independent effect and does not require knowledge of the overall normalisation of the data.

The size of the reduction in the diffractive structure function between two data sets chosen with different, but strong, pseudo-rapidity gap cuts is a direct indication of the magnitude of the colourless component of the pomeron coupling to the virtual quark. The magnitude of this reduction is predicted by the various models of diffractive scattering and hence offers a sensitive way to discriminate between those models. This procedure also has the advantage that no knowledge is required of the overall normalisation of the data. Selecting two data sets with strong cuts also provides a further test of the large-$p_\perp^2$ and large-k^2 structure of the models.

At present, there is only one published study with data chosen with two different pseudo-rapidity gap cuts [15]. However, the virtuality constraints due to the data selection cuts are insufficient to reduce the available phase space measurably. Table 2.1 shows the minimum transverse momentum and exchanged-quark virtuality for data corresponding to two pseudo-rapidity cuts, $\eta_{\max} = 3.3$ and $\eta_{\max} = 2$, used in an H1 analysis [15] of large pseudo-rapidity gap diffractive DIS. The data is plotted in Fig. 4 of [15], the only points not plotted in the H1 figure being those corresponding to large $p^2_{\perp\,\mathrm{min}}$ and $\eta_{\mathrm{max}} = 2$. These are the points at which one would expect to see significant differences between the data taken with two different pseudo-rapidity gap cuts, but these points have been discarded by other cuts imposed on the $\eta_{\mathrm{max}} = 2$ data.

The graphs in Figs. 4.7 and 4.8 show the data used in the fits of the form factor models to large pseudo-rapidity gap cut diffractive structure function data from Sect. 4.3, with the solid lines representing the diffractive structure function fits of the Donnachie-Landshoff and Ellis-Ross models, respectively. The dashed lines show the fits that would be expected using the same normalisation, but with weaker ($\eta_{\mathrm{max}} = 1.3$, upper line) and stronger ($\eta_{\mathrm{max}} = 2.3$, lower line) pseudo-rapidity gap cuts. The differences between the structure function predictions with differing pseudo-rapidity gap cuts are significant. However data with smaller uncertainties than in the present study would be required to be able to detect the reduction in the diffractive structure function due to stronger pseudo-rapidity gap cuts.

It is also important to obtain a higher-statistics sample of diffractive DIS data for which there is a large pseudo-rapidity gap between the forward proton direction and the diffractive final state in order to study the structure of high-multiplicity diffractive final states. The phase space restrictions on high-multiplicity diffractive final state events are lower than those on dijet final states and data taken with a large pseudo-rapidity gap cut should therefore contain an enhanced 3-jet contribution, providing a useful testing ground for models of the 3-jet component of diffractive DIS. Further, varying the strength of the pseudo-rapidity gap cut and looking at the relative normalisation and the change in shape of the data will provide a measure of the relative contribution from dijet and 3-jet final states to diffractive DIS as function of the kinematic parameters, Q^2, β and $x_{I\!P}$.

4.6 Summary

Five dijet-production colour-singlet exchange models were compared with diffractive structure function data for which the pseudo-rapidity gap cuts and kinematic parameters Q^2, β and $x_{I\!P}$ lead to a significant restriction on the final-state phase space for diffractive scattering. This has provided a sensitive test of models of diffractive DIS, particularly in the case of the two-gluon exchange model in which the β dependence differs significantly between the cases of negligible $p^2_{\perp\,\mathrm{min}}$ and large $p^2_{\perp\,\mathrm{min}}$.

Analysis of the available data with strong pseudo-rapidity gap cuts shows that the diffractive DIS cross section is relatively insensitive to pseudo-rapidity, implying that the direct component of the pomeron coupling provides a significant contribution to diffractive DIS. The fit assuming a direct C-even vector-like coupling to quarks is sensitive to the form factor describing the dependence on the exchanged-quark virtuality. An excellent fit is obtained using the Ellis-Ross form factor model, but not with the Donnachie-Landshoff form factor model which, in particular, fails to describe the small-β behaviour of the diffractive structure function. A good fit is also obtained for the scalar-pomeron model. The single-gluon exchange model provides a marginally acceptable fit to the data and the two-gluon model (dijet component) fails to describe the data at small β.

The addition of a quark–antiquark–gluon diffractive final-state component to the Landshoff-Nachtmann two-gluon model and to the Donnachie-Landshoff form factor model might enable either model to describe the data and it is important to carry out further investigations in order to distinguish between a dijet Ellis-Ross, single-gluon or scalar-pomeron scenario and a dijet plus 3-jet two-gluon or Donnachie-Landshoff picture.

The strong pseudo-rapidity cut data is not useful to distinguish between the choices of hard, soft or unit pomeron intercept, due to the presence of factorization-breaking effects from the phase space constraints imposed by data selection cuts.

Finally, further investigations were suggested to help refine the analyses in this chapter and also to test the conclusions presented here.

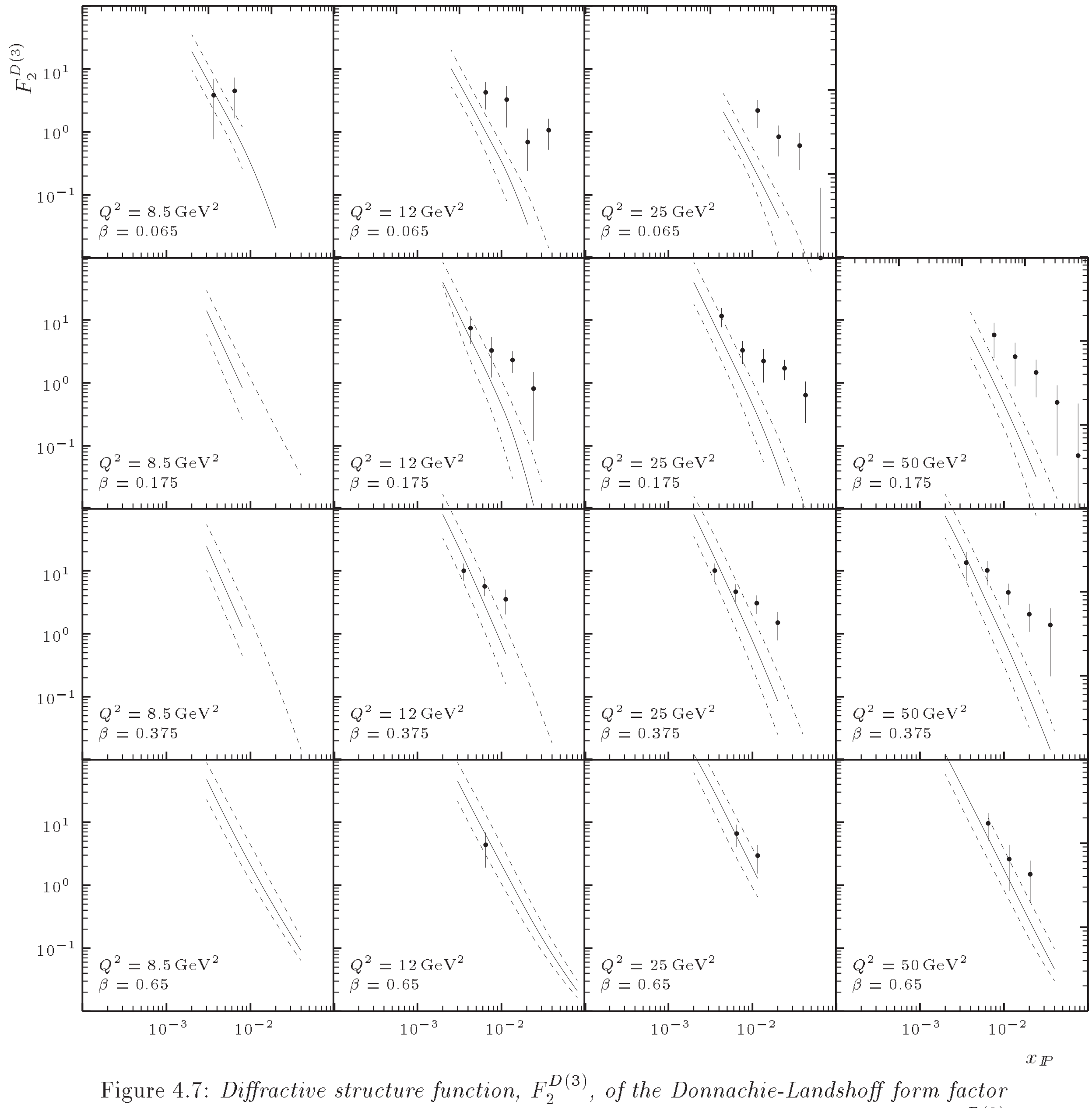

Figure 4.7: *Diffractive structure function, $F_2^{D(3)}$, of the Donnachie-Landshoff form factor model with various pseudo-rapidity gap cuts. The solid curve shows the plot of $F_2^{D(3)}$ from Fig. 4.1 with $\alpha_{I\!P}(0) = 1.08$ and $\Lambda = 0.2\,GeV$. The data plotted with solid points is described in Fig. 4.1. The data and the solid line correspond to a pseudo-rapidity gap cut at hadron level of $\eta_{\max} = 1.8$. The upper dashed line is the Donnachie-Landshoff model with the same normalisation as the solid line, but with a cut of $\eta_{\max} = 2.3$, while the lower dashed line corresponds to a cut of $\eta_{\max} = 1.3$.*

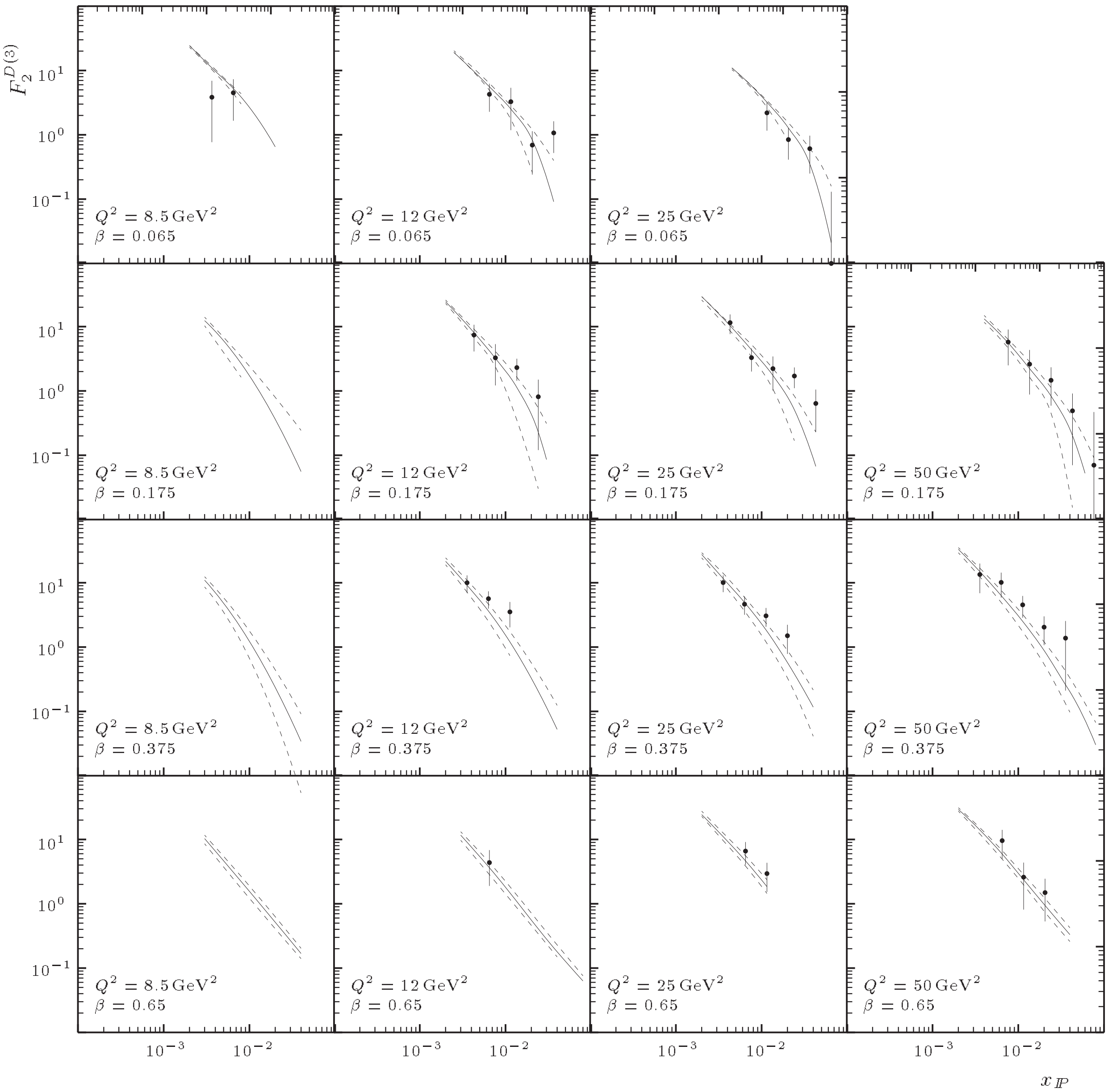

Figure 4.8: *Diffractive structure function, $F_2^{D(3)}$, of the Ellis-Ross form factor model with various pseudo-rapidity gap cuts. The solid curve shows the plot of $F_2^{D(3)}$ from Fig. 4.1 with $\alpha_{\mathbb{P}}(0) = 1.08$ and $\Lambda = 0.2\,GeV$. The data plotted with solid points is described in Fig. 4.1. The data and the solid line correspond to a pseudo-rapidity gap cut at hadron level of $\eta_{\max} = 1.8$. The upper dashed line is the Ellis-Ross model with the same normalisation as the solid line, but with a cut of $\eta_{\max} = 2.3$, while the lower dashed line corresponds to a cut of $\eta_{\max} = 1.3$.*

Chapter 5

Comparison With Data II: Thrust Transverse Momentum Distribution Analysis

5.1 Introduction

The transverse momentum distribution of the diffractive final state can be used to test models of diffractive DIS. An analysis of the thrust transverse momentum distribution and a comparison of colour-singlet exchange models using H1 transverse momentum distribution data is presented in this chapter.

The data selection cuts imposed to select diffractive DIS events constrain the kinematically-accessible phase space available for the interaction. As a result of the pseudo-rapidity gap cut there is no dijet contribution at low transverse momenta. An additional contribution is therefore required to describe the data at small transverse momenta. At the transverse momentum values at the low-momentum dijet cut-off, the data also changes slope, having an approximately quadratic fall-off with increasing transverse momentum up to 4-10 GeV^2 which changes to a quartic fall-off at larger transverse momenta. The (β-dependent) position of the low transverse momentum dijet cut-off corresponds closely to the transverse momentum values at which the slope of the cross section changes from a quadratic to a quartic fall-off.

The large transverse momentum part of the data can be fitted with the two-gluon Landshoff-Nachtmann model and with the Donnachie-Landshoff form factor model (calculated in the non-covariant gauge). The other dijet production models considered lead to a cross section with a quadratic fall-off with transverse momentum at large transverse momenta and hence fail to describe the data.

The main conclusion of this analysis is that a significant small-β 3-jet contribution is probably required to fit the data. It is demonstrated that the combination of a two-gluon dijet model and an exponential thrust transverse momentum distribution provides a good fit over the entire kinematic range of the large pseudo-rapidity gap diffractive DIS data.

5.2 Phase Space Analysis and Data Selection Cuts

H1 measured the differential cross section for diffractive DIS with respect to thrust transverse momentum, $p_\perp^2$, and final-state diffractive mass, M_X, and presented their results in the form [49]

$$\frac{1}{\sigma}\,\frac{\mathrm{d}^2\sigma}{\mathrm{d}M_X^2\,\mathrm{d}p_\perp^2}(p_\perp^2)\bigg|_{\text{fixed } M_X}\,. \tag{5.2.1}$$

The diffractive cross section was integrated over Q^2 and $x_{I\!P}$ in the range

$$\begin{aligned} Q^2 &: 10 \to 100\,\mathrm{GeV}^2\,, \\ x_{I\!P} &: 10^{-4} \to 3.2\times 10^{-2}\,, \end{aligned} \tag{5.2.2}$$

and the data was binned with average diffractive masses of

$$M_X = 7.01,\ 9.40,\ 12.82,\ 16.85,\ 21.20,\ 28.58\ \mathrm{GeV}\,. \tag{5.2.3}$$

This corresponds to integrating over small values of β, for example: for $M_X = 7.01\,\mathrm{GeV}$, over the range of Q^2 in this analysis, β ranges from 0.17 to 0.67; whereas for $M_X = 28.58\,\mathrm{GeV}$, β ranges from 0.01 to 0.11. Here "small" is interpreted as values of β for which one might expect 3-jet processes to provide a significant contribution to the diffractive final state (specifically, $\beta \lesssim 0.3$ [59–61]).

The H1 transverse momentum distribution data [49] is summarised in Table 5.1. This data has a $1/p_\perp^2$ fall-off at low transverse momenta, steepening to a $1/p_\perp^4$ fall-off at higher transverse momenta. The $1/p_\perp^4$ tail is present for all values of M_X a long way away from the phase space limit of $p^2_{\perp\,\mathrm{max}} = M_X^2/4$. For $M_X = 28.58\,\mathrm{GeV}$, for example, the data changes slope at about $p_\perp^2 = 10\,\mathrm{GeV}^2$.

$< p_\perp^2 >$ GeV^2	$\frac{1}{\sigma}\frac{\mathrm{d}\sigma}{\mathrm{d}p_\perp^2\,\mathrm{d}M_X^2}$ GeV^{-4}	δ_{stat}	δ_{syst}	$\sqrt{\delta^2_{\mathrm{stat}}+\delta^2_{\mathrm{syst}}}$
.41	.361	.032	.039	.050
1.83	.141	.018	.028	.033
4.26	.048	.008	.013	.015
8.42	.017	.003	.004	.005
17.38	.0049	.0010	.0011	.0015
32.09	.0014	.0004	.0006	.0007
58.28	.00054	.00018	.00025	.00031
113.20	.00011	.00006	.00011	.00013

Table 5.1: *H1 thrust transverse momentum distribution cross section data for* $\overline{M_X} = 28.58$ *GeV. (The uncertainties,* δ_{stat} *and* δ_{syst}*, correspond to the statistical and systematic errors, respectively, in* $\frac{1}{\sigma}\frac{\mathrm{d}\sigma}{\mathrm{d}p_\perp^2\,\mathrm{d}M_X^2}$*.)*

There are two cuts which restrict the accessible range of Q^2 and $x_{I\!P}$ for a given final-state thrust transverse momentum and diffractive mass:

1. *Cut on y:* $y < 0.5$.

This cut is imposed to restrict the photo-production background, as well as to remove events where the diffractive system is strongly boosted in the backward direction [49]. This leads to the restriction on $x_{I\!P}$,

$$x_{I\!P} > \frac{2(Q^2 + M_X^2)}{S_{\mathrm{Tot}}}\,, \tag{5.2.4}$$

which sets a lower limit on the integral over $x_{I\!P}$ as a function of Q^2 at fixed M_X.

2. *Pseudo-rapidity gap cut: require pseudo-rapidity gap greater than* $\eta_{\mathrm{max}} = 3.2$.

It was shown in Chap. 2 that imposing a pseudo-rapidity gap cut removes part of the low-$p_\perp$ dijet contribution to diffractive DIS. For a given range of the kinematic variables Q^2, M_X^2 and $x_{I\!P}$, a pseudo-rapidity gap cut corresponds to imposing a lower transverse momentum cut-off, $p^2_{\perp\,\mathrm{min}}$, on accepted events. Therefore, when calculating the cross section at a given $p_\perp^2$, say $p^2_{\perp\mathrm{fixed}}$, one should only integrate over the region of Q^2 and $x_{I\!P}$

for which $p^2_{\perp\,\mathrm{min}} < p^2_{\perp\,\mathrm{fixed}}$. The region of phase space for which $p^2_{\perp\,\mathrm{min}} > p^2_{\perp\,\mathrm{fixed}}$ will have been removed by the pseudo-rapidity gap cut.

The effect of the pseudo-rapidity gap cut on the final-state phase space is illustrated in Fig. 5.1. In this figure, the region of the $Q^2 - x_{I\!P}$ plane over which one would integrate to extract the cross section at $p^2_\perp = 4\,\mathrm{GeV}^2$ is shown for a diffractive mass of $M_X = 16\,\mathrm{GeV}$ and a pseudo-rapidity gap cut of $\eta_{\mathrm{max}} = 3.2$. The upper shaded area shows the region excluded by pseudo-rapidity gap cuts since dijet events with $p^2_\perp < 4\,\mathrm{GeV}^2$ are removed at these values of Q^2 and $x_{I\!P}$ by the cut. The lower shaded area shows the region excluded by the cut on y. As a result, only a restricted region of phase space is populated by dijet events with thrust transverse momentum of $4\,\mathrm{GeV}^2$.

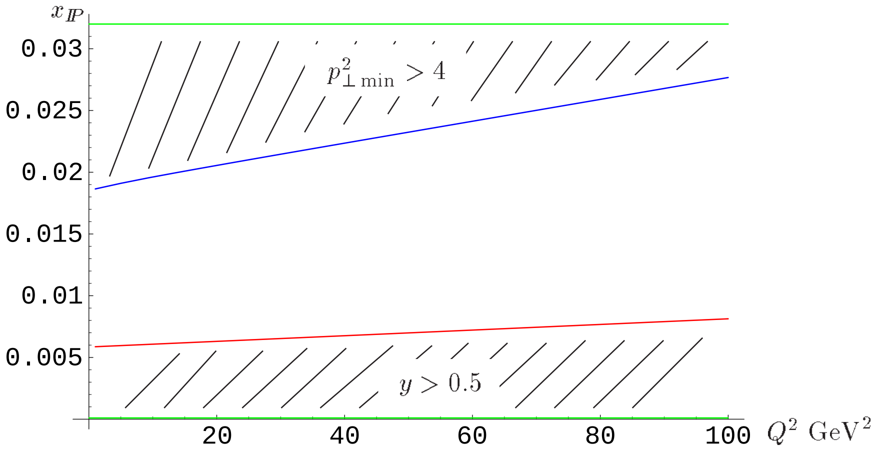

Figure 5.1: *Phase space plot for* $p^2_{\perp\,\mathrm{min}} = 4\,GeV^2$ *with* $\eta_{\mathrm{max}} = 3.2$ *(hadron-level cut) and* $M_X = 16\,GeV$. *The horizontal lines show upper and lower limits of* $x_{I\!P}$ *in the data sample, the upper slanted line shows the upper limit on* $x_{I\!P}$ *as a result of the pseudo-rapidity gap cut and the lower slanted line shows the lower limit of* $x_{I\!P}$ *as a result of the* y *cut.*

For large diffractive masses and small $p^2_\perp$ the data selection cuts exclude the entire $Q^2 - x_{I\!P}$ plane, leading to a sharp low-momentum cut-off in $p^2_\perp$ below which there are no values of the kinematic parameters Q^2 and $x_{I\!P}$ in the H1 data for which dijet events can contribute to the diffractive cross section. The position of the cut-off depends on M_X and moves to larger transverse momentum values for larger diffractive masses. In Fig. 5.2, the position of the low-momentum dijet cut-off is shown for three diffractive masses: $M_X = 28.58\,\mathrm{GeV}$, $21.20\,\mathrm{GeV}$ and $16.85\,\mathrm{GeV}$. For smaller diffractive masses the transverse momentum distribution of dijet events is not strongly restricted by the data selection cuts and for $M_X \lesssim 15\,\mathrm{GeV}$, there is no lower $p_\perp$ cut-off from the data selection cuts (i.e., $p^2_{\perp\,\mathrm{min}} \lesssim 1\,\mathrm{GeV}^2$).

This analysis of the effect of data selection cuts on the dijet contribution to diffractive DIS therefore demonstrates that an additional contribution is needed to describe the H1 thrust transverse momentum distribution data at low transverse momenta.

5.3 Transverse Momentum Distribution Fits with Dijet Models

The diffractive scattering cross section is calculated by integrating the cross section from the colour-singlet exchange models over the region of phase space in Q^2 and $x_{I\!P}$ accessed in the H1 analysis. The common feature of all the fits is that, as a result of the large pseudo-rapidity gap requirement and the cut on y, the dijet contribution is cut off sharply at low $p^2_\perp$. For example, for a diffractive mass of $M_X = 28.58\,\mathrm{GeV}$, the phase space restrictions affect the dijet contribution below about $10\,\mathrm{GeV}^2$, completely removing the

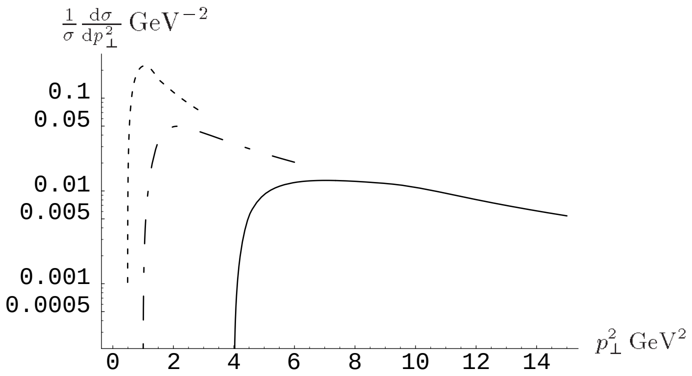

Figure 5.2: *Position of dijet transverse momentum cut-offs at different diffractive masses (two-gluon model). The solid line corresponds to a diffractive mass of 28.58 GeV, while the dot-dashed line is for M_X =21.20 GeV and the dotted line corresponds to a diffractive mass of 16.85 GeV.*

contribution from events with $p_\perp^2 \lesssim 4\,\text{GeV}^2$. For $M_X = 16.85\,\text{GeV}$, the turn-over is much sharper and the spectrum cuts off at $p_\perp^2 \approx 1 - 2\,\text{GeV}^2$.

Figs. 5.3 and 5.4 show the dijet model fits to the H1 data by fitting only the part of the curves after the phase space-induced turn-over. These show how the models describe the large-$p_\perp^2$ behaviour of the cross section.

The graphs shown in Figs. 5.3(a) and 5.4(a) are of the Donnachie-Landshoff form factor model in the non-covariant gauge (solid line) and in the Feynman gauge (dashed line). In both cases a pomeron intercept of 1.2 and low-momentum cut-off in the form factor of $\Lambda = 1.2\,\text{GeV}$ are assumed. The Donnachie-Landshoff model in the non-covariant gauge provides a good fit to the large-$p_\perp$ part of the transverse momentum spectrum, that is, it predicts a $1/p_\perp^4$ fall-off for $p_\perp^2 \gtrsim 10\,\text{GeV}^2$. The Feynman gauge curve gives a poor fit, mainly due to a large-$p_\perp$ tail which is not present in the data. The unphysical large-$p_\perp$ behaviour is not present in the non-covariant gauge cross section [36].

Figs. 5.3(b) and 5.4(b) show fits of the Ellis-Ross form factor model to the transverse momentum distribution data with $\alpha_{I\!P}(0) = 1.2$ and $\Lambda = 1.2\,\text{GeV}$. Again, a high-$p_\perp$ tail is evident in the cross section calculated in the Feynman gauge. The Ellis-Ross model fails to describe the large transverse momentum behaviour of the data in either gauge, predicting a $1/p_\perp^2$ fall-off at large transverse momenta. The scalar-pomeron and single-gluon exchange models are shown in Figs. 5.3(c) and 5.4(c). These models also fail to describe the $1/p_\perp^4$ behaviour of the data at large $p_\perp^2$, giving only a $1/p_\perp^2$ fall-off.

Figs. 5.3(d) and 5.4(d) show the fit of the two-gluon model to the transverse momentum distribution data. This model fits the data well above the phase space-induced low-$p_\perp$ cut-off. The fit here is similar to that obtained using the Donnachie-Landshoff form factor model.

5.4 Comparison of Structure Function and Thrust Transverse Momentum Distribution Analyses

5.4.1 Introduction

The results of fitting the colour-singlet exchange models to the thrust transverse momentum distribution data are surprising when compared with the results from the structure function analysis in Chap. 4. The structure function data is obtained from the $p_\perp$-integrated cross section, while the transverse momentum distribution analysis considers data which has not been integrated over $p_\perp^2$. The Ellis-Ross and single-gluon exchange models provide an acceptable fit to the large pseudo-rapidity gap structure function data,

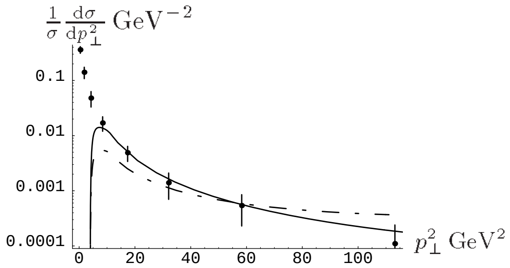

(a) *Donnachie-Landshoff form factor model in the non-covariant gauge (solid line) and in the Feynman gauge (dashed line). Here* $\Lambda = 0.2\,GeV$ *and* $\alpha_{I\!P}(0) = 1.08$.

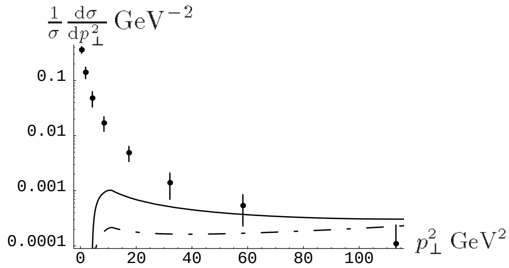

(b) *Ellis-Ross form factor model in the non-covariant gauge (solid line) and in the Feynman gauge (dashed line). Here* $\Lambda = 0.2\,GeV$ *and* $\alpha_{I\!P}(0) = 1.08$.

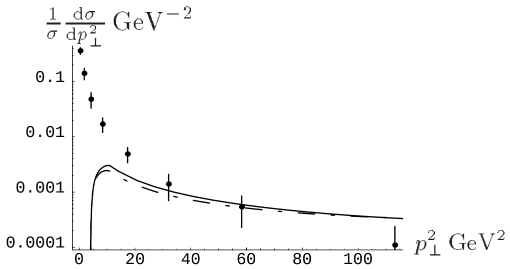

(c) *Single-gluon exchange model (solid line) and scalar-pomeron exchange model (dashed line).*

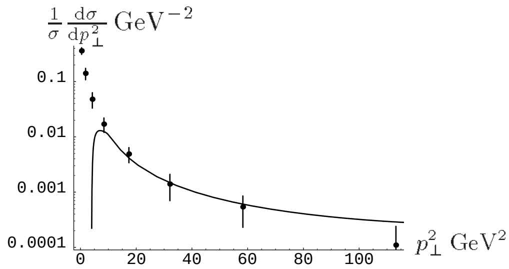

(d) *Two-gluon exchange model.*

Figure 5.3: *Fits of the colour-singlet exchange models to H1 transverse momentum distribution data [49]. The fit is made to points after the turn-over of the curves (see Sect. 5.3 for explanation). The curves correspond to the models, while the solid points represent H1 data. The plots show the fits for diffractive masses of* $M_X = 28.58\,GeV$. *The statistical and systematic errors have been added in quadrature.*

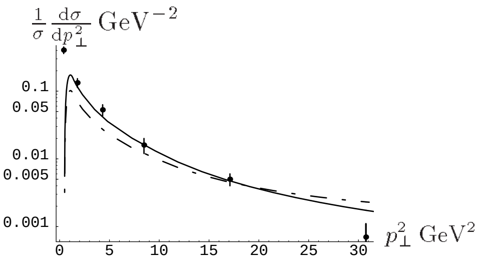

(a) *Donnachie-Landshoff form factor model in the non-covariant gauge (solid line) and in the Feynman gauge (dashed line). Here* $\Lambda = 0.2\,GeV$ *and* $\alpha_{I\!P}(0) = 1.08$.

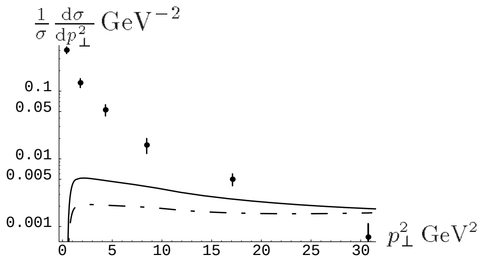

(b) *Ellis-Ross form factor model in the non-covariant gauge (solid line) and in the Feynman gauge (dashed line). Here* $\Lambda = 0.2\,GeV$ *and* $\alpha_{I\!P}(0) = 1.08$.

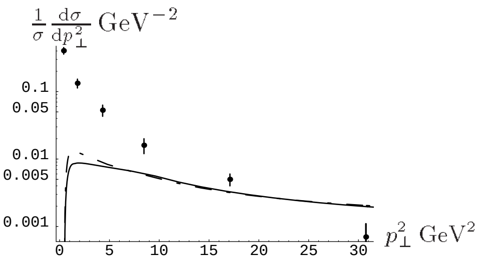

(c) *Single-gluon exchange model (solid line) and scalar-pomeron exchange model (dashed line).*

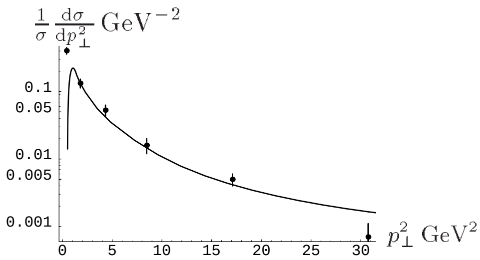

(d) *Two-gluon exchange model.*

Figure 5.4: *Fits of the colour-singlet exchange models to H1 transverse momentum distribution data [49]. The fit is made to points after the turn-over of the curves. The curves correspond to the models, while the solid points are H1 data. The plots show the fits for diffractive masses of* $M_X = 16.85\,GeV$.

but are unable to describe the shape of the thrust transverse momentum distribution data. By contrast, the Donnachie-Landshoff and two-gluon models fit the thrust transverse momentum distribution data well, but under-estimate the structure function data badly at low β.

There are two possible ways to reconcile the results of these analyses: The first possibility is that the Ellis-Ross and single-gluon exchange models may describe the data at large β (in the region where the operator product expansion is believed to be reliable in describing diffractive DIS), but that the leading-twist description fails at small β. Another possibility is that the Donnachie-Landshoff and two-gluon models are able to fit both sets of data with the addition of a substantial contribution from multi-jet diffractive final states. This latter possibility requires the multi-jet contribution to the transverse momentum data to be most significant at small-β and to have a thrust transverse momentum distribution which is strongly peaked near zero.

5.4.2 β-Dependent Structure Function Models

It is possible that the Ellis-Ross or leading-twist single-gluon exchange models describe a physical picture of the data for large β, but that some other (possibly higher-twist) component is required at low β. The Ellis-Ross model provides a good fit ($\chi^2/\mathrm{dof} = 37/41$) to the large pseudo-rapidity gap structure function data studied in Chap. 4 and describes that data well over a wide range of Q^2, β and $x_{I\!P}$. However, most of the large pseudo-rapidity gap structure function data and the transverse momentum distribution data is at low β and there is insufficient large-β data available to test this possibility.

The present thrust transverse momentum distribution analysis demonstrates a need for a substantial non-dijet contribution to the diffractive DIS cross section. Due to the low-$p_\perp$ dijet cut-off, an additional contribution is needed to explain the low transverse momentum data. The position of the cut-off also shows that the size of this extra contribution is β-dependent and is peaked at low β. If this low-β contribution is included in the Ellis-Ross model fits to large pseudo-rapidity gap structure function data, the combination will overshoot the structure function data at low β. The need for a substantial low-$p_\perp$, low-β contribution to explain the thrust transverse momentum distribution data therefore presents a problem for the Ellis-Ross and leading-twist models.

A further explanation for the apparent discrepancy between the success of the Ellis-Ross model in fitting the diffractive structure function data while failing to describe the thrust transverse momentum distribution data is the unphysical large-$p_\perp^2$ tail in the Ellis-Ross transverse momentum distribution. The E-R model falls off as $1/p_\perp^2$ at large transverse momenta unlike the experimentally-observed $1/p_\perp^4$ behaviour. Large-$p_\perp^2$ events are particularly significant at low β as the low-$p_\perp^2$ part of the spectrum is removed at low β by the pseudo-rapidity gap cuts. Integrating over the Ellis-Ross transverse momentum distribution, therefore, gives a large contribution to the low-β diffractive structure function from the large-$p_\perp^2$ tail. This additional contribution mimics the low-β contribution from 3-jet events which is expected to be present in the diffractive data sample, but which is not included in either of the form factor models.

5.4.3 Two-Gluon Dijet Contribution Plus 3-Jet Contribution

The M_X-dependent position of the dijet low transverse momentum cut-off is such that at large diffractive masses the region where dijet events cannot contribute to the diffractive scattering cross section is larger than for smaller diffractive masses. This dominance at small β is what is expected from quark–antiquark–gluon diffractive final states [58–61]. It therefore seems reasonable, given also the small values of β in the H1 thrust study, to conclude that the extra contribution required to explain the thrust transverse momentum distribution is probably provided by 3-jet diffractive final-state events. This conclusion is consistent with [59–61], where it is estimated that 3-jet events both provide a significant contribution to the diffractive structure function for $\beta \lesssim 0.4$ and dominate $F_2^{D(3)}$ for $\beta \lesssim 0.2$. This hypothesis is also consistent with the H1 findings that the average thrust of diffractive DIS events is less than 0.9 [49].

If the 3-jet contribution is indeed dominant at small β (large M_X), one would expect to see the pattern of diffractive structure function results found in [1] for the Donnachie-Landshoff and two-gluon models. In this case the dijet contribution is expected to underestimate the diffractive structure function at small β.

Considering the results shown in Figs. 5.3 and 5.4 and the analysis in [1], two comments can be made about the distribution of 3-jet processes in the diffractive sample:

- *3-jet events dominate the large pseudo-rapidity gap sample at low β*:

The requirement of a large pseudo-rapidity gap between the proton direction and the diffractive final state selects a data sample from which the low-$p_\perp^2$ dijet events have been removed [1, 4]. As a result, higher-multiplicity final states are required to explain the low transverse momentum part of the spectrum. Furthermore, comparing Figs. 5.3 and 5.4 shows that the cut-off in the dijet contribution from the phase space restrictions is shifted to smaller $p_\perp^2$ for smaller values of M_X. This is to be expected because smaller M_X corresponds to larger values of β, for which there is a weaker restriction on the dijet phase space [1, 4]. The ratio of multi-jet events to dijet events is also expected to be smaller at large β [59–61].

- *The thrust transverse momentum distribution of 3-jet events is strongly peaked about 0*:

This conclusion is partly based on the success of the two-gluon dijet model in fitting the $1/p_\perp^4$ behaviour of the cross section at large transverse momenta and also on the inability of all the dijet models to describe that low-$p_\perp^2$ part of the spectrum due to data selection cuts. If the 3-jet events were to describe the part of the transverse momentum distribution not described by dijet events, they should also have thrust transverse momentum strongly peaked about $p_\perp^2 = 0$, in order not to affect the spectrum at larger transverse momenta.

A strongly peaked *thrust* transverse momentum distribution might be expected from a two-gluon "partonic" model of the pomeron. In such a model, the leading-order process is one where the photon interacts with one of the gluons in the pomeron, producing a diffractive quark–antiquark pair. The third final-state particle is the other constituent gluon in the pomeron, the pomeron remnant, which would be travelling in approximately the same direction as the initial proton. Therefore, one would expect the thrust axis of the final state to be closely aligned with the virtual photon–proton axis, especially if there is a reasonably isotropic distribution of momentum between the two constituent gluons in the pomeron. This hypothesis does, however, require a β-dependent non-perturbative spreading of the transverse momentum distribution of the remnant gluon of up to $p_\perp^2 \approx 6\,\mathrm{GeV}^2$ in order to fit the H1 data. The intrinsic transverse momentum of the pomeron has been discussed recently in [71].

It is also possible that the peaked thrust transverse momentum distribution might be due to the non-zero momentum transfer at the proton vertex [14]. It is not possible to explore this latter possibility further at present as there is insufficient data describing the $t_{I\!P}$-dependence of diffractive DIS.

5.4.4 Parameterization of the Extra Thrust Contribution

The thrust transverse momentum distribution data was fit with a combination of the two-gluon model and a parameterization for the "3-jet" contribution to diffractive DIS in which the invariant amplitude of the thrust transverse momentum distribution is described by the Gaussian[1]:

[1] Note that since the definition of the transverse momentum variable in the transverse momentum distribution analysis is different to that used in the diffractive structure function study, the parameterization

$$f(Q^2,\beta) = \frac{1}{Q^2\beta} e^{-\frac{p_\perp^2}{\beta^2 p_{\perp\,\max}^2}} . \tag{5.4.1}$$

This function gives a β-dependent distribution which falls sharply with increasing $p_\perp^2$. Since the H1 data contains no information about the absolute normalisation, in these fits the overall normalisation of each contribution is a free parameter, giving two adjustable parameters when combining the two contributions. The most unsatisfactory feature of the "3-jet" interpretation of this extra contribution is the need for an exponential β-dependent cut-off in the thrust transverse momentum distribution.

The combination fit is shown in Fig. 5.5. This fit describes the transverse momentum distribution data well in the range of diffractive masses studied by H1, only underestimating the data slightly at $M_X = 16.85$ GeV. This confirms that the data may be described by the combination of a dijet model with a quadratic fall-off with transverse momentum and a "3-jet" parameterization with an exponentially decaying thrust transverse momentum distribution.

A more complete test of this hypothesis would be to study data for which the overall normalisation of the cross section at each diffractive mass is measured, as this would enable the relative contributions of 2- and 3-jet final states to the diffractive cross section to be measured.

5.5 Proposed Future Thrust Transverse Momentum Distribution Experiments

Further investigation is required to test the conclusions of this analysis. On the theory side, there is a need for a full 3-jet diffractive DIS calculation or at least, as far as testing this analysis is concerned, for a Monte Carlo treatment of the thrust transverse momentum distribution of 3-jet diffractive events, with phase space effects due to data selection cuts taken into account. Better statistics and finer binning in the thrust transverse momentum variable would enable the interface between diffractive dijet production and the low-$p_\perp^2$ contribution to be explored. In a similar vein, analysing data corresponding to larger values of β, where phase space effects due to pseudo-rapidity gap cuts are less significant and dijet events are expected to dominate over higher-multiplicity diffractive final states, one would expect to see the quartic $p_\perp$-dependence in the present H1 data extend to smaller values of $p_\perp^2$. On the other hand, restricting to smaller values of β would push the position of the change to a quartic fall-off to larger values of $p_\perp^2$.

A more interesting experiment would be to keep the same range of kinematic parameters in Q^2, β and $x_{I\!P}$, but impose a stronger pseudo-rapidity gap cut. This would also push the position of the low-momentum dijet cut-off to larger values of $p_\perp^2$. The only effect on the sharply-peaked low thrust-$p_\perp$ contribution would be a decrease in the overall normalisation. With fine enough binning in $p_\perp$ this should therefore lead to the production of a "dip" in the cross section in the $p_\perp^2$ region between where the exponential low-$p_\perp$ contribution cuts off and where the $1/p_\perp^4$ dijet contribution starts.

Information about the overall normalisation of the cross section would enable the relative contributions of dijet and 3-jet events to diffractive DIS to be measured.

5.6 Summary

The transverse momentum distribution of the dijet component of several diffractive DIS models has been compared with recent H1 data [49].

which fits the thrust transverse momentum distributions here cannot be directly applied to the structure function analysis.

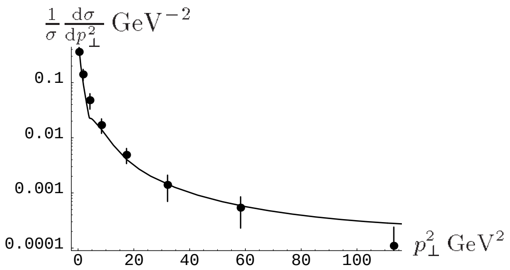

(a) *Dijet plus 3-jet fit for* $M_X = 28.58$ *GeV.*

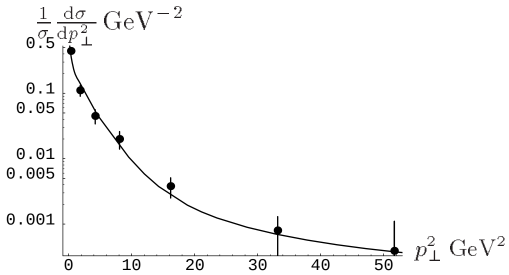

(b) *Dijet plus 3-jet fit for* $M_X = 21.20$ *GeV.*

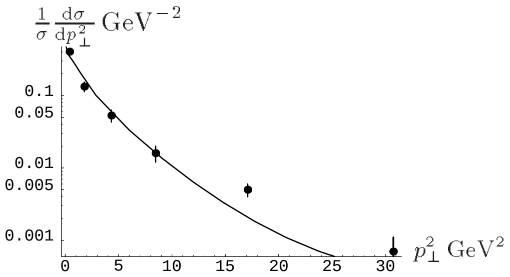

(c) *Dijet plus 3-jet fit for* $M_X = 16.85$ *GeV.*

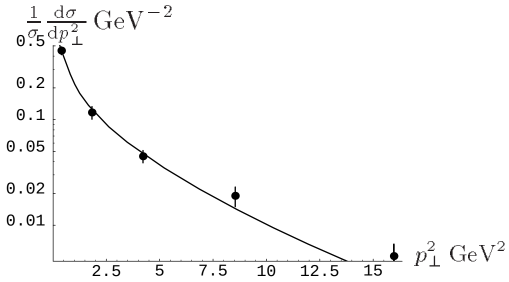

(d) *Dijet plus 3-jet fit for* $M_X = 12.82$ *GeV*

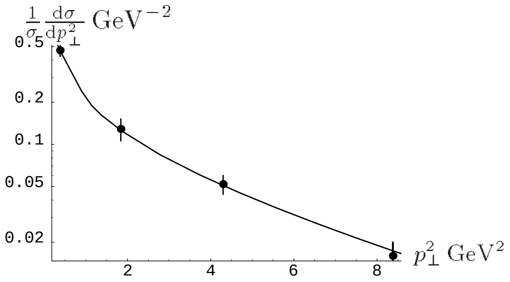

(e) *Dijet plus 3-jet fit for* $M_X = 9.40$ *GeV.*

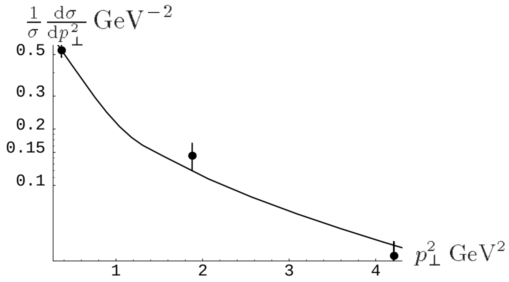

(f) *Dijet plus 3-jet fit for* $M_X = 7.01$ *GeV.*

Figure 5.5: *Comparison of the combined two-gluon dijet model plus 3-jet parameterization with H1 transverse momentum distribution data [49] at different diffractive masses.*

The general trend in the data is towards a $1/p_\perp^2$ fall-off at low transverse momenta, steepening to $1/p_\perp^4$ at about 4-10 GeV^2. The position of the change in slope depends on the diffractive mass, with the change in slope occurring at larger values of the transverse momentum variable for larger M_X.

The data selection cuts, particularly the pseudo-rapidity gap cuts imposed by H1 to select diffractive events, lead to a restriction on the available phase space for a large region of the parameter space covered by HERA. The main result is that, for most diffractive masses and for the range of Q^2 and $x_{I\!P}$ in this analysis, data selection cuts are expected to remove all dijet events with small transverse momenta. As a result, a further contribution, from quark–antiquark–gluon final states, for example, is required to explain the small-$p_\perp^2$ region of the H1 transverse momentum distribution data. The region in $p_\perp$ where the data changes slope corresponds closely to the region where phase space effects due to data selection cuts remove the low-$p_\perp$ dijet contribution.

Five colour-singlet exchange models were compared with the H1 data. The cross section from the form factor models was calculated in both the Feynman gauge and in a non-covariant gauge. The difference between the two gauge choices was particularly evident in the large-$p_\perp^2$ tail which one obtains using the Feynman gauge. This is not present in any other approach and it fails to describe the H1 thrust transverse momentum distribution data in this analysis. The Donnachie-Landshoff form factor model (in the non-covariant gauge) provided a good fit to the large transverse momentum part of the spectrum for all values of diffractive mass beyond the point where the slope changed to a $1/p_\perp^4$ fall. The Ellis-Ross form factor model, like the single-gluon and scalar-pomeron models, predicts a $1/p_\perp^2$ fall at large transverse momenta which is not consistent with the H1 data. The two-gluon model fits the large-$p_\perp$ part of the transverse momentum distribution well.

Since the region where dijet events cannot contribute to the diffractive cross section is larger for larger diffractive masses (i.e. smaller β), it was concluded that the extra contribution required to describe the H1 transverse momentum distribution data was probably from 3-jet diffractive final states. A combination of the two-gluon dijet model and a simple parameterization for the extra contribution using a β-dependent Gaussian gives a good fit to the entire thrust transverse momentum distribution. The 3-jet interpretation of this extra contribution is consistent with the structure function analysis of large pseudo-rapidity gap diffractive DIS in Chap. 4, in which a large 3-jet diffractive contribution is required at small β in addition to the dijet contribution from the Donnachie-Landshoff or two-gluon models. In addition, however, the present analysis requires the 3-jet diffractive events to have thrust transverse momentum strongly peaked about zero. This analysis also suggests that the apparent success of the Ellis-Ross, single-gluon and scalar-pomeron models in describing the diffractive structure function may be due to these models over-estimating the large-$p_\perp^2$ dijet contribution. An alternative possibility is that the Ellis-Ross or leading-twist single-gluon models may provide a reasonable fit to the diffractive DIS cross section at moderate to large values of β. Present pseudo-rapidity gap thrust transverse momentum distribution and structure function data in which the requirement of a large pseudo-rapidity gap restricts the available phase space corresponds mostly to small β and at present there is insufficient data, particularly at large β, to either prove or disprove these hypotheses.

This analysis demonstrates how the transverse momentum dependence of diffractive DIS can be used to distinguish between models. It is import to obtain an improved data set in the diffractive scattering regime, in particular at smaller $x_{I\!P}$, as the present jet production data has relatively large $x_{I\!P}$ where the purely diffractive interpretation may be invalid.

Chapter 6

Summary and Conclusions

6.1 Phase Space Constraints

It has been shown that imposing large pseudo-rapidity gap cuts to extract diffractive deep-inelastic scattering events from the fully-inclusive DIS data sample at HERA may lead to a systematic reduction in the measured diffractive structure function. This is because, for a wide range of HERA parameter space, the pseudo-rapidity gap cuts restrict the available phase space for the diffractive final state. Since this reduction is stronger at small β and at large $x_{I\!P}$, there will be comparatively less events selected by this method at small β and at large $x_{I\!P}$ than are present in the full diffractive data sample. Since the diffractive structure function is obtained by integrating the scattering cross section over the available phase space, a deficit of events at low β and large $x_{I\!P}$ will skew the structure function extracted from pseudo-rapidity gap events away from that which would be extracted from data selected from the full kinematic phase space.

The usual leading-order picture of diffractive DIS is that of Fig. 1.2 where the photon dissociates into a quark–antiquark pair which interacts with the proton by the exchange of a colourless state, the pomeron. Higher-order contributions to diffractive scattering include final states which also contain a gluon, such as those processes shown in Fig. 1.3. The Ingelman-Schlein interpretation assumes the pomeron to behave somewhat like a real hadronic particle, coupling only to on-shell partons which are interpreted as being constituents of the pomeron. In this interpretation, one can factorize the diffractive structure function into the product of an $x_{I\!P}$-dependent pomeron flux factor and an $x_{I\!P}$-independent pomeron structure function.

The phase space constraints due to pseudo-rapidity gap cuts can be expressed as a minimum virtuality imposed on the exchanged parton coupling to the pomeron and it has been shown in Sect. 2.5 and App. A that for some regions of HERA parameter space, this minimum virtuality can be of the order of several GeV^2. In some regions of parameter space in which there are strong virtuality constraints, the diffractive scattering cross section is significant (see, for example, Table 2.2). This indicates that there is a significant contribution to diffractive DIS from events where the exchanged colour-singlet system couples directly to the diffractive system with off-shell couplings. It is difficult to reconcile this result with an hadronic picture of the pomeron.

As well as imposing exchanged-parton virtuality constraints, pseudo-rapidity gap cuts remove diffractive events for which the diffractive system has low transverse momentum relative to the forward photon direction. This means, in particular, that diffractive data taken from a restricted phase space can be used to explore the large-$p_\perp^2$ structure of diffractive DIS. Low-$p_\perp^2$ events dominate the full diffractive DIS sample.

Furthermore, it was shown in [1] and Sect. A.4 that pseudo-rapidity gap cuts are more restrictive on the phase space available for dijet diffractive final states than on higher-multiplicity final states. This means that large pseudo-rapidity gap cuts can be used to select data with a strongly enhanced 3-jet component, providing a testing ground for models of the quark–antiquark–gluon diffractive final state.

6.2 Models of Diffractive DIS

Diffractive DIS data was used to test five models of colour-singlet exchange in diffractive DIS. In the data chosen large pseudo-rapidity gap cuts restrict the virtuality of the exchanged parton coupling to the pomeron in diagrams like Fig. 1.2 to be greater than a few GeV^2 and also restrict the transverse momentum of the diffractive final state to be large. Only the dijet component of the models was considered in these analyses, largely because there is no prescription for coupling the pomeron to gluons in two of the models. However, the rôle of higher-multiplicity diffractive final states was considered throughout.

The first models considered were the phenomenological form factor model of Donnachie and Landshoff and the variation suggested by Ellis and Ross. In these models a form factor is introduced as an effective pomeron–quark coupling. This serves to reduce the contribution from highly-virtual quarks coupling to the pomeron. The Donnachie-Landshoff and Ellis-Ross models differ most strongly in the virtuality and transverse momentum dependences introduced by the form factors, making them particularly well-suited to a large pseudo-rapidity gap analysis. The form factor models are not gauge-invariant and two choices of gauge were used in the calculations; the first is the Feynman gauge, while the other is a non-covariant gauge choice in which the Donnachie-Landshoff model behaves like the two-gluon Landshoff-Nachtmann model. The QCD-inspired models considered were the single-gluon exchange model in which the dynamics of the colour-singlet exchange are assumed to be driven by the exchange of a single hard gluon, with subsequent soft gluon exchanges which serve to dress the colour of the hard gluon, and a model in which the diffractive process is described by the exchange of the colour-singlet part of two non-interacting gluons. A model in which the pomeron interacts with partons with point-like scalar couplings was also studied.

The Ellis-Ross form factor model was also discussed in terms of a resolved-coupling interpretation of the pomeron. In this interpretation, the diagram of Fig. 3.1 provides a significant contribution to the diffractive structure function. This diagram is insensitive to struck-quark virtuality and is not rejected by pseudo-rapidity gap cuts. Furthermore, Fig.3.1 provides additional scaling violations to the diffractive structure function. The inclusion of this diagram into the H1 analysis [15], which previously included only the diagrams of Figs. 1.2 and 1.3, could provide a more isotropic interpretation of the parton momentum distribution within the pomeron. Proton–(anti)proton elastic and diffractive scattering data and diffractive DIS data may provide a means of separately investigating the quark and gluon structure of the pomeron, as the hadron–hadron experiments are sensitive to the quark structure of the pomeron, while the resolved-coupling interpretation of the Ellis-Ross model suggests that diffractive DIS may be driven by the gluonic content of the pomeron.

The colour-singlet exchange models were compared with diffractive structure function data for which the large pseudo-rapidity gap cuts impose strong constraints on the minimum exchanged-quark virtuality. The Ellis-Ross form factor model and the scalar-pomeron model (dijet component) fit the data well over the entire Q^2, β and $x_{I\!P}$ range, with a χ^2/dof of approximately 1 for 41 degrees of freedom. The single-gluon model ($\chi^2/\mathrm{dof} \approx 1.5$) gave a reasonable fit to the structure function data. The Donnachie-Landshoff form factor model and the two-gluon model (dijet component) failed to describe the data at low β.

The results of this analysis suggest two possible scenarios which might describe the colour-singlet exchange in diffractive DIS. In the first, the exchange is described by either the Ellis-Ross model with a quark–antiquark diffractive final state, requiring no additional gluon contribution to describe the data over the entire kinematic range. The other possibility is that the Donnachie-Landshoff model or the two-gluon model may describe the large pseudo-rapidity gap data with the inclusion of a large quark–antiquark–gluon diffractive final state component. In analogy with the proton structure function, which is driven by the gluon contribution at low x_{Bj}, the proposed 3-jet contribution to the pomeron structure function is significant at low β.

It was shown in Sect. 2.5.5 that it is not possible to extract an $x_{\mathbb{P}}$-independent pomeron structure function from large pseudo-rapidity gap cut diffractive DIS data. This is because, even though the diffractive structure function may be factorizable into an $x_{\mathbb{P}}$-dependent pomeron flux factor and an $x_{\mathbb{P}}$-independent pomeron structure function, the pseudo-rapidity gap data selection cuts introduce a further $x_{\mathbb{P}}$ dependence through the phase space lower limit, $p^2_{\perp\,\mathrm{min}}$. This also means that it is not easy to extract a pomeron intercept from large pseudo-rapidity gap diffractive DIS data. Three different choices of pomeron intercept were used in the fits and it was found that the data was not sufficiently precise to favour any particular intercept. Due to the complications introduced by factorization-breaking phase space effects, it is better to use diffractive DIS data taken from the unconstrained phase space to extract the pomeron intercept and use this value as an input parameter for the large pseudo-rapidity gap diffractive structure function fits.

The thrust transverse momentum distribution analysis provided an effective test of the conclusions of the diffractive structure function study. It also highlighted the difference in the two gauge choices in the form factor model calculations. In this study, the dijet component of the colour-singlet exchange models was compared with the unintegrated diffractive cross section, where data for which the pseudo-rapidity gap cuts constrain the available final-state phase space was used. The effect of the cuts was to remove a large part of the dijet contribution in which the diffractive system has small transverse momentum with respect to the virtual photon–proton axis. In particular, at large diffractive masses, dijet final states could not contribute at all to the low-$p^2_\perp$ part of the spectrum. The data did not reflect this sharp cut-off, exhibiting instead a smooth transition from a $1/p^2_\perp$ fall-off with increasing $p^2_\perp$ to a $1/p^4_\perp$ fall in the region where the dijet contribution was not rejected. The quadratic dependence was present for all values of the diffractive final-state mass, but this $1/p^2_\perp$ dependence occured only at low $p^2_\perp$. It was also shown that the full transverse momentum spectrum could be modelled by an exponential function with quadratic small-$p^2_\perp$ behaviour.

The $1/p^4_\perp$ behaviour of the thrust transverse momentum distribution occured for $p^2_\perp$ a long way from the phase space upper limit of $p^2_\perp = M^2_X/4$. The Donnachie-Landshoff (non-covariant gauge) and two-gluon models both fit the large-$p^2_\perp$ tail well, but the other three models gave a $1/p^2_\perp$ behaviour at large $p^2_\perp$ and were unable to describe the transverse momentum distribution. The part of the low-$p^2_\perp$ spectrum that is not present in the dijet cross section is largest at large diffractive masses, that is, at low β. This is the region in which quark–antiquark–gluon diffractive final-state events are expected to provide a significant contribution to the cross section. It was concluded that the low-$p^2_\perp$ part of the diffractive cross section is probably due to 3-jet diffractive final-state events. This additional contribution is just what is required by the Donnachie-Landshoff and two-gluon models to describe the large pseudo-rapidity gap cut diffractive structure function data. The inclusion of a low-β 3-jet contribution with thrust transverse momentum strongly peaked about zero would provide a good fit to both the diffractive structure function data and to the thrust transverse momentum distribution data. The 3-jet contribution was parameterized with a simple Gaussian function and the combination of the 3-jet parameterization and the two-gluon dijet model were shown to be able to fit all the thrust transverse momentum distribution data in Chap. 5.

The Ellis-Ross, single-gluon and scalar-pomeron models have the wrong large-$p^2_\perp$ dependence to describe the thrust transverse momentum distribution data. The Ellis-Ross and Donnachie-Landshoff models calculated in the Feynman gauge exhibited unphysical large-$p^2_\perp$ tails which are also unable to fit the data. Furthermore, if the additional low-β 3-jet contribution which is required to describe the low-$p^2_\perp$ thrust transverse momentum distribution data were included in the Ellis-Ross, single-gluon or scalar-pomeron models, this low-β contribution would destroy the fit of these models to the diffractive structure function data in Chap. 4.

The unsatisfactory feature of the thrust transverse momentum distribution fits is that the 3-jet contribution is required to be strongly peaked about $p_\perp^2 = 0$. One possible explanation is that this peaked distribution is due to non-perturbative spreading of the transverse momentum of the remnant gluon in a two-gluon pomeron, or due to the non-zero momentum transfer, $t_{I\!P}$, at the proton vertex. Further data and calculations are required to explain the origin of the low-$p_\perp^2$ 3-jet thrust transverse momentum distribution.

6.3 Future Experiments and Calculations

Large pseudo-rapidity gap cut diffractive DIS experiments were proposed to provide further tests of the results presented in this thesis. There is a need for large pseudo-rapidity gap data with better statistics, particularly data for which the cuts lead to considerable phase space constraints. It is possible to calculate the region in Q^2, β and $x_{I\!P}$ in which phase space constraints are expected. It would also be useful to have data taken with varying pseudo-rapidity gap cuts, in order to study both the pseudo-rapidity gap cut dependence of the data and also to study the transverse momentum and exchanged-quark virtuality structure of models of diffractive DIS.

Theoretical efforts to understand diffractive DIS better should focus on a full calculation of the 3-jet cross section. In terms of the analyses presented in this thesis, it would be most useful to have an analytic calculation of the 3-jet contribution to each of the models studied in a form in which phase space effects can be taken into account.

The cross section and structure function calculations in this thesis were carried out in the massless quark approximation. It would be interesting to calculate the contribution from diffractive charm production in the H1 and ZEUS experiments. This would require the phase space constraint calculations to be repeated for massive quarks, as well as requiring a recalculation of the cross sections, but would be a worthwhile exercise.

It would also be interesting to consider scenarios for including 3-jet diffractive final-state processes in the form factor models and to include the 3-jet contribution to the scalar-pomeron in the large pseudo-rapidity gap analysis. Finally, an alternative to fixing a gauge for the form factor models would be to consider the addition of contact terms to describe the coupling of the pomeron to the diffractive final state. Compared to the four two-gluon exchange diagrams, the introduction of contact terms would be equivalent to introducing an effective vertex to include the two diagrams in which the two gluons couple to different quark lines.

6.4 Conclusion

The two-gluon model, with a large contribution at low β from quark–antiquark–gluon diffractive final states, is the scenario most likely to describe diffractive DIS. This interpretation allows the colour-singlet state to couple to off-shell partons, as required by the constraints imposed by pseudo-rapidity gap data selection cuts and can be understood within the framework of QCD. The only difficulties in this interpretation are understanding why the thrust transverse momentum distribution of the 3-jet diffractive final state is strongly peaked about zero and how the two gluons might propagate in a colour-singlet state in order to produce the observed pseudo-rapidity gap. The physical picture is likely to be one in which the two gluons do interact with each other, closer to the BFKL model of the pomeron.

Appendix A

Constraints from Pseudo-Rapidity Cuts

A.1 Introduction

Pseudo-rapidity gap cuts select events for which there is no significant hadronic activity in a minimum angle $\theta_{\rm lab}^{\rm min}$ about the forward proton direction, where $\theta_{\rm lab}$ is the laboratory scattering angle shown in Fig. A.1(a). This can be seen by starting with a (parton-level) pseudo-rapidity cut made in the HERA laboratory frame, then boosting to the virtual photon–pomeron CMS, which relates $\theta_{\rm lab}$ to the CMS scattering angle $\theta_{\rm cms}$ (defined in Fig. A.1(b)). Since $\theta_{\rm cms}$ is one of the final-state phase space angles, the pseudo-rapidity gap cut leads to a restriction on the available phase space. This result was first discussed by Ellis and Ross in [2] and the calculation (with some corrections to the original) appears in [1]. A more detailed account of the phase space constraint calculation is in Sect. A.2. In Sect. A.3 there is a discussion of azimuthal angle effects due to pseudo-rapidity gap cuts. This is followed by calculations of phase space limits for multi-jet production in Sect. A.4.

A.2 Dijet Phase Space Constraints

Starting in the HERA LAB frame the dijet production process (with particle momenta shown in brackets)

$$e(p_e) + P(P) \to e(p_e') + P(P') + q(p_A) + \bar{q}(p_B)\,, \tag{A.2.1}$$

is parameterized by

$$\begin{aligned}
p_e &= (E_e,\, 0,\, 0,\, -E_e) & E_e &= 27.5\,\mathrm{GeV}\\
P &= (E_P,\, 0,\, 0,\, E_P) & E_P &= 820\,\mathrm{GeV}\\
p_e' &= (E_e',\, E_e'\sin\theta_{\rm lab}',\, 0,\, E_e'\cos\theta_{\rm lab}')\\
q &= (E_e - E_e',\, -E_e'\sin\theta_{\rm lab}',\, 0,\, -E_e - E_e'\cos\theta_{\rm lab}')\\
p_B &= (l,\, l\sin\theta_{\rm lab}\cos\phi_{\rm lab},\, l\sin\theta_{\rm lab}\sin\phi_{\rm lab},\, l\cos\theta_{\rm lab})\,,
\end{aligned} \tag{A.2.2}$$

where M_X^2 is the invariant mass squared of the diffractive system $X(X_{\rm lab}) = p_A + p_B$ and q is the four-momentum of the virtual photon in the underlying $\gamma^* - I\!P$ sub-reaction. The momentum transfer, $t_{I\!P}$, at the proton vertex is neglected and the pomeron is assumed to be emitted in the forward proton direction. The pomeron carries a fraction $x_{I\!P}$ of the proton longitudinal momentum.

The angles involved are shown in Figs. A.1(a) and A.1(b)[1].

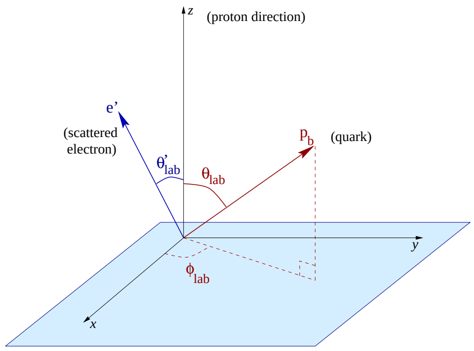

(a) *Definition of angles in the HERA laboratory frame.*

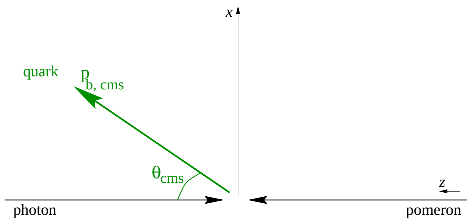

(b) *Definition of angles in the $\gamma^* - I\!P$ CMS.*

Figure A.1: *Angle definitions used in virtuality constraint calculations.*

The following relations are useful:

$$\begin{aligned}
Q^2 &= -q^2 = -(p_e - p_e')^2 \approx 2p_e \cdot p_e' = 2E_e E_e'(1 + \cos\theta'_{\text{lab}}) \\
W^2 &= (P+q)^2 \Rightarrow W^2 + Q^2 \approx 2P \cdot q = 2E_P[2E_e - E_e'(1 - \cos\theta_{\text{lab}})] \,,
\end{aligned} \tag{A.2.3}$$

giving

$$\begin{aligned}
E_e'(1 + \cos\theta'_{\text{lab}}) &= \frac{Q^2}{2E_e} \,, \\
E_e'(1 - \cos\theta'_{\text{lab}}) &= 2E_e - \frac{Q^2 + W^2}{2E_P} = 2E_e - \frac{Q^2}{2E_P \beta x_{I\!P}} \,.
\end{aligned} \tag{A.2.4}$$

Adding and subtracting Eqs. A.2.4 gives

$$\begin{aligned}
2E_e' &= 2E_e + \frac{Q^2}{2E_e} - \frac{Q^2}{2E_P \beta x_{I\!P}} \,, \\
2E_e' \cos\theta'_{\text{lab}} &= -2E_e + \frac{Q^2}{2E_e} + \frac{Q^2}{2E_P \beta x_{I\!P}} \,,
\end{aligned} \tag{A.2.5}$$

leading to

$$\begin{aligned}
2(E_e - E_e') &= -Q^2 \left[\frac{1}{2E_e} - \frac{1}{2E_P \beta x_{I\!P}} \right] \,, \\
2(E_e + E_e' \cos\theta'_{\text{lab}}) &= Q^2 \left[\frac{1}{2E_e} + \frac{1}{2E_P \beta x_{I\!P}} \right] \,.
\end{aligned} \tag{A.2.6}$$

Therefore

[1] This figure is a copy of Fig. 2.6 in Sect. 2.5.2.

$$\begin{aligned} E_e'^2(1-\cos^2\theta'_{\text{lab}}) &= E_e'^2\sin^2\theta'_{\text{lab}} = E_e'^2(1+\cos\theta'_{\text{lab}})(1-\cos\theta'_{\text{lab}}) \\ &= \frac{Q^2}{2E_e}(2E_e - \frac{Q^2}{2E_P\beta x_{I\!P}}) \\ &= Q^2[1-\frac{Q^2}{S_{\text{Tot}}\beta x_{I\!P}}]\,. \end{aligned} \tag{A.2.7}$$

The momentum of the diffractive system is therefore

$$\begin{aligned} X_{\text{lab}} &= q + x_{I\!P}P \\ &= (x_{I\!P}E_P + E_e - E_e',\, -E_e'\sin\theta'_{\text{lab}},\, 0,\, x_{I\!P}E_P - E_e - E_e'\cos\theta'_{\text{lab}}), \\ &= \Bigg(x_{I\!P}E_P + \frac{Q^2}{2}\left[\frac{1}{2E_P\beta x_{I\!P}} - \frac{1}{2E_e}\right], -\left[Q^2\left(1-\frac{Q^2}{2E_PE_e\beta x_{I\!P}}\right)\right]^{\frac{1}{2}}, \\ &\qquad 0, x_{I\!P}E_P - \frac{Q^2}{2}\left[\frac{1}{2E_P\beta x_{I\!P}} + \frac{1}{2E_e}\right]\Bigg)\,. \end{aligned} \tag{A.2.8}$$

In the CMS,

$$X_{\text{cms}} = (M_X,\, 0,\, 0,\, 0)\,. \tag{A.2.9}$$

A.2.1 Boosts from HERA LAB Frame to $\gamma^* - I\!P$ CMS

For a general linear boost along the z-direction

$$(E,\, 0,\, 0,\, z) \to \frac{1}{\sqrt{1-\beta^2}}(E-\beta z,\, 0,\, 0,\, z-\beta E)\,, \tag{A.2.10}$$

where β here is the boost parameter for the Lorentz transformation. The transformation from the LAB frame to the CMS is calculated with two orthogonal boosts. The first boost, along the z-axis, has boost parameter β_1 which satisfies $X^z_{\text{lab}} - \beta_1 X^0_{\text{lab}} = 0$, and is therefore given by

$$\beta_1 = \frac{X^z_{\text{lab}}}{X^0_{\text{lab}}} = \frac{-\left[\frac{Q^2}{2}\left(\frac{1}{2E_P\beta x_{I\!P}} + \frac{1}{2E_e}\right) - x_{I\!P}E_P\right]}{\frac{Q^2}{2}\left(\frac{1}{2E_P\beta x_{I\!P}} - \frac{1}{2E_e}\right) + x_{I\!P}E_P}\,. \tag{A.2.11}$$

After the first boost:

$$\begin{aligned} & X^0_{\text{lab}} \to X'^{\,0} \\ &= \frac{1}{\sqrt{1-\beta_1^2}}(X^0_{\text{lab}} - \beta_1 X^z_{\text{lab}}) \\ &= \frac{1}{\sqrt{1-\beta_1^2}}\Bigg[x_{I\!P}E_P + \frac{Q^2}{2}\left(\frac{1}{2E_P\beta x_{I\!P}} - \frac{1}{2E_e}\right) - \\ &\quad \beta_1\left\{x_{I\!P}E_P - \frac{Q^2}{2}\left(\frac{1}{2E_P\beta x_{I\!P}} + \frac{1}{2E_e}\right)\right\}\Bigg] \\ &= \frac{1}{\sqrt{1-\beta_1^2}}\Bigg[\beta_1^{-1}\left\{-\left(\frac{Q^2}{2}\left(\frac{1}{2E_P\beta x_{I\!P}} + \frac{1}{2E_e}\right) - x_{I\!P}E_e\right)\right\} - \end{aligned}$$

$$
\begin{aligned}
&\beta_1 \left\{ x_{I\!P} E_P - \frac{Q^2}{2} \left(\frac{1}{2E_P \beta x_{I\!P}} + \frac{1}{2E_e} \right) \right\} \Bigg] \\
&= \frac{1}{\sqrt{1-\beta_1^2}} \frac{1}{\beta_1} (1-\beta_1^2) \left[x_{I\!P} E_P - \frac{Q^2}{2} \left(\frac{1}{2E_P \beta x_{I\!P}} + \frac{1}{2E_e} \right) \right] \\
&\Rightarrow X'^{\,0} = \frac{\sqrt{1-\beta_1^2}}{\beta_1} \left[x_{I\!P} E_P - \frac{Q^2}{2} \left(\frac{1}{2E_P \beta x_{I\!P}} + \frac{1}{2E_e} \right) \right] , \\
&X'^{\,x} = X^x_{\mathrm{lab}} , \\
&X'^{\,y} = 0 , \\
&X'^{\,z} = 0 .
\end{aligned}
\tag{A.2.12}
$$

The boost along the x-direction involves boost parameter, β_2, (which satisfies $X'^{\,x} - \beta_2 X'^{\,0} = 0$) is given by

$$
\begin{aligned}
\beta_2 &= \frac{X^x_{\mathrm{lab}}}{X'^{\,0}} \\
&= - \frac{\beta_1}{\sqrt{1-\beta_1^2}} \frac{\left[Q^2 \left(1 - \frac{Q^2}{S_{\mathrm{Tot}} \beta x_{I\!P}} \right) \right]^{\frac{1}{2}}}{x_{I\!P} E_P - \frac{Q^2}{2} \left(\frac{1}{2E_P \beta x_{I\!P}} + \frac{1}{2E_e} \right)} \\
&= \frac{\beta_1}{\sqrt{1-\beta_1^2}} \frac{\left[Q^2 \left(1 - \frac{Q^2}{S_{\mathrm{Tot}} \beta x_{I\!P}} \right) \right]^{\frac{1}{2}}}{\frac{Q^2}{2} \left(\frac{1}{2E_P \beta x_{I\!P}} + \frac{1}{2E_e} \right) - x_{I\!P} E_P} .
\end{aligned}
\tag{A.2.13}
$$

These two boosts transform from the LAB frame to the $\gamma^* - I\!P$ CMS.

The effect of these boosts on the 0^{th} component of p_B is

$$
\begin{aligned}
\beta_1 : \quad & {p_B}^0 \to p'^{\,0}_B = \frac{l}{\sqrt{1-\beta_1^2}} (1 - \beta_1 \cos\theta_{\mathrm{lab}}) , \\
\beta_2 : \quad & p'^{\,0}_B \to p^0_{B\,\mathrm{cms}} = \frac{l}{\sqrt{1-\beta_2^2}} \left[\frac{(1-\beta_1 \cos\theta_{\mathrm{lab}})}{\sqrt{1-\beta_1^2}} - \beta_2 \sin\theta_{\mathrm{lab}} \cos\phi_{\mathrm{lab}} \right] .
\end{aligned}
\tag{A.2.14}
$$

The effect of the boosts on the 0^{th} component of the proton initial momentum is

$$
\begin{aligned}
\beta_1 : \quad & P^0 \to P'^{\,0} = \frac{(1-\beta_1)}{\sqrt{1-\beta_1^2}} E_P = \sqrt{\frac{1-\beta_1}{1+\beta_1}} E_P , \\
\beta_2 : \quad & P'^{\,0} \to P^0_{\mathrm{cms}} = \sqrt{\frac{1-\beta_1}{1+\beta_1}} \frac{E_P}{\sqrt{1-\beta_2^2}} .
\end{aligned}
\tag{A.2.15}
$$

Since the proton and final-state quarks are on-shell,

$$
\begin{aligned}
P \cdot p_B &= P^0 \, {p_B}^0 \, (1 - \cos\theta_{\mathrm{lab}}) \\
&= P^0_{\mathrm{cms}} \, p^0_{B\,\mathrm{cms}} \, (1 - \cos\theta_{\mathrm{cms}}) .
\end{aligned}
\tag{A.2.16}
$$

The LAB and CMS scattering angles are therefore related by

$$
\begin{aligned}
1-\cos\theta_{\rm lab} &= \frac{P^0_{\rm cms}p^0_{B\,{\rm cms}}(1-\cos\theta_{\rm cms})}{P^0 {p_B}^0} \\
&= \sqrt{\frac{1-\beta_1}{1+\beta_1}}\left(\frac{1-\beta_1\cos\theta_{\rm lab}}{\sqrt{1-\beta_1^2}} - \beta_2\sin\theta_{\rm lab}\cos\phi_{\rm lab}\right)\frac{(1-\cos\theta_{\rm cms})}{(\sqrt{1-\beta_2^2})^2} \\
&= \left(1-\beta_1\cos\theta_{\rm lab} - \sqrt{1-\beta_1^2}\,\beta_2\sin\theta_{\rm lab}\cos\phi_{\rm lab}\right)\frac{(1-\cos\theta_{\rm cms})}{(1+\beta_1)(1-\beta_2^2)}\,,
\end{aligned}
\tag{A.2.17}
$$

so that

$$
(1-\cos\theta_{\rm cms}) = \frac{(1+\beta_1)(1-\beta_2^2)\,(1-\cos\theta_{\rm lab})}{1-\beta_1\cos\theta_{\rm lab}-\sqrt{1-\beta_1^2}\,\beta_2\sin\theta_{\rm lab}\cos\phi_{\rm lab}}\,. \tag{A.2.18}
$$

Since $\theta_{\rm lab}$ is related to pseudo-rapidity (parton level), a pseudo-rapidity gap cut, $\eta_{\rm max}$, is equivalent to a cut on the lab angle $\theta^{\rm min}_{\rm lab}$, of

$$
\cos\theta^{\rm min}_{\rm lab} = \frac{1-e^{-2\eta_{\rm max}}}{1+e^{-2\eta_{\rm max}}}\,. \tag{A.2.19}
$$

The pseudo-rapidity gap cut, $\eta_{\rm max}$, therefore corresponds to a minimum CMS scattering angle of selected diffractive dijet events of

$$
(1-\cos\theta^{\rm min}_{\rm cms}) = \frac{(1+\beta_1)(1-\beta_2^2)\frac{2e^{-2\eta_{\rm max}}}{1+e^{-2\eta_{\rm max}}}}{1-\beta_1\frac{1-e^{-2\eta_{\rm max}}}{1+e^{-2\eta_{\rm max}}}-\sqrt{1-\beta_1^2}\beta_2\frac{2e^{-\eta_{\rm max}}}{1+e^{-2\eta_{\rm max}}}\cos\phi_{\rm lab}}\,. \tag{A.2.20}
$$

This corresponds to a minimum exchanged-quark virtuality and a minimum transverse momentum of the final-state quarks with respect to the forward proton direction of

$$
\begin{aligned}
-k^2_{\rm min} &= \frac{Q^2}{2\beta}\,(1-\cos\theta^{\rm min}_{\rm cms})\,, \\
p^2_{\perp\,{\rm min}} &= \frac{M_X^2}{4}\sin^2\theta^{\rm min}_{\rm cms}\,.
\end{aligned}
\tag{A.2.21}
$$

The original pseudo-rapidity constraint calculation contained an invalid small-angle approximation and an algebraic error. Correction of these errors lead to weaker virtuality constraints than those found in [2]. The original values for $-k^2_{\rm min}$ are shown with the corrected values in Table A.1.

A.3 Effect of Azimuthal Angle Distribution on Phase Space Constraints

The phase space constraints derived in Sect. A.2 for diffractive dijet production depend on the electron and proton initial energies, the CMS energy, Q^2, β and $x_{I\!P}$ and the azimuthal distribution of the final-state quarks. The azimuthal angle is defined in the HERA LAB frame to be the angle between the virtual photon–pomeron plane and the final-state quarks. Choosing the $x-z$ plane to be the plane of interaction of the virtual photon and pomeron, the diffractive system is produced with 3-momentum in the $x-z$ plane and the azimuthal angle, $\phi_{\rm lab}$, is defined in Fig. A.1(a) and Eq. A.2.2. In the calculations of the phase space limits, $p^2_{\perp\,{\rm min}}$ and $k^2_{\rm min}$, on transverse momentum and exchanged-quark virtuality, respectively, $\phi_{\rm lab}$ is chosen to minimise $|k^2_{\rm min}|$ and $p^2_{\perp\,{\rm min}}$. This amounts to

Q^2 GeV^2	β	$x_{I\!P}$	$-k^2_{\mathrm{min}}\,\mathrm{GeV}^2$ ($\eta_{\mathrm{max}} = 1.5$)	$-k^2_{\mathrm{min}}\,\mathrm{GeV}^2$ ($\eta_{\mathrm{max}} = 2.5$)	$-k^2_{\mathrm{min\,old}}\,\mathrm{GeV}^2$ ($\eta_{\mathrm{max}} = 1.5$)	$-k^2_{\mathrm{min\,old}}\,\mathrm{GeV}^2$ ($\eta_{\mathrm{max}} = 2.5$)
10	0.175	.0032	2.5	0.39	3.1	0.4
		.0050	5.1	0.89	7.5	1.0
	0.375	.0020	0.7	0.11	0.9	0.12
		.0032	1.5	0.27	2.3	0.3
	0.65	.0013	0.2	0.03	0.2	0.03
		.0020	0.3	0.06	0.5	0.07
28	0.175	.0050	6.2	0.95	7.5	1.0
		.0079	13.3	2.26	18.7	2.5
	0.375	.0020	0.8	0.12	0.9	0.1
		.0079	7.4	1.51	14.2	1.9
	0.65	.0020	0.4	0.06	0.5	0.07
		.0050	1.7	0.33	3.2	0.4
63	0.375	.0050	4.5	0.71	5.7	0.8
		.0079	9.4	1.66	14.2	1.9
	0.65	.0032	1.0	0.16	1.3	0.2
		.0079	4.1	0.83	8.0	1.1

Table A.1: *Constraints on struck-quark virtuality for diffractive dijet production as a result of the pseudo-rapidity gap cuts used in early ZEUS experiments [11]. In this table, $k^2_{\mathrm{min\ old}}$ corresponds to the results published in [2] and k^2_{min} are the revised virtuality constraints with corrections due principally to the elimination of the small-angle approximation used in [2].*

setting ϕ_{lab} to zero in the phase space constraint calculations. In this section, the effect of this approximation is studied by looking at $p^2_{\perp\,\mathrm{min}}$ at fixed Q^2, β and $x_{I\!P}$, to see the azimuthal angle dependence of the phase space constraints.

Fig. A.2 shows the effect of the two boosts described in Sect. A.2. Here it is assumed that the diffractive system X has 3-momentum in the positive xz-quadrant, thereby requiring boosts in the positive z and x directions to reach the rest frame of X. The edges of the cones represent a massless particle created with polar angle $\theta^{\mathrm{lab}}_{\mathrm{min}}$ with respect to the forward proton direction and azimuthal angle ϕ_{lab} from the direction of X. The magnitude of the 3-momentum of the massless particle is represented by the length of the cone and its polar angle is represented by the opening angle of the cone. Pseudo-rapidity gap cuts reject events with laboratory polar angle with respect to the electron–proton direction of less than $\theta^{\mathrm{lab}}_{\mathrm{min}}$. This cone therefore represents the angles below which diffractive scattering events are rejected by pseudo-rapidity gap cuts. The cone angle, $\theta^{\mathrm{min}}_{\mathrm{lab}}$, is independent of ϕ_{lab}. The first boost is in the positive z direction. This boost increases the opening angle of the cone deforming the acceptance cone from the configuration shown in Fig. A.2(a) to that shown in Fig. A.2(b). The opening angle of the cone is still independent of ϕ_{lab}. The second boost is in the positive x-direction. This boost takes the diffractive system to its rest frame and further deforms the acceptance cone to the configuration shown in Fig. A.2(c). This boost introduces an azimuthal angle dependence into the pseudo-rapidity gap cut phase space constraints because $\theta^{\mathrm{cms}}_{\mathrm{min}}$, the minimum acceptance angle in the virtual photon–pomeron CMS (the rest frame of X), depends on the azimuthal orientation of the edge of the acceptance cone. Fig. A.2 shows that, in the case that the 3-momentum of X is in the positive xz-quadrant, the minimum constraint on the CMS scattering angle θ^{cms} occurs at an azimuthal angle of $\phi_{\mathrm{lab}} = 0$.

The result of these boosts is that, as $p^2_{\perp\,\mathrm{min}}$ and k^2_{min} depend on ϕ_{lab}, the analyses in Chaps. 4 and 5 underestimate the strength of the phase space constraints as they take the conservative estimate of the minimum $p^2_{\perp}$ and k^2 to be those for a particle created with $\phi_{\mathrm{lab}} = 0$. Fig. A.3 shows the $p^2_{\perp\,\mathrm{min}}$ distribution as a function of azimuthal angle for $Q^2 = 30\,\mathrm{GeV}^2$, $\eta^{\mathrm{expt}}_{\mathrm{max}} = 1.8$, $\eta^{\mathrm{expt}}_{\mathrm{max}} = 2.5$ and various β and $x_{I\!P}$. This figures show that the azimuthal dependence is strongest in the region of HERA parameter space in which the phase space constraints due to pseudo-rapidity gap cuts are the greatest, particularly for large $x_{I\!P}$. For regions in which $p^2_{\perp\,\mathrm{min}}$ is small at $\phi_{\mathrm{lab}} = 0$, $p^2_{\perp\,\mathrm{min}}$ varies little with varying ϕ_{lab}.

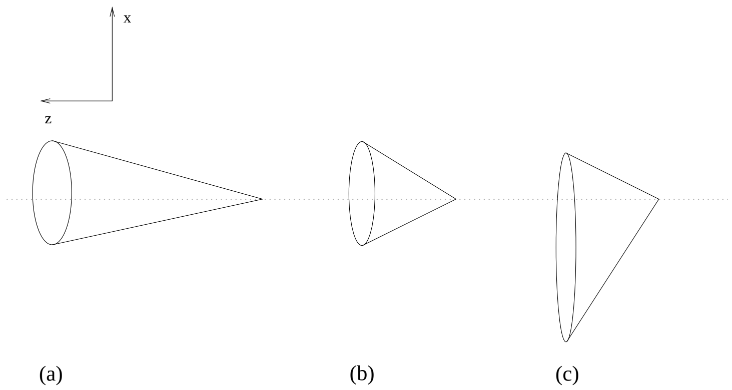

Figure A.2: *Effect of boosts on azimuthal angle dependence of pseudo-rapidity gap phase space constraints: (a) Initial configuration of pseudo-rapidity gap cut exclusion cone, (b) Exclusion cone following a boost in the positive z-direction, (c) Exclusion cone following a boost in the positive z-direction then a boost in the positive x-direction.*

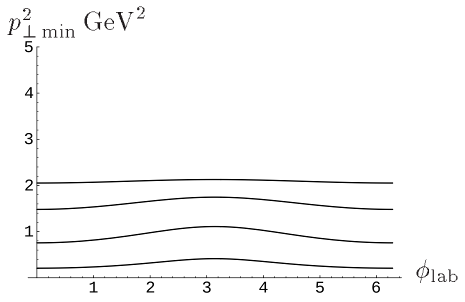

(a) *Azimuthal dependence of $p^2_{\perp\,\mathrm{min}}$ for a pseudo-rapidity gap cut of $\eta_{\mathrm{max}} = 2.5$, with $Q^2 = 30\,GeV^2$, $x_{I\!P} = 0.007$. From the top curve down, β = 0.065, 0.175, 0.375, 0.65. (From the top curve down, $p^2_{\perp\,\mathrm{max}}$ (GeV^2)= 108, 35, 12, 4.)*

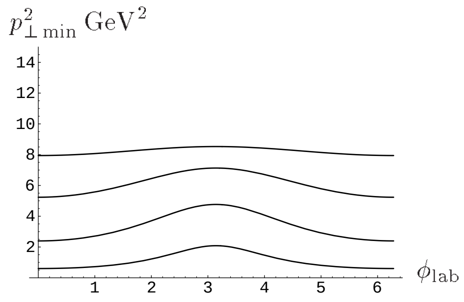

(b) *Azimuthal dependence of $p^2_{\perp\,\mathrm{min}}$ for a pseudo-rapidity gap cut of $\eta_{\mathrm{max}} = 1.8$, with $Q^2 = 30\,GeV^2$, $x_{I\!P} = 0.007$. From the top curve down, β = 0.065, 0.175, 0.375, 0.65. (From the top curve down, $p^2_{\perp\,\mathrm{max}}$ (GeV^2)= 108, 35, 12, 4.)*

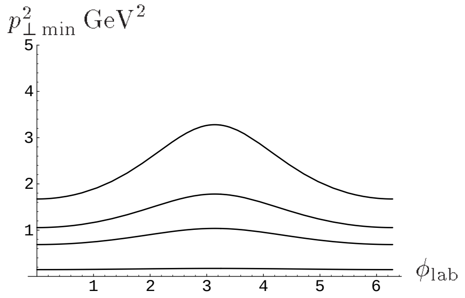

(c) *Azimuthal dependence of $p^2_{\perp\,\mathrm{min}}$ for a pseudo-rapidity gap cut of $\eta_{\mathrm{max}} = 2.5$, with $Q^2 = 30\,GeV^2$, $\beta = 0.4$. From the top curve down, $x_{I\!P}$ = 0.012, 0.009, 0.007, 0.003. (In all of the curves, $p^2_{\perp\,\mathrm{max}} = 18\,GeV^2$.)*

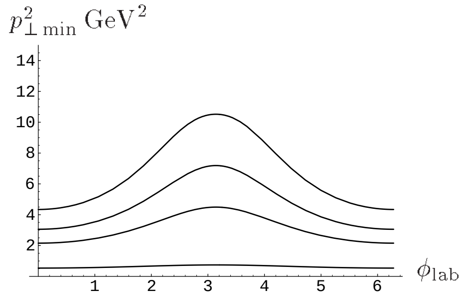

(d) *Azimuthal dependence of $p^2_{\perp\,\mathrm{min}}$ for a pseudo-rapidity gap cut of $\eta_{\mathrm{max}} = 1.8$, with $Q^2 = 30\,GeV^2$, $\beta = 0.4$. From the top curve down, $x_{I\!P}$ = 0.012, 0.009, 0.007, 0.003 (In all of the curves, $p^2_{\perp\,\mathrm{max}} = 18\,GeV^2$.)*

Figure A.3: *Azimuthal angle dependence of transverse momentum phase space constraints.*

A.4 Multi-Jet Virtuality Constraints

A.4.1 Constraints on Multi-Parton Diffractive Final States

The situation is slightly more complicated for the production of multi-parton final states. There is, however, still a wide range of parameter space in Q^2, β and $x_{I\!P}$ in which strong pseudo-rapidity gap cuts result in phase space restrictions and remove contributions from events with resolved pomeron–parton couplings.

It is easiest to consider diffractive multi-jet production processes in the form

$$e(p_e) + P(P) \to e(p_e') + X_1(p_A) + X_2(p_B) + P(P') \,, \tag{A.4.1}$$

where $X = X_1 + X_2$ is the diffractive system and X_2 is the hadronic jet produced by the final-state parton coupled to the pomeron. In this case, X_2 has squared mass $M_{X_2}^2 \lesssim 1\,\mathrm{GeV}^2$. The sum over the jets formed from the other final-state partons in the process, X_1, has squared mass $M_{X_1}^2 < M_X^2$. In the example of three-jet production via photon–gluon fusion, shown in Fig. 1.3(b), X_1 corresponds to the two final-state quark jets and X_2 represents the emitted gluon. These calculations concern constraints on the exchanged parton labeled with momentum k in Fig. A.4 and on the transverse momentum of the parent parton of jet X_2 relative to the forward proton direction.

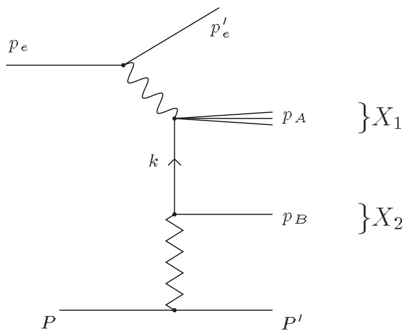

Figure A.4: *Momentum assignments for multi-jet production calculations.*

In the $\gamma^* - I\!P$ CMS, the jet momenta are parameterized by

$$\begin{aligned} p_A &= \gamma \frac{M_X^2}{2} \,(\frac{2-\gamma}{\gamma},\, -\sin\theta_{\mathrm{cms}},\, 0,\, -\cos\theta_{\mathrm{cms}}) \,, \\ p_B &= \gamma \frac{M_X^2}{2} \,(1,\, \sin\theta_{\mathrm{cms}},\, 0,\, \cos\theta_{\mathrm{cms}}) \,, \end{aligned} \tag{A.4.2}$$

where the mass-squared of system X_1 is $(1-\gamma)M_X^2$ and $0 < \gamma \leq 1$. The case $\gamma = 1$ corresponds to dijet production. The pomeron momentum in this frame is

$$P_{I\!P} = (E,\, 0,\, 0,\, E) \,, \tag{A.4.3}$$

where

$$E = \frac{Q^2 + M_X^2}{2M_X} \,. \tag{A.4.4}$$

The momentum of the exchanged parton is given by

$$k = p_A - q = P_{I\!P} - p_B \,, \tag{A.4.5}$$

and therefore the virtuality of the exchanged parton is

$$k^2 = -\gamma \frac{Q^2 + M_X^2}{2} (1 - \cos\theta_{\rm cms})\,. \tag{A.4.6}$$

The constraint from the $\eta_{\rm max}$ cuts derived in Sect. A.2 can be evaded by having γ small.

For the case $\theta_{\rm cms} > 90°$, the condition that the exchanged parton be near mass shall, say $|k^2| \lesssim 1\,{\rm GeV}^2$, is

$$\gamma \leq (1\,{\rm GeV}^2) \frac{2}{Q^2 + M_X^2} = \frac{2}{k^2_{\rm min}\,({\rm GeV}^2)}\,. \tag{A.4.7}$$

For the case of a strong virtuality constraint due to the pseudo-rapidity gap cut, say $k^2_{\rm min} > 6\,{\rm GeV}^2$, Eq. A.4.7 leads to an upper bound on the lower quark momentum fraction of $\gamma \leq 1/33$. This corresponds effectively to a two-jet configuration, because a parton carrying less than 1/33 of the pomeron momentum will not be observed as a jet. The rest of the diffractive system, labeled in Fig. A.4 as p_A, is constrained by the pseudo-rapidity gap cut to carry essentially all of the pomeron momentum. This contribution is included in the model corresponding to leading twist, but not in the models of direct coupling. The non-soft contributions which are genuinely multi-jet processes require high virtuality similar to the two-jet bound given by

$$\begin{aligned} -k^2_{\gamma<1} \geq -k^2_{\rm min} &= \gamma \frac{Q^2 + M_X^2}{2} (1 - \cos\theta^{\rm min}_{\rm cms}) \\ &= -\gamma\, k^2_{\gamma=1}\,, \end{aligned} \tag{A.4.8}$$

where $k^2_{\gamma=1}$ is the minimum virtuality of the exchanged quark in dijet production.

The opening angle of a soft jet is greater than for a jet produced by hadronization of a harder parton. This statement can be quantified by considering the effect of boosts between frames on the opening angle of an hadronic jet. The relevant angles are defined in Fig. A.5.

In the HERA LAB frame θ_1 is the angle between the final-state parton which hadronizes to produce the observed jet and θ_2 is the opening angle of the hadronic jet. Therefore $\theta_1 - \theta_2$ is the angle between the edge of the hadronic jet and the proton direction. The pseudo-rapidity gap is defined in terms of this angle. To estimate the opening angle of a soft jet, assume that the jet produced by a parton of energy E_j has a cone radius of 0.5 to 1 unit of pseudo-rapidity and opening angle θ_2. Boosting to a frame in which the parton has energy $\gamma\, E_j$ (where $0 < \gamma \leq 1$), the opening angle in the new frame, θ_2', can be related to θ_2. For the boost

$$(E_j,\, 0,\, 0,\, E_j) \quad \rightarrow \quad \gamma\,(E_j,\, 0,\, 0,\, E_j)\,, \tag{A.4.9}$$

with boost parameters γ^* and β^*, where $\gamma^* = 1/\sqrt{1 - \beta^{*\,2}}$,

$$\gamma\, E_j \rightarrow \gamma^* (E_j - \beta^*\, E_j) \quad \Rightarrow \quad \gamma = \gamma^* (1 - \beta^*)\,. \tag{A.4.10}$$

The corresponding transformation of angles is

$$\begin{aligned} \tan\theta_2' &= \frac{1}{\gamma^*} \frac{\sin\theta_2}{\cos\theta_2 - \beta^*} \\ &= \frac{1}{\gamma^*} \frac{\sin\theta_2/\cos\theta_2}{1 - \beta^*/\cos\theta_2} \\ &\geq \frac{1}{\gamma^*} \frac{\tan\theta_2}{1 - \beta^*} \end{aligned}$$

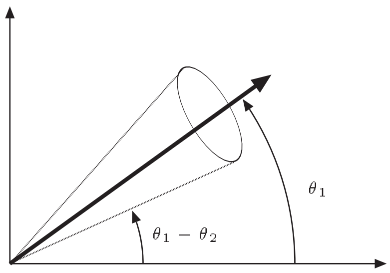

Figure A.5: *Angles involved in parton level and hadron level pseudo-rapidity gap cut phase space constraint calculations.*

$$= \frac{1}{\gamma} \tan\theta_2 \,. \tag{A.4.11}$$

From (A.4.11)

$$\tan\theta_2' \geq \frac{1}{\gamma}\tan\theta_2 \geq \frac{1}{\gamma} 2\tan\frac{\theta_2}{2} \,, \tag{A.4.12}$$

therefore

$$\tan\frac{\theta_2'}{2} \geq \frac{1}{\gamma}\tan\frac{\theta_2}{2}\,(1-\tan^2\frac{\theta_2'}{2}) \,. \tag{A.4.13}$$

To bound $(1-\tan^2\frac{\theta_2'}{2})$, assume that the jet is produced in the forward hemisphere, i.e., that $\theta_1 \leq 90°$. The large pseudo-rapidity gap cut data used in the analysis in Chap. 4 was taken with an experimental cut on pseudo-rapidity of $\eta_{\max} = 1.8$. This corresponds to a minimum angle in the HERA LAB frame of $\theta_{\min}^{\rm lab} \approx 18°$ at hadron level. Therefore

$$\theta_2' \leq \theta_1 - 18° \quad \Rightarrow \quad 1-\tan^2\frac{\theta_2'}{2} \geq 1-\tan^2 36° \approx 0.47 \,, \tag{A.4.14}$$

giving

$$\tan\frac{\theta_2'}{2} \geq \frac{0.47}{\gamma}\tan\frac{\theta_2}{2} \,. \tag{A.4.15}$$

Finally, pseudo-rapidity gap cuts are defined at the experimental level by seeking events with polar angle $\theta_1 - \theta_2$ satisfying the pseudo-rapidity gap cut $\eta_{\max}$. Therefore

$$\begin{aligned}
\eta_{\max}^{\rm expt} &\geq -\ln\tan\left(\frac{\theta_1-\theta_2}{2}\right) \\
&\geq -\ln(\tan\frac{\theta_1}{2} - \tan\frac{\theta_2}{2}) \\
&= -\ln\tan\frac{\theta_1}{2} - \ln\left(1 - \frac{\tan\frac{\theta_2}{2}}{\tan\frac{\theta_1}{2}}\right) \\
&\Rightarrow -\ln\tan\frac{\theta_1}{2} \leq \eta_{\max}^{\rm expt} + \ln\left(1-\frac{\tan\frac{\theta_2}{2}}{\tan\frac{\theta_1}{2}}\right) \,.
\end{aligned} \tag{A.4.16}$$

At the quark–parton level, the angle θ_1 is relevant. Assuming a cone radius of 0.5 to 1 unit of pseudo-rapidity,

$$-\ln\tan\frac{\theta_1}{2} \le \eta^{\rm th}_{\rm max} \approx \eta^{\rm expt}_{\rm max} - (\frac{1}{2} \to 1)\,, \tag{A.4.17}$$

giving

$$\tan\frac{\theta_2}{2} = \left({}^{0.39}_{0.63}\right)\tan\frac{\theta_1}{2}\,, \tag{A.4.18}$$

where the factor 0.39 corresponds to the case of a cone radius of $\frac{1}{2}$ and 0.63 corresponds to unit radius. Combining these results, the bound on multi-jet production can be calculated in terms of the dijet phase space limits. Writing (A.2.18) as

$$(1-\cos\theta^{\rm cms}) = f\,(1-\cos\theta^{\rm lab})\,, \tag{A.4.19}$$

where f is a complicated function of the LAB angles and boost parameters,

$$\begin{aligned}
k^2_{\gamma<1} &= \gamma\frac{Q^2+M_X^2}{2}\,(1-\cos{\theta_1}^{\rm cms})\\
&= \gamma\frac{Q^2+M_X^2}{2}\,f\,(1-\cos{\theta_1}^{\rm lab})\\
&= \gamma\frac{Q^2+M_X^2}{2}\,f\,\tan\frac{{\theta_1}^{\rm lab}}{2}\sin{\theta_1}^{\rm lab}\\
&\ge \gamma\frac{Q^2+M_X^2}{2}\,f\,\tan\frac{{\theta'_2}^{\rm lab}}{2}\sin{\theta_1}^{\rm lab}\\
&\ge 0.47\frac{Q^2+M_X^2}{2}\,f\,\tan\frac{{\theta_2}^{\rm lab}}{2}\sin{\theta_1}^{\rm lab}\\
&= 0.47\frac{Q^2+M_X^2}{2}\,f\,\left({}^{0.39}_{0.63}\right)\tan\frac{{\theta_1}^{\rm lab}}{2}\sin{\theta_1}^{\rm lab}\\
&\approx \left({}^{0.2}_{0.3}\right)\frac{Q^2+M_X^2}{2}\,f\,\tan\frac{{\theta_1}^{\rm lab}}{2}\sin{\theta_1}^{\rm lab}\\
&= \left({}^{0.2}_{0.3}\right)\frac{Q^2+M_X^2}{2}\,f\,(1-\cos{\theta_1}^{\rm lab})\\
&= \left({}^{0.2}_{0.3}\right)\frac{Q^2+M_X^2}{2}\,(1-\cos{\theta_1}^{\rm cms})\,,
\end{aligned} \tag{A.4.20}$$

i.e.,

$$k^2_{\gamma<1} \gtrsim \left({}^{0.2}_{0.3}\right)k^2_{\gamma=1}\,. \tag{A.4.21}$$

This calculation, along with the dijet virtuality limits shown in Table 2.2, shows that for a large region of parameter space resolved-coupling multi-jet production does not contribute to large pseudo-rapidity gap cut diffractive DIS.

A.4.2 3-Jet Production via Final-State Gluon Radiation

There is a scenario which is not covered by either of the cases described above. This is where the lower parton coupled to the pomeron emits QCD radiation after interacting with the pomeron.

Consider the case of dijet production with the modification that the lower quark coupled to the pomeron emits final-state radiation by the emission of a single gluon, as shown in Fig. A.6. In a resolved-coupling picture, the quark labeled p_1 should be close to mass shell. In this case, the quark momentum at the lower vertex, p_1, is shared between the two final-state partons, which, following the argument above means that the jets from the hadronization of these partons will be more spread than the jet from one final-state parton carrying all the momentum. The jets from the final-state partons are all constrained by the pseudo-rapidity gap cuts to be separated from the pomeron direction by a minimum angle $\theta_{\rm min}$ and, since these jets will spread more than a single jet which has not emitted QCD radiation, the angle between the hadronizing partons will be wider. Therefore the minimum constraint in this case is the same as the constraint for a single hard parton at the lower vertex.

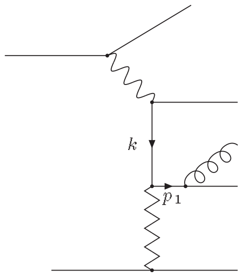

Figure A.6: *Gluon Bremsstrahlung in diffractive DIS.*

The case for single-gluon Bremsstrahlung is sufficient to illustrate that the phase space constraints for emission of one or more final-state partons from the lower line are at least as strong as those for diffractive dijet production.

A.4.3 Jet-Finding Energy Constraints

There is a much weaker, but nevertheless interesting, constraint on diffractive DIS. Jet-finding energies can be used as a way to constrain struck quark virtualities. Consider diffractive production of two or more jets, e.g., the processes of Fig. 1.3. Experimentally, a jet is identified as an isolated set of adjacent calorimeter cells with summed energy greater than 400 MeV [10, 13, 16, 49, 53, 54]. This implies that the parton that has produced the jet has energy greater than 400 MeV. Increasing the jet-finding cut produces a stronger suppression of events. To show this, the procedures developed earlier in this appendix are used, with the diffractive DIS process written in the form

$$e(p_e) + P(P) \to e(p_e') + X_1(p_A) + X_2(p_B) + P(P'), \tag{A.4.22}$$

where again X_2 represents the hadronic jet produced by the lowest final-state parton. Applying two orthogonal boosts to get from the LAB frame to the $\gamma^* - I\!P$ CMS transforms the proton energy to

$$P^0_{\rm cms} = E_P \sqrt{\frac{1+\beta_1}{1-\beta_1}} \frac{1}{\sqrt{1-\beta_2^2}}, \qquad P^0_{\rm lab} = E_P\,, \tag{A.4.23}$$

giving

$$p^0_{B\,\rm cms}(1-\cos\theta_{\rm cms}) = \sqrt{\frac{1-\beta_1}{1+\beta_1}}\sqrt{1-\beta_2^2}\,(1-\cos\theta_{\rm lab})\,P^0_{B\,\rm lab}\,. \tag{A.4.24}$$

The process can be parameterized in the virtual photon–pomeron CMS by

$$q = (M_X - E,\, 0,\, 0,\, -E)$$
$$p_{A\,\rm cms} = (\sqrt{M^2+\kappa^2},\, -\kappa\sin\theta,\, 0,\, -\kappa\cos\theta)$$

$$\begin{aligned} p_{B\,\mathrm{cms}} &= \kappa(1,\, \sin\theta,\, 0,\, \cos\theta) \\ P_{I\!P} &= (E,\, 0,\, 0,\, E)\,, \end{aligned} \tag{A.4.25}$$

where κ is the energy of the lowest final-state parton which couples to the pomeron in the $\gamma^* - I\!P$ CMS. The virtuality, k^2, of the exchanged parton coupled to the pomeron is

$$-k^2 = -(q - p_A{}^2) = -(p_B - P_{I\!P})^2 \approx 2p_B \cdot P_{I\!P} = 2\kappa E(1 - \cos\theta_{\mathrm{lab}})\,. \tag{A.4.26}$$

Now

$$E = \frac{Q^2 + M_X^2}{2M_X} = \frac{Q^2}{2\beta\sqrt{Q^2(\frac{1}{\beta} - \beta)}} = \frac{\sqrt{Q^2}}{2\sqrt{\beta - \beta^2}}\,, \tag{A.4.27}$$

therefore, remembering that

$$1 - \cos\theta_{\mathrm{lab}} = \frac{2e^{-2\eta}}{1 + e^{-2\eta}}\,, \tag{A.4.28}$$

an exchanged-quark virtuality constraint can be written in terms of the minimum jet-finding energy by

$$-k^2_{\mathrm{min}} = \frac{\sqrt{Q^2}}{\sqrt{\beta - \beta^2}}\sqrt{\frac{1 - \beta_1}{1 + \beta_1}}\sqrt{1 - \beta_2^2}\,\frac{2e^{-2\eta_{\mathrm{max}}}}{1 + e^{-2\eta_{\mathrm{max}}}}\kappa_{\mathrm{min}}\,. \tag{A.4.29}$$

H1 and ZEUS require a minimum energy deposition of 400 MeV in adjacent calorimeter cells to identify a jet, therefore $\kappa_{\mathrm{min}} \geq 0.4\,\mathrm{GeV}$. This jet-finding constraint leads to the multi-jet exchanged-quark virtuality constraints shown in Table A.2. Doubling the jet-finding constraint to $\kappa_{\mathrm{min}} = 0.8\,\mathrm{GeV}$ doubles $-k^2_{\mathrm{min}}$. In this case there is a wide range of parameter space for which $-k^2_{\mathrm{min}} > 1\,\mathrm{GeV}^2$. Pseudo-rapidity gap cuts favour events with a low-momentum final-state parton coupling to the pomeron. As a result, the majority of multi-jet production large pseudo-rapidity gap events observed in the HERA collider require at least one of the final-state jets to have small energy. This is consistent with the H1 findings [15] from modelling the pomeron as a two-gluon colour-singlet state. The jet-finding constraint leads to a finite minimum k^2_{min} and since, for relatively small k^2, $p_\perp^2 \approx -(1 - \beta)k^2$, increasing the jet-finding cut will also increase the lower transverse momentum constraint. However, as can be seen from Table A.2, the constraints due to jet-finding cuts are significant only in a small region of HERA phase space and will only become measurably significant if the jet-finding constraint is increased.

Q^2	β	$x_{\mathbb{P}}$	$\lvert k^2_{\rm min}\rvert$ GeV^2 ($\kappa_{\rm min} = 0.4$ GeV)	Q^2	β	$x_{\mathbb{P}}$	$\lvert k^2_{\rm min}\rvert$ GeV^2 ($\kappa_{\rm min} = 0.4$ GeV)
8.5	0.065	0.00365	1.25	25	0.175	0.02410	0.20
		0.00649	0.69			0.04285	0.11
12	0.065	0.00649	0.98		0.375	0.00356	0.69
		0.01154	0.55			0.00632	0.37
		0.02052	0.31			0.01125	0.21
		0.03648	0.17			0.02000	0.11
	0.175	0.00429	0.56		0.65	0.00649	0.21
		0.00762	0.31			0.01154	0.12
		0.01355	0.17	50	0.175	0.00762	1.37
		0.02410	0.10			0.01355	0.74
	0.375	0.00356	0.32			0.02410	0.41
		0.00632	0.17			0.04285	0.23
		0.01125	0.10			0.07620	0.13
	0.65	0.00649	0.10		0.375	0.00356	1.50
25	0.065	0.01154	1.15			0.00632	0.78
		0.02052	0.64			0.01125	0.42
		0.03648	0.36			0.02000	0.23
		0.06488	0.20			0.03556	0.13
	0.175	0.00429	1.20		0.65	0.00649	0.44
		0.00762	0.66			0.01154	0.24
		0.01355	0.36			0.02052	0.13

Table A.2: *Constraints imposed by H1 jet-finding cuts on the virtuality of the exchanged quark coupled to the pomeron in multi-jet diffractive final-state processes such as Fig. 1.3. The parameters correspond to the H1 diffractive DIS analysis in [57].*

Appendix B

Cross Section Calculation Details

B.1 Introduction

The Feynman rules, including a set of rules for form factor pomeron exchange and various useful kinematic results are presented in this chapter. This appendix also contains details of cross section and structure function calculations for the colour-singlet exchange models described in Chap. 3.

B.2 Notes for Cross Section Calculations

B.2.1 Feynman Rules

The vector-pomeron properties described by Donnachie and Landshoff [46, 47] can be easily translated into an additional set of "Feynman Rules".

The pomeron carries no colour but does have vector indices and Regge theory suggests that the total cross section for single pomeron exchange between two partons/hadrons varies approximately as $s^{\alpha_{I\!P}(t)-1}$, where s is the s-channel energy of the interaction and t is the momentum-squared carried by the pomeron. This can be embodied in a Feynman-type rule with a pomeron "propagator" associated with the factor $g^{\mu\nu} s_D^{\alpha_{I\!P}(t)-1}$, where s_D is the diffractive sub-energy of the process involving pomeron exchange. Coupling the pomeron to on-shell quarks with a vector-like coupling, the Donnachie-Landshoff prescription has a coupling constant β_0, giving a factor $\beta_0 \bar{u}(k_2)\gamma_\mu u(k_1)$, where $u(k_1)$ represents a quark of momentum k_1 entering the quark–antiquark–pomeron vertex and $\bar{u}(k_2)$ represents a quark of momentum k_2 leaving the vertex. At each vertex where a quark is replaced by a proton a further factor $3F_1(t_{I\!P})$ is inserted to account for the 3 valence quarks in the proton, where $F_1(t_{I\!P})$ is the Dirac elastic form factor of the proton. The pomeron couples with equal sign to quarks and to antiquarks. For a virtual quark with squared four-momentum $-k^2$ coupling to the pomeron at a $q\bar{q}I\!P$ vertex, a form factor, $f(k^2)$, is introduced to soften the vertex and preserve the experimentally-observed scaling. This is described in detail in Chap. 3. This set of additional rules leads to the correct $x_{I\!P}$ Regge-behaviour of ${x_{I\!P}}^{1-2\alpha_{I\!P}(t_{I\!P})}$ in the diffractive scattering cross section. The Feynman rules for calculating pomeron-exchange diagrams are summarised in Fig. B.1. These rules apply in the Feynman gauge and assume light quarks ($m_q^2 \approx 0$) throughout.

B.2.2 Trace Theorems

The following trace theorems are useful in calculating pomeron exchange cross sections:

Conventions Used in Calculating Feynman Diagrams

(Feynman Gauge)

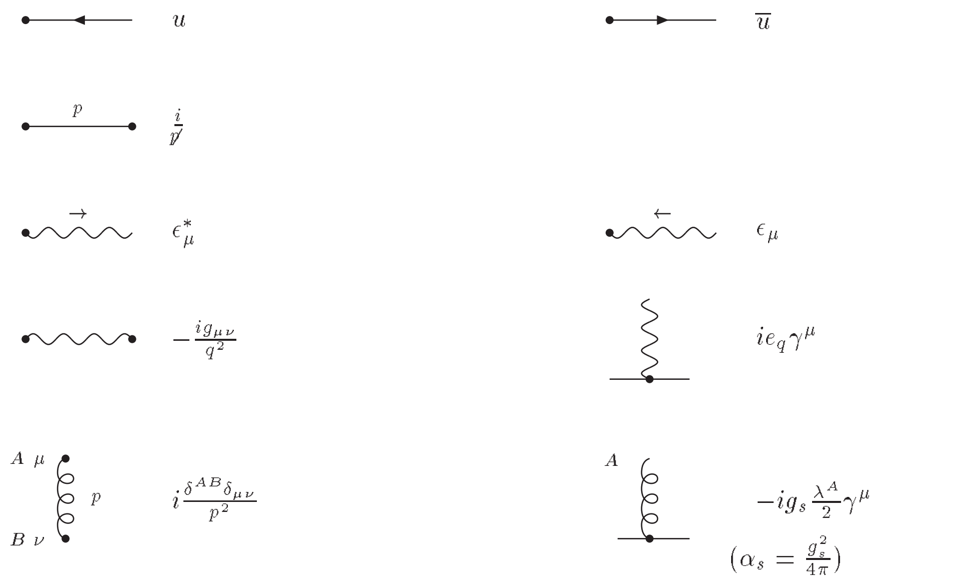

Form Factor Pomeron Exchange Rules

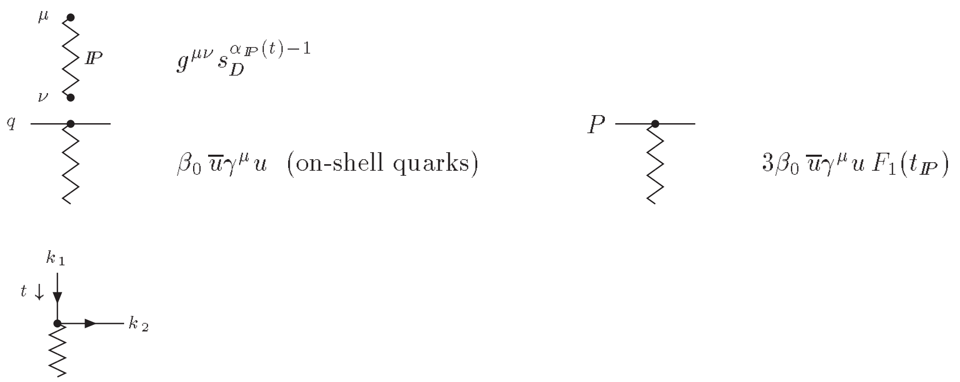

For a virtual quark, k_1, at the $qqI\!P$ vertex introduce a *form factor* $f(k_1^2)$ to restore scaling and account for the fact that k_1 is not on mass shell.

Donnachie-Landshoff: $f(k^2) = \frac{\Lambda^2}{\Lambda^2 - k^2}$ $\quad(\Lambda^2 \sim 1\,\mathrm{GeV}^2)$

Ellis-Ross: $f(k^2) = \sqrt{\frac{\Lambda^2}{\Lambda^2 - k^2}}$ $\quad(\Lambda^2 \sim 1\,\mathrm{GeV}^2)$

Figure B.1: *Rules used in pomeron exchange cross section calculations (in the light quark approximation).*

Dirac Algebra $\gamma^\mu\gamma^\nu + \gamma^\nu\gamma^\mu = 2\, g^{\mu\nu} \Rightarrow \not{a}\not{b} = 2\, a\cdot b - \not{b}\not{a}$,
$\not{a}\gamma_\mu + \gamma_\mu\not{a} = 2a_\mu$

$\mathrm{Tr}\, g_{\mu\nu} = 4 g_{\mu\nu}$

$\gamma^\mu\gamma_\mu = 4$

$\gamma^\mu\not{a}\gamma_\mu = -2\not{a}$

$\gamma^\mu\not{a}\not{b}\gamma_\mu = 4a\cdot b$

$\gamma^\mu\not{a}\not{b}\not{c}\gamma_\mu = -2\not{c}\not{b}\not{a}$

$\mathrm{Tr}\,(\not{a}\not{b}) = 4\, a\cdot b$

$\not{p}\not{p} = p^2$

$\mathrm{Tr}\,(\gamma^\mu\gamma^\nu) = 4g^{\mu\nu}$

$\mathrm{Tr}\,(\not{P}\gamma_\beta) = 4P_\beta$

$\mathrm{Tr}\,(\not{a}\not{b}\not{c}\not{d}) = 4\,[(a\cdot b)(c\cdot d) - (a\cdot c)(b\cdot d) + (a\cdot d)(b\cdot c)]$

$\mathrm{Tr}\,(\not{a}\not{b}\not{a}\not{d}) = 4\,[2\,(a\cdot b)(a\cdot d) - a^2\,(b\cdot d)]$

$\mathrm{Tr}\,(\gamma^\alpha\gamma^\beta\gamma^\lambda\gamma^\tau) = 4\,[g^{\alpha\beta}g^{\lambda\tau} - g^{\alpha\lambda}g^{\beta\tau} + g^{\alpha\tau}g^{\beta\lambda}]$

$\mathrm{Tr}\,(\not{k}_1\gamma^\mu\not{k}_2\gamma^\nu) = 4\,[k_1^\mu k_2^\nu + k_1^\nu k_2^\mu - (k_1\cdot k_2)\, g^{\mu\nu}]$

Special case :

$$\begin{aligned}
\mathrm{Tr}\,(\not{k}_1\gamma^\mu\not{k}_2\gamma^\nu) & \qquad : \quad k_1 \approx k_2, \quad k_1^2 = k_2^2 = 0 \\
&= 4\,[k_1^\mu k_2^\nu + k_1^\nu k_2^\mu - k_1\cdot k_2 g^{\mu\nu}] \\
&\approx 8\, k_1^\mu k_1^\nu
\end{aligned}$$

$$\begin{aligned}
\mathrm{Tr}\,(\gamma_a\gamma_b\gamma_c\gamma_d\gamma_e\gamma_f) = 4\ [&g_{ef}\,(g_{ab}g_{cd} - g_{ac}g_{bd} + g_{ad}g_{bc}) \\
&- g_{df}\,(g_{ab}g_{ce} - g_{ac}g_{be} + g_{ae}g_{bc}) \\
&+ g_{cf}\,(g_{ab}g_{de} - g_{ad}g_{be} + g_{ae}g_{bd}) \\
&- g_{bf}\,(g_{ac}g_{de} - g_{ad}g_{ce} + g_{ae}g_{cd}) \\
&+ g_{af}\,(g_{bc}g_{de} - g_{bd}g_{ce} + g_{be}g_{cd})\ ]
\end{aligned}$$

Equivalently

$$\begin{aligned}
\mathrm{Tr}\,(\not{a}\not{b}\not{c}\not{d}\not{e}\not{f}) = 4\ [&(e\cdot f)\,[(a\cdot b)\,(c\cdot d) - (a\cdot c)\,(b\cdot d) + (a\cdot d)\,(b\cdot c)] \\
&- (d\cdot f)\,[(a\cdot b)\,(c\cdot e) - (a\cdot c)\,(b\cdot e) + (a\cdot e)\,(b\cdot c)] \\
&+ (c\cdot f)\,[(a\cdot b)\,(d\cdot e) - (a\cdot d)\,(b\cdot e) + (a\cdot e)\,(b\cdot d)] \\
&- (b\cdot f)\,[(a\cdot c)\,(d\cdot e) - (a\cdot d)\,(c\cdot e) + (a\cdot e)\,(c\cdot d)] \\
&+ (a\cdot f)\,[(b\cdot c)\,(d\cdot e) - (b\cdot d)\,(c\cdot e) + (b\cdot e)\,(c\cdot d)]\ ]
\end{aligned}$$

B.2.3 Useful Kinematic Results

Feynman diagram arrows show direction of *momenta*

$W^2 >> M_X^2 >> Q^2$

$x_{\mathrm{Bj}} << 1$

$\alpha_{\mathrm{em}} = \dfrac{e^2}{4\pi}$

Cross section : $\mathrm{d}\sigma = \dfrac{\overline{|\mathcal{M}|}^2}{F}\,\mathrm{d}\Gamma$

Structure function as a function of 4 variables (neglecting $y^2 F_L^{D(4)}$) :

$$\frac{\mathrm{d}^4\sigma_{\mathrm{diff}}}{\mathrm{d}\beta\,\mathrm{d}Q^2\,\mathrm{d}x_{I\!P}\,\mathrm{d}t_{I\!P}} = \frac{2\pi\alpha^2}{\beta Q^4}\,[1+(1-y)^2]\,F_2^{D(4)}(\beta, Q^2, x_{I\!P}, t_{I\!P})$$

Diffractive energies :

$$s_{D_1} = (p_B + P')^2 = P'^2 + 2P' \cdot p_B \approx -\frac{t}{x_{I\!P}}$$
$$s_{D_2} = (p_A + P')^2 = P'^2 + 2P' \cdot p_A \approx -\frac{u}{x_{I\!P}}$$

Flux factor for particles a and b colliding :
$\mathrm{F} = 4[(p_a \cdot p_b)^2 - m_a^2\, m_b^2]^{\frac{1}{2}}$,
so, for $e - P$ scattering,
$F = 4\, P \cdot p_e = 2S_{\mathrm{Tot}} \qquad (S_{\mathrm{Tot}} >> m_P^2)$.

The Mandelstam variables for the $\gamma^*(q) + I\!P(x_{I\!P} P) \longrightarrow \mathrm{jet}(p_A) + \mathrm{jet}(p_B)$ subprocess (with light quarks) are:

$$\begin{aligned}
s = M_X^2 &= (q + x_{I\!P} P)^2 \approx 2x_{I\!P}\, P \cdot q - Q^2 \qquad = (p_A + p_B)^2 \approx 2p_A \cdot p_B \\
t &= (q - p_A)^2 \approx -2q \cdot p_A - Q^2 \\
&= (p_B - x_{I\!P} P)^2 \approx -2x_{I\!P}\, P \cdot p_B \\
u &= (q - p_B)^2 \approx -2q \cdot p_B - Q^2 \\
&= (p_A - x_{I\!P} P)^2 \approx -2x_{I\!P}\, P \cdot p_A \\
s + t + u &= -Q^2 .
\end{aligned}$$

B.3 Cross Section and Structure Function Calculations

B.3.1 Introduction

Details of the cross section and structure function calculations involving the colour-singlet exchange models are presented in this appendix. The calculations relate to the diffractive dijet production process described in Chap. 3 in which the virtual photon dissociates into a quark–antiquark pair which then interacts with the proton via colour-singlet exchange. This chapter starts with the 4-body phase space element calculation common to all of the models, followed by calculations of the invariant matrix elements for the individual models. The differential scattering cross section and diffractive structure function are calculated for each model and the behaviour of the models in various regions of parameter space is studied.

The cross section is calculated differential with respect to Q^2, β, $x_{I\!P}$ and $p_\perp^2$ from which the diffractive structure function, unintegrated with respect to $p_\perp^2$, can be determined. The $p_\perp^2$-integral is then carried out, integrating over the experimentally-accessible range of $p_\perp^2$, to find the diffractive structure function extracted from the large pseudo-rapidity gap cut experiments. Having calculated $p_{\perp\,\mathrm{min}}^2$ appropriate to the parameters Q^2, β, $x_{I\!P}$ and η_{max}, the structure function can be integrated over $p_\perp^2$ from $p_{\perp\,\mathrm{min}}^2$ up to the maximum value of $p_\perp^2$, namely, $M_X^2/4$. This is different to approaches used before as the constraints on the range of the struck-quark virtuality, as well as on the jet transverse momentum, imposed by strong pseudo-rapidity gap cuts are taken into account.

The differential cross section is defined by

$$\mathrm{d}\sigma = \frac{1}{F}\, |\overline{\mathcal{M}}|^2\, \mathrm{d}\Gamma\,, \tag{B.3.1}$$

where F is the flux factor and $\mathrm{d}\Gamma$ is the invariant phase space element. The flux factor for electron–proton scattering with fixed CMS energy is

$$F = 4\, P \cdot p_e = 2S_{\mathrm{Tot}} \qquad (S_{\mathrm{Tot}} >> m_P^2)\,. \tag{B.3.2}$$

Throughout this analysis the proton mass, m_{P}, is neglected relative to larger momentum scales.

B.3.2 Phase Space Element

It is easiest to calculate the contribution to the phase space element from the outgoing electron in the electron–proton CMS. The rest of the phase space element is calculated in the $\gamma^* - I\!P$ CMS. The azimuthal angle element $\mathrm{d}\phi$ is invariant under the transformation between the $e - P$ CMS and the $\gamma^* - I\!P$ CMS (this is demonstrated at the end of this section).

The electron–proton CMS is related to the HERA LAB system by a boost in the z-direction. The z-axis is chosen to be in the proton direction and the axes are aligned such that the photon is in the xz-plane. The momenta of the particles are parameterized as in Fig. B.2.

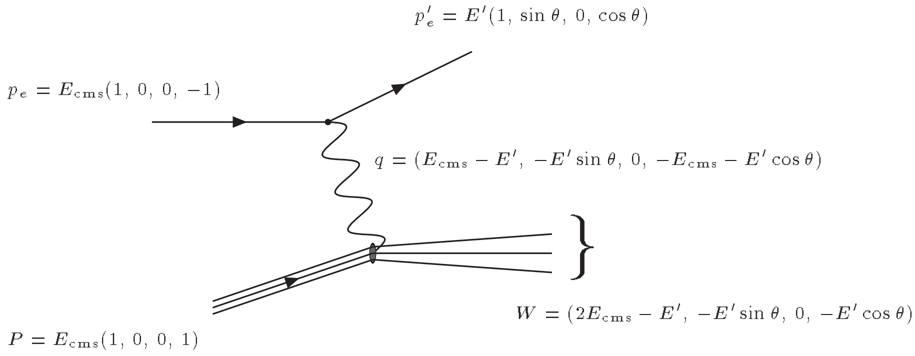

Figure B.2: *Momentum assignments for lepton phase space contribution calculations (in $e - P$ CMS).*

In terms of the momentum assignments in Fig. B.2, the invariants Q^2 and W^2 are

$$\begin{aligned} Q^2 &= -q^2 = -(p_e' - p_e)^2 = 2p_e' \cdot p_e = 2E_{\mathrm{cms}}E'(1+\cos\theta)\,, && \text{(B.3.3)}\\ W^2 &= 4E_{\mathrm{cms}}^2 - 4E_{\mathrm{cms}}E' + E'^{\,2} - E'^{\,2}\sin^2\theta\cos^2\phi - E'^{\,2}\sin^2\theta \\ &= 4E_{\mathrm{cms}}^2 - 4E_{\mathrm{cms}}E'\,. && \text{(B.3.4)} \end{aligned}$$

The phase space contribution from the outgoing electron is

$$\mathrm{d}\Gamma_{\mathrm{elec}} = \frac{\mathrm{d}^3\underline{p}_e'}{(2\pi)^3 2p_e'^{\,0}} = \frac{E'\,\mathrm{d}E'\,\mathrm{d}\cos\theta\,\mathrm{d}\phi}{2(2\pi)^3}\,. \tag{B.3.5}$$

Changing variables from E' and $\cos\theta$ to the invariants Q^2 and W^2, involves the Jacobian

$$\frac{\partial(Q^2,\,W^2)}{\partial(E',\,\cos\theta)} = -\frac{\partial Q^2}{\partial\cos\theta}\,\frac{\partial W^2}{\partial E'} = 8E_{\mathrm{cms}}^2E'\,, \tag{B.3.6}$$

so that

$$\mathrm{d}\Gamma_{\mathrm{elec}} = \frac{\mathrm{d}Q^2\,\mathrm{d}W^2\,\mathrm{d}\phi}{2^4(2\pi)^3E_{\mathrm{cms}}^2}\,. \tag{B.3.7}$$

The total energy of the $e - P$ interaction is

$$S_{\mathrm{Tot}} = (P + p_e)^2 \approx 4E^2_{\mathrm{cms}} , \tag{B.3.8}$$

and changing variables from W^2 to $x_{I\!P}$ gives

$$x_{I\!P} = \frac{Q^2 + M_X^2}{Q^2 + W^2} \Rightarrow \mathrm{d}W^2 = -\frac{Q^2 + M_X^2}{{x_{I\!P}}^2}\mathrm{d}x_{I\!P} , \tag{B.3.9}$$

so that

$$\mathrm{d}\Gamma_{\mathrm{elec}} = -\frac{(Q^2 + M_X^2)}{(2\pi)^3 4{x_{I\!P}}^2 s_{\mathrm{Tot}}} \mathrm{d}Q^2 \,\mathrm{d}x_{I\!P} \,\mathrm{d}\phi . \tag{B.3.10}$$

Since $\mathrm{d}\phi$ is invariant under a boost from the $e - P$ CMS to the $\gamma^* - I\!P$ CMS, this result is also the contribution to the invariant phase space element from the outgoing electron in the $\gamma^* - I\!P$ CMS.

In the $\gamma^* - I\!P$ CMS (with momenta as shown in Fig. B.3), the rest of the phase space element is

$$\mathrm{d}\Gamma_{\mathrm{had}} = \frac{\mathrm{d}^3\underline{p}_A}{(2\pi)^3 2{p_A}^0} \frac{\mathrm{d}^3\underline{p}_B}{(2\pi)^3 2{p_B}^0} \frac{\mathrm{d}^3\underline{P}'}{(2\pi)^3 2P'^0} (2\pi)^4\delta^4(p_e' + p_A + p_B + P' - p_e - P) . \tag{B.3.11}$$

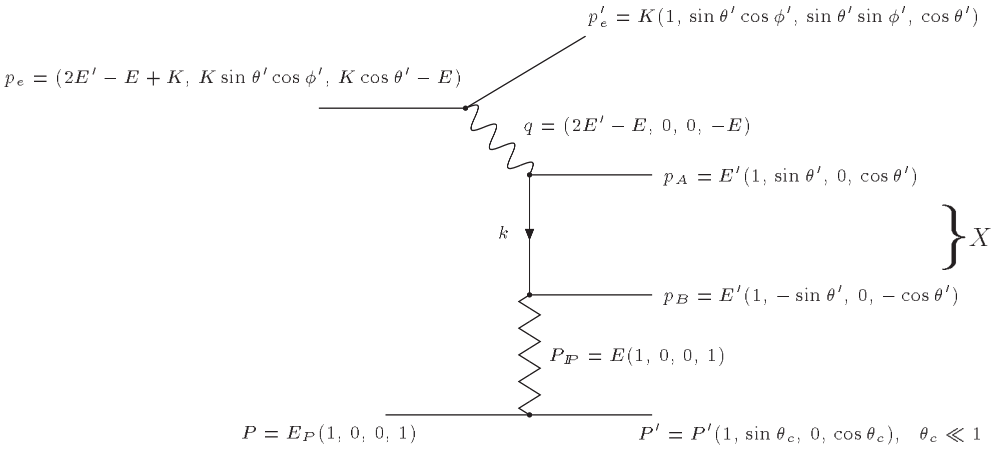

Figure B.3: *Momentum assignments for cross section calculations in the* $\gamma^* - I\!P$ *CMS.*

Now

$$\frac{\mathrm{d}^3\underline{p}_A}{{p_A}^0} = E'\mathrm{d}E'\mathrm{d}\cos\theta\mathrm{d}\phi , \tag{B.3.12}$$

the mass of the diffractive system is given by

$$M_X^2 = ({p_A}^2 + {p_B}^2) = 4E'^2 , \tag{B.3.13}$$

and the four-momentum of the virtual photon is

$$Q^2 = -q^2 = 4EE' - 4E'^2 . \tag{B.3.14}$$

Therefore

$$E = \frac{Q^2 + M_X^2}{2M_X} . \tag{B.3.15}$$

The transverse momentum of the jets, $p_\perp$, with respect to the forward proton direction is defined in terms of the diffractive mass and the polar angle of the parton which produces the jet by

$$p_\perp = E' \sin\theta \Rightarrow p_\perp^2 = E'^2(1-\cos\theta^2)\,, \tag{B.3.16}$$

so that

$$\cos\theta = \sqrt{1-\frac{4p_\perp^2}{M_X^2}}\,. \tag{B.3.17}$$

Both $\cos\theta$ and $\mathrm{d}\cos\theta$ change sign at $\theta = \pi/2$. However, since only the product of these two factors appears in the calculations, there is change of sign in the terms involving θ. Furthermore, there is an additional factor of 2 that must be introduced into the phase space element when converting from an integral over θ to an integral over $p_\perp^2$ due to the symmetry of $\cos\theta \mathrm{d}\theta$ for $0 \leq \theta < \pi/2$ and $\pi/2 \leq \theta < \pi$. Changing variables from E' and $\cos\theta$ in the CMS to M_X^2 and $p_\perp^2$ gives

$$\begin{aligned}\frac{\partial(M_X^2, p_\perp^2)}{\partial(E', \cos\theta)} &= \frac{\partial M_X^2}{\partial E'}\frac{\partial p_\perp^2}{\partial\cos\theta} \\ &= (8E')(2E'\cos\theta) \\ &= -2M_X^3\sqrt{1-\frac{4p_\perp^2}{M_X^2}}\,.\end{aligned} \tag{B.3.18}$$

The integral over the azimuthal angle of the final state quarks is trivial giving, with the inclusion of the factor of 2 from the change of variables from $\cos\theta$ to $p_\perp^2$,

$$\begin{aligned}\frac{\mathrm{d}^3\underline{p}_A}{p_A{}^0} &= \left(\frac{M_X}{2}\right)\left[\frac{\mathrm{d}M_X^2\,\mathrm{d}p_\perp^2}{-M_X^3\sqrt{1-\frac{4p_\perp^2}{M_X^2}}}2\pi\right] \\ &= -\frac{\pi \mathrm{d}M_X^2\,\mathrm{d}p_\perp^2}{M_X^2\sqrt{1-\frac{4p_\perp^2}{M_X^2}}}\,.\end{aligned} \tag{B.3.19}$$

Furthermore

$$\begin{aligned}&\frac{\mathrm{d}^3\underline{p}_B}{p_B{}^0}\frac{\mathrm{d}^3\underline{P}'}{P'^0}\delta^4(p_e'+p_A+p_B+P'-p_e-P) \\ &= \frac{\mathrm{d}^3\underline{P}'}{p_B{}^0P'^0}\delta(p_e'^0+p_A{}^0+p_B{}^0+P'^0-p_e^0-P^0) \\ &= \frac{P'\mathrm{d}P'\mathrm{d}\cos\theta_c\mathrm{d}\phi_c}{E'}\delta(p_e'^0+p_A{}^0+p_B{}^0+P'^0-p_e^0-P^0) \\ &= \frac{E_P\mathrm{d}\cos\theta_c\mathrm{d}\phi_c}{E'} \\ &= \frac{4\pi}{M_X}E_P\mathrm{d}\cos\theta_c\,.\end{aligned} \tag{B.3.20}$$

Assuming that the pomeron is emitted approximately in the same direction as the proton, the pomeron energy is given by

$$E = x_{I\!P} E_P \,. \tag{B.3.21}$$

The momentum transfer at the proton vertex, $t_{I\!P}$, must be taken into account at this stage. In terms of the incoming and outgoing proton momenta and the scattering angle of the proton, $\cos\theta_c$,

$$t_{I\!P} = (P - P')^2 \approx 2P \cdot P' = -2E_P p' \left(1 - \cos\theta_c\right), \tag{B.3.22}$$

giving

$$E_P \mathrm{d}\cos\theta_c = E_P \frac{\mathrm{d}t_{I\!P}}{2p'} \approx \frac{M_X x_{I\!P} \mathrm{d}t_{I\!P}}{Q^2 + M_X^2} \,. \tag{B.3.23}$$

Therefore the contribution to the phase space element from the hadronic final state is

$$\begin{aligned} \mathrm{d}\Gamma_{\text{had}} &= \frac{1}{2^3 (2\pi)^5} \left(-\frac{\pi}{M_X^2} \frac{\mathrm{d}M_X^2 \mathrm{d}p_\perp^2}{\sqrt{1 - \frac{4p_\perp^2}{M_X^2}}} \right) \left(\frac{4\pi}{M_X} \frac{M_X x_{I\!P} \mathrm{d}t_{I\!P}}{(Q^2 + M_X^2)} \right) \\ &= -\frac{1}{(2\pi)^3} \frac{x_{I\!P} \mathrm{d}M_X^2 \mathrm{d}p_\perp^2 \mathrm{d}t_{I\!P}}{2^3 M_X^2 (Q^2 + M_X^2)} \frac{1}{\sqrt{1 - \frac{4p_\perp^2}{M_X^2}}} \,. \end{aligned} \tag{B.3.24}$$

This leads to a total final-state phase space element for diffractive dijet production of

$$\begin{aligned} \mathrm{d}\Gamma &= \frac{(2\pi)^4}{((2\pi)^3)^4} \frac{\mathrm{d}^3 \underline{p}_e'}{2p_e'^0} \frac{\mathrm{d}^3 \underline{p}_A}{2p_A{}^0} \frac{\mathrm{d}^3 \underline{p}_B}{2p_B{}^0} \frac{\mathrm{d}^3 \underline{P}'}{2P'^0} \delta^4(p_e' + p_A + p_B + P' - P - p_e) \\ &= \left(\frac{-(Q^2 + M_X^2) \mathrm{d}Q^2 \mathrm{d}x_{I\!P} \mathrm{d}\phi}{(2\pi)^3 4 x_{I\!P}{}^2 S_{\text{Tot}}} \right) \left(\frac{-x_{I\!P} \mathrm{d}M_X^2 \mathrm{d}p_\perp^2 \mathrm{d}t_{I\!P}}{(2\pi)^3 2^3 M_X^2 (Q^2 + M_X^2)} \frac{1}{\sqrt{1 - \frac{4p_\perp^2}{M_X^2}}} \right) \\ &= \frac{\mathrm{d}Q^2 \mathrm{d}M_X^2 \mathrm{d}p_\perp^2 \mathrm{d}x_{I\!P} \mathrm{d}t_{I\!P} \mathrm{d}\phi}{2^5 (2\pi)^6 x_{I\!P} S_{\text{Tot}} M_X^2} \frac{1}{\sqrt{1 - \frac{4p_\perp^2}{M_X^2}}} \,, \end{aligned} \tag{B.3.25}$$

where ϕ is the azimuthal angle of the outgoing electron.

Effect of Frame Boosts on Azimuthal Angle Element

The invariance of infinitesimal azimuthal angles under Lorentz boosts between inertial reference frames is demonstrated in this section.

Starting in the electron–proton CMS, the four-vector describing the diffractive system, X, is parameterized most generally by

$$X = (X_0,\, X\sin\theta\cos\phi,\, X\sin\theta\sin\phi,\, X\cos\theta) \,. \tag{B.3.26}$$

The momentum of the outgoing electron in the $e - P$ CMS can be written

$$p_e' = (p_e'^{\,0},\, p_e'\sin\theta\cos\phi,\, p_e'\sin\theta\sin\phi,\, p_e'^{\,z}) \,, \tag{B.3.27}$$

where the angles θ and ϕ are the same as for the diffractive system. The projection of p_e' onto the xy-plane is therefore parallel to the projection of the diffractive 4-vector, X, onto the xy-plane.

Using two orthogonal boosts to get from the HERA LAB frame to the $\gamma^* - I\!P$ CMS, which is also the rest frame of X, it is possible to demonstrate that the total boost leaves the azimuthal angle element $\mathrm{d}\phi$ of the outgoing electron invariant. The first boost is in the z-direction. This is perpendicular to the plane in which the azimuthal angle ϕ is defined and therefore leaves ϕ invariant. Since the boost in the z-direction does not change the momentum components in the x or y directions, the projections of X and p'_e onto the xy-plane are still parallel. This boost is also orthogonal to the direction of increasing ϕ and will not effect small elements of azimuthal angle describing the outgoing electron direction. The first boost is a transformation to a frame in which the vector produced by transforming X has only x and y spatial components. To get to the CMS of the virtual photon–pomeron system, a boost is required in the direction of the remaining spatial part of X. However, as is shown in Fig. B.4, the vector $\mathrm{d}\phi$ which describes small changes in the azimuthal angle is perpendicular to the boost direction. This demonstrates that small changes in ϕ are not affected by this boost.

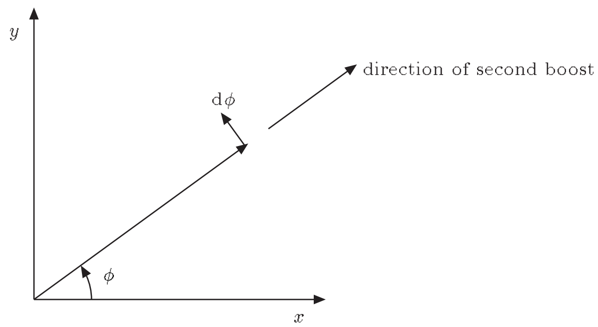

Figure B.4: *The boost from the $x - y$ projection of the 3-momentum of the diffractive system to the $\gamma^* - I\!P$ CMS.*

It has therefore been shown that the infinitesimal angle, $\mathrm{d}\phi$, which occurs in the phase space element for the outgoing electron is invariant under the boost between the two frames. This demonstrates the validity of the use of the two different frames to calculate different parts of the phase space element for diffractive DIS dijet production.

B.3.3 Form Factor Models

Details of the form factor model cross section and structure function calculations are given in Sect. 3.8.2. The full cross section for the form factor models of diffractive dijet production is given by Eq. 3.8.19 and is repeated here in Eq. B.3.28.

$$\frac{\mathrm{d}\sigma}{\mathrm{d}Q^2\,\mathrm{d}M_X^2\,\mathrm{d}p_\perp^2\,\mathrm{d}x_{I\!P}} = \frac{9\,2^4 e^4 e_q^2 \beta_0^4 b^2}{(Q^2+M_X^2)^2\,Q^4\,x_{I\!P}\,(2\pi)^5 M_X^2}\,\frac{1}{\sqrt{1-\frac{4p_\perp^2}{M_X^2}}}$$
$$\left\{(Q^2M_X^2 - 2Q^2p_\perp^2)\,[1+(1-y)^2] + \frac{2p_\perp^2}{M_X^2}(Q^2-M_X^2)^2\,(1-y)\right\}$$
$$[f(t)^2\, s_{D_1}^{2[\alpha_{I\!P}(0)-1]} + f(u)^2\, s_{D_2}^{2[\alpha_{I\!P}(0)-1]} + 2f(t)\,f(u) s_{D_1}^{\alpha_{I\!P}(0)-1} s_{D_2}^{\alpha_{I\!P}(0)-1}]\,. \tag{B.3.28}$$

B.3.4 Single-Gluon Model

The single-gluon exchange diffractive dijet production cross section is calculated by squaring the sum of the diagram in Fig. B.5 and the equivalent diagram with the quark line reversed. In these diagrams the exchanged gluon carries (small) momentum fraction $x_{I\!P}$ of the parent proton momentum P. The matrix element is calculated following the Feynman rules in Sect. B.2.1, giving

$$\overline{|\mathcal{M}_1|}^2 = \frac{1}{2}\frac{1}{2}(e^4 e_q^2)\frac{g^{\mu\mu'}g^{\nu\nu'}}{q^4}\frac{\delta^{\alpha\alpha'}\delta^{\beta\beta'}}{(x_{I\!P}P)^4}\frac{1}{(q-p_A)^4}$$
$$\mathrm{Tr}\,[\not{p}_e\gamma_{\mu'}\not{p}'_e\gamma_{\nu'}]\,\mathrm{Tr}\,[\gamma_\mu(\not{q}-\not{p}_A)\gamma_\alpha\not{p}_B\gamma_\beta(\not{q}-\not{p}_A)\gamma_\nu\not{p}_A]\,\mathrm{Tr}\,[\not{P}\gamma_{\alpha'}\not{P}'\gamma_{\beta'}]\,, \tag{B.3.29}$$

where the factors preceding the traces are from (starting from the left): average over incoming electron spins, average over incoming proton spins, contribution from virtual photon–quark and virtual photon–electron vertices, photon propagators, gluon propagators, scalar denominators from quark propagators. Here the gluon distribution in the photon has been approximated by a δ-function, thereby absorbing the gluon distribution function of the proton into the overall normalisation (which is the free parameter of the calculation).

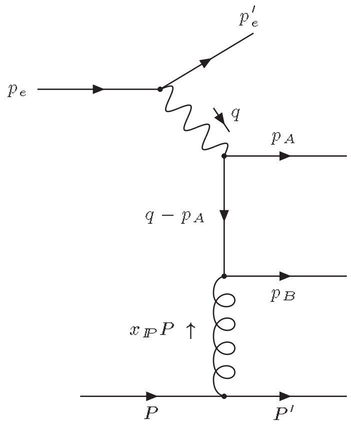

Figure B.5: *First diagram contributing to diffractive DIS via single-gluon exchange.*

As a result of the gauge invariance of this calculation, the contribution from the parts of the lepton trace proportional to the photon momentum, q, and the contribution from parts of the proton trace proportional to the gluon momentum, $x_{I\!P}P$, will cancel with other terms of the invariant matrix element. The non-canceling contributions from the lepton and proton traces to the matrix element are

$$\begin{aligned}\mathrm{Tr}\,(\not{p}_e\gamma_\mu\not{p}'_e\gamma_\nu) &= 4[p_{e\mu}p'_{e\nu} + p_{e\nu}p'_{e\mu} - g_{\mu\nu}p_e\cdot p'_e] \\ &\to 4[2p_{e\mu}p_{e\nu} - g_{\mu\nu}\frac{Q^2}{2}]\,,\end{aligned} \tag{B.3.30}$$

and[1]

[1] In contrast to Eq. B.3.31, in the form factor model calculations the completeness relation applied to the proton lines was written as $\sum_{\mathrm{spins}}(\mathrm{proton}) = 1/\not{P}$, rather than $1/(\not{P} - m_P)$ because the contribution from the second (proton mass) term was negligible compared to the contribution from $\not{P}$ in the form factor model case. This is a consequence of the C-even nature of the pomeron and the consequent gauge

$$\begin{aligned}
\mathrm{Tr}\,(\,(\not{P}+m_P)\gamma_\alpha(\not{P}'+m_P)\gamma_\beta) &= \mathrm{Tr}\,(\not{P}\gamma_\alpha\not{P}'\gamma_\beta) + m_P^2\,\mathrm{Tr}\,(\,\gamma_\alpha\gamma_\beta) \\
&= 4[P_\alpha P'_\beta + P_\beta P'_\alpha - g_{\alpha\beta}P\cdot P'] + 4m_P^2 g_{\alpha\beta} \\
&= 4[P_\alpha P'_\beta + P_\beta P'_\alpha - g_{\alpha\beta}m_P^2(1-x_{I\!P})] + 4m_P^2 g_{\alpha\beta} \\
&\to 4x_{I\!P}m_P^2 g_{\alpha\beta}. \qquad (B.3.31)
\end{aligned}$$

Applying the trace theorems in Sect. B.2.2 and momentum conservation, the first contribution to the matrix element can be written

$$\begin{aligned}
\overline{|\mathcal{M}_1|}^2 &= \frac{e^4e_q^2}{4Q^4(x_{I\!P}P)^4t^2}\,2[4p_e{}^\mu p_e{}^\nu - Q^2g^{\mu\nu}]\,4x_{I\!P}m_P^2g^{\alpha\beta} \\
&\quad \mathrm{Tr}\,[\gamma_\mu(\not{q}-\not{p}_A)\gamma_\alpha\not{p}_B\gamma_\beta(\not{q}-\not{p}_A)\gamma_\nu\not{p}_A] \\
&= \frac{2e^4e_q^2}{Q^4m_P^2x_{I\!P}{}^3t^2}\,[4p_e{}^\mu p_e{}^\nu - Q^2g^{\mu\nu}]\,\mathrm{Tr}\,[\gamma_\mu(\not{q}-\not{p}_A)\gamma_\alpha\not{p}_B\gamma^\alpha(\not{q}-\not{p}_A)\gamma_\nu\not{p}_A] \\
&= \frac{2e^4e_q^2}{Q^4m_P^2x_{I\!P}{}^3t^2}\Big(4\,\mathrm{Tr}\,[\not{p}_e(\not{p}_B - x_{I\!P}\not{P})(-2\not{p}_B)(\not{p}_B - x_{I\!P}\not{P})\not{p}_e\not{p}_A] \\
&\quad -Q^2\,\mathrm{Tr}\,[(-2\not{p}_A)(\not{p}_B - x_{I\!P}\not{P})(-2\not{p}_B)(\not{p}_B - x_{I\!P}\not{P})]\Big) \\
&= -\frac{2^3e^4e_q^2}{Q^4m_P^2x_{I\!P}t^2}\Big(2\,\mathrm{Tr}\,[\not{p}_e\not{P}\not{p}_B\not{P}\not{p}_e\not{p}_A] + Q^2\,\mathrm{Tr}\,[\not{p}_A\not{P}\not{p}_B\not{P}]\Big) \\
&= -\frac{2^3e^4e_q^2}{Q^4m_P^2x_{I\!P}t^2}\Big(2(2p_e\cdot p_A)(2P\cdot p_B)(4P\cdot p_e) + Q^2(2P\cdot p_B)(4P\cdot p_A)\Big) \\
&= -\frac{2^3e^4e_q^2}{Q^4m_P^2x_{I\!P}t^2}\Big(2(2p_e\cdot p_A)(-\frac{t}{x_{I\!P}})(2S_{\mathrm{Tot}}) + Q^2(-\frac{t}{x_{I\!P}})(-2\frac{u}{x_{I\!P}})\Big) \\
&= \frac{2^4e^4e_q^2}{Q^4m_P^2tx_{I\!P}{}^3}\Big(4(p_e\cdot p_A)x_{I\!P}S_{\mathrm{Tot}} - Q^2u\Big). \qquad (B.3.32)
\end{aligned}$$

The second term in the matrix element is obtained from $\overline{|\mathcal{M}_1|}^2$ by swapping p_A and p_B as well as t and u in Eq. B.3.32, giving

$$\overline{|\mathcal{M}_2|}^2 = \frac{2^4e^4e_q^2}{Q^4m_P^2ux_{I\!P}{}^3}\Big(4(p_e\cdot p_B)x_{I\!P}S_{\mathrm{Tot}} - Q^2t\Big). \qquad (B.3.33)$$

The contributions from the two mixed diagrams, $\overline{|\mathcal{M}_{12}|}$ and $\overline{|\mathcal{M}_{21}|}$, must also be included. The contribution from the first mixed term, $\overline{|\mathcal{M}_{12}|}$, is calculated using Fig. B.6 (with the diagram cut vertically), giving

$$\begin{aligned}
\overline{|\mathcal{M}_{12}|} &= \frac{1}{2}\frac{1}{2}(e^4e_q^2)\frac{g^{\mu\mu'}g^{\nu\nu'}}{q^4}\frac{\delta^{\alpha\alpha'}\delta^{\beta\beta'}}{(x_{I\!P}P)^4}\frac{1}{(q-p_A)^2}\frac{1}{(q-p_B)^2} \\
&\quad \mathrm{Tr}\,[\not{p}_e\gamma_{\mu'}\not{p}'_e\gamma_{\nu'}]\,\mathrm{Tr}\,[\,(-\not{p}_A)\gamma_\mu(\not{q}-\not{p}_A)\gamma_\alpha\not{p}_B\gamma_\nu(\not{p}_B-\not{q})\gamma_\beta]\,\mathrm{Tr}\,(\not{P}\gamma_{\alpha'}\not{P}'\gamma_{\beta\prime}) \\
&= -\frac{e^4e_q^2}{4Q^4(x_{I\!P}P)^4tu}\,2[4p_e{}^\mu p_e{}^\nu - Q^2g^{\mu\nu}]\,4x_{I\!P}m_P^2g^{\alpha\beta} \\
&\quad \mathrm{Tr}\,(\not{p}_A\gamma_\mu(\not{q}-\not{p}_A)\gamma_\alpha\not{p}_B\gamma_\nu(\not{p}_B-\not{q})\gamma_\beta) \\
&= -\frac{2e^4e_q^2}{Q^4m_P^2x_{I\!P}{}^3tu}\,[4p_e{}^\mu p_e{}^\nu - Q^2g^{\mu\nu}]\,\mathrm{Tr}\,(\not{p}_A\gamma_\mu(\not{q}-\not{p}_A)\gamma_\alpha\not{p}_B\gamma_\nu(\not{p}_B-\not{q})\gamma^\alpha)
\end{aligned}$$

non-invariance of these models. In the single-gluon exchange model, the mass term in the completeness relation cannot be neglected.

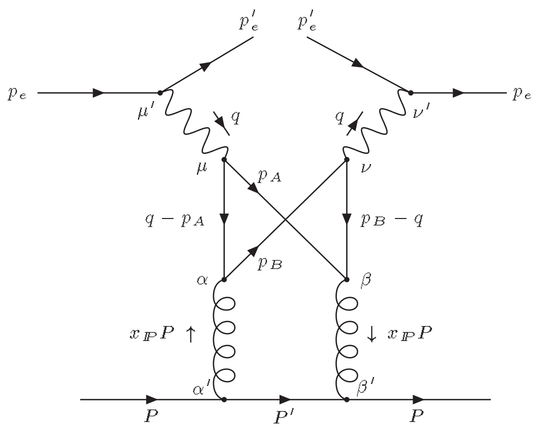

Figure B.6: *Contribution to the first mixed term in the single-gluon exchange model matrix element.*

$$
\begin{aligned}
&= -\frac{2e^4 e_q^2}{Q^4 m_P^2 x_{I\!P}{}^3 tu} \left[4 p_e{}^{\mu} p_e{}^{\nu} - Q^2 g^{\mu\nu}\right] \mathrm{Tr}\left(\not{p}_A \gamma_\mu (\not{q} - \not{p}_A) \gamma_\alpha \not{p}_B \gamma_\nu (\not{p}_B - \not{q}) \gamma^\alpha\right) \\
&= \frac{2^2 e^4 e_q^2}{Q^4 m_P^2 x_{I\!P}{}^3 tu} \left[4 p_e{}^{\mu} p_e{}^{\nu} - Q^2 g^{\mu\nu}\right] \mathrm{Tr}\left[\not{p}_A \gamma_\mu (\not{q} - \not{p}_A)(\not{p}_B - \not{q}) \gamma_\nu \not{p}_B\right] \\
&= \frac{2^2 e^4 e_q^2}{Q^4 m_P^2 x_{I\!P}{}^3 tu} \Big\{ 4\,\mathrm{Tr}\left[\not{p}_A \not{p}_e (\not{q} - \not{p}_A)(\not{p}_B - \not{q}) \not{p}_e \not{p}_B\right] - Q^2\,\mathrm{Tr}\left[\not{p}_A \gamma_\mu (\not{q} - \not{p}_A)(\not{p}_B - \not{q}) \gamma^\mu \not{p}_B\right] \Big\} \\
&= \frac{2^2 e^4 e_q^2}{Q^4 m_P^2 x_{I\!P}{}^3 tu} \Big\{ 4\,\mathrm{Tr}\left[\not{p}_A \not{p}_e (\not{q} - \not{p}_A)(\not{p}_B - \not{q}) \not{p}_e \not{p}_B\right] - Q^2 4 (q - p_A) \cdot (p_B - q)\,\mathrm{Tr}\left[\not{p}_A \not{p}_B\right] \Big\} \\
&= \frac{2^2 e^4 e_q^2}{Q^4 m_P^2 x_{I\!P}{}^3 tu} \Big\{ 4\,\mathrm{Tr}\left[\not{p}_A \not{p}_e (\not{q} - \not{p}_A)(\not{p}_B - \not{q}) \not{p}_e \not{p}_B\right] - Q^2 2^4 (q - p_A) \cdot (p_B - q)\, p_A \cdot p_B \Big\},
\end{aligned}
\tag{B.3.34}
$$

where

$$
\begin{aligned}
(q - p_A) \cdot (p_B - q) &= (q \cdot p_B + q \cdot p_A - p_A \cdot p_B - q^2) \\
&= (-\frac{1}{2}(u + Q^2) - \frac{1}{2}(t + Q^2) - \frac{s}{2} + Q^2) \\
&= (-\frac{1}{2}(u + 2Q^2 + t + s) + Q^2) \\
&= (\frac{1}{2} Q^2),
\end{aligned}
\tag{B.3.35}
$$

so that

$$
\overline{|\mathcal{M}_{12}|} = \frac{2^4 e^4 e_q^2}{Q^4 m_P^2 x_{I\!P}{}^3 tu} \Big\{ \mathrm{Tr}\left[\not{p}_A \not{p}_e (\not{q} - \not{p}_A)(\not{p}_B - \not{q}) \not{p}_e \not{p}_B\right] - Q^4 M_X^2 \Big\}. \tag{B.3.36}
$$

The other term is obtained by interchanging p_A and p_B as well as t and u in Eq. B.3.36 and is equal to $\overline{|\mathcal{M}_{12}|}$.

The squared matrix element for diffractive electron–proton scattering via the exchange of a single hard gluon is, therefore,

$$\begin{aligned}
\overline{|\mathcal{M}|}^2 &= \frac{2^4 e^4 e_q^2}{Q^4 m_P^2 t x_{I\!P}{}^3}\left(4\, p_e\cdot p_A\, x_{I\!P} S_{\rm Tot} - Q^2 u\right) + \\
&\quad \frac{2^4 e^4 e_q^2}{Q^4 m_P^2 u x_{I\!P}{}^3}\left(4\, p_e\cdot p_B\, x_{I\!P} S_{\rm Tot} - Q^2 t\right) + \\
&\quad \frac{2^4 e^4 e_q^2}{Q^4 m_P^2 x_{I\!P}{}^3 t u}\left\{ 2{\rm Tr}\left[\not{p}_A \not{p}_e (\not{q}-\not{p}_A)(\not{p}_B-\not{q})\not{p}_e \not{p}_B\right] - 2Q^4 M_X^2\right\} \\
&= \frac{2^4 e^4 e_q^2}{Q^4 m_P^2 x_{I\!P}{}^3}\left\{4 x_{I\!P} S_{\rm Tot}\left(\frac{p_e\cdot p_A}{t}+\frac{p_B\cdot p_e}{u}\right) - Q^2\left(\frac{u}{t}+\frac{t}{u}\right)\right. \\
&\quad \left. -2\frac{Q^2 M_X^2}{tu} + 2{\rm Tr}\left[\not{p}_A \not{p}_e (\not{q}-\not{p}_A)(\not{p}_B-\not{q})\not{p}_e \not{p}_B\right]\right\}. \qquad \text{(B.3.37)}
\end{aligned}$$

Expanding this expression further leads to a large number of terms, the result of which is not reproduced here.

Combining the matrix element with the electron–proton scattering flux factor and the full phase space element gives the full single-gluon exchange model diffractive scattering cross section

$$\begin{aligned}
{\rm d}\sigma &= \frac{1}{2S_{\rm Tot}}\frac{{\rm d}Q^2 {\rm d}M_X^2 {\rm d}p_\perp^2 {\rm d}x_{I\!P} {\rm d}t_{I\!P} {\rm d}\phi}{2^5(2\pi)^6 x_{I\!P} S_{\rm Tot} M_X^2}\frac{1}{\sqrt{1-\frac{4p_\perp^2}{M_X^2}}}\frac{2^4 e^4 e_q^2}{Q^4 m_P^2 x_{I\!P}{}^3}\left\{4 x_{I\!P} S_{\rm Tot}\cdot\right. \\
&\quad \left(\frac{p_e\cdot p_A}{t}+\frac{p_B\cdot p_e}{u}\right) - Q^2\left(\frac{u}{t}+\frac{t}{u}\right) - 2\frac{Q^2 M_X^2}{tu} + \\
&\quad \left. 2{\rm Tr}\left[\not{p}_A \not{p}_e (\not{q}-\not{p}_A)(\not{p}_B-\not{q})\not{p}_e \not{p}_B\right]\right\} \\
&= \frac{{\rm d}Q^2 {\rm d}M_X^2 {\rm d}p_\perp^2 {\rm d}x_{I\!P} {\rm d}t_{I\!P} {\rm d}\phi}{2^2(2\pi)^6 m_P^2 x_{I\!P}{}^4 S_{\rm Tot}{}^2 M_X^2 Q^4}\frac{e^4 e_q^2}{\sqrt{1-\frac{4p_\perp^2}{M_X^2}}}\left\{4 x_{I\!P} S_{\rm Tot}\left(\frac{p_e\cdot p_A}{t}+\frac{p_B\cdot p_e}{u}\right) - \right. \\
&\quad \left. Q^2\left(\frac{u}{t}+\frac{t}{u}\right) - 2\frac{Q^2 M_X^2}{tu} + 2{\rm Tr}\left[\not{p}_A \not{p}_e (\not{q}-\not{p}_A)(\not{p}_B-\not{q})\not{p}_e \not{p}_B\right]\right\}. \qquad \text{(B.3.38)}
\end{aligned}$$

After an integral is performed over the quark azimuthal angle, the single-gluon exchange model cross section can be factorized in a similar way to the form factor model approach.

B.3.5 Scalar-Pomeron Model

Vermaseren *et al* [48] calculated the cross section for electron–pomeron deep-inelastic scattering, in which the pomeron couples to quarks and gluons with scalar couplings. The cross section for the dijet component of diffractive DIS is given by (with some typographical errors from [48] corrected)

$$\begin{aligned}
{\rm d}\sigma^{eI\!P} &= \frac{{\rm d}^3\underline{p}_A}{2p_A{}^0}\frac{{\rm d}^3\underline{p}_B}{2p_B{}^0}\frac{{\rm d}^3\underline{p}'_e}{2p'^0_e}\,\delta^4(p_e + P_{I\!P} - p_A - p_B - p'_e) \\
&\quad \left[q^2\,\frac{(M_X^2-q^2)^2+P_{I\!P}^4}{ut} - P_{I\!P}^2 (q^2)^2\left(\frac{1}{u^2}+\frac{1}{t^2}\right)\right. \\
&\quad -8P_{I\!P}\cdot p_e\left(\frac{1}{u}+\frac{1}{t}\right)\left\{\frac{p_e\cdot p_A\,(P_{I\!P}^2-t)}{t}+\frac{p_e\cdot p_B\,(P_{I\!P}^2-u)}{u}\right\}
\end{aligned}$$

$$+ \, 8\frac{(P_{I\!P} \cdot p_e)^2 M_X^2}{u\,t} + 8 p_A \cdot p_e \, p_B \cdot p_e \, P_{I\!P}^2 \left(\frac{1}{u} + \frac{1}{t}\right)^2 \Bigg]$$

$$\frac{(2\pi)^4}{(2\pi)^9} \, 2^2 \, \frac{1}{2(s_T - P_{I\!P}^2)} \, \frac{e_q^2 \, e^4 \, g_{I\!Pqq}^2}{Q^4} \,, \tag{B.3.39}$$

where $P_{I\!P} = x_{I\!P} P$ is the pomeron momentum, $g_{I\!Pqq}$ is the coupling constant at the quark–antiquark–pomeron vertex and $s_{\mathrm{T}} = x_{I\!P} S_{\mathrm{Tot}}$ is the electron–pomeron CMS energy. This cross section must be summed over contributing (light) quark flavours of fractional charge ee_q.

Extending this result to electron–proton diffractive deep-inelastic scattering, the contribution to the final state phase space element from the outgoing proton is included, the δ-function is altered to conserve total momentum and the flux factor is also altered from $(x_{I\!P} S_{\mathrm{Tot}} - P_{I\!P}^2)$ to $(S_{\mathrm{Tot}} - m_P^2)$. Unlike the case of vector quark–pomeron coupling models, the scalar-pomeron structure function scales without the need for form factors. For the pomeron–proton vertex, a point-like scalar coupling is assumed between the pomeron and (valence) quarks and a factor of $3F_1(t_{I\!P})$ is included for each proton coupling to a pomeron. The contribution from the proton–pomeron coupling and the trace at the proton vertex in the scalar-pomeron model is

$$\begin{aligned} \frac{1}{2} \left[g_{I\!Pqq} 3F_1(t_{I\!P})\right]^2 \mathrm{Tr}\left[\not{P} \not{P}'\right] &= \frac{1}{2} \left[3 g_{I\!Pqq} F_1(t_{I\!P})\right]^2 4P \cdot P' \\ &\approx 2[3 g_{I\!Pqq} F_1(t_{I\!P})]^2 m_P^2 \,, \end{aligned} \tag{B.3.40}$$

where the factor of $1/2$ is from averaging over the spins of incoming protons. The final step in this calculation is to modify the $x_{I\!P}$ dependence by hand to ${x_{I\!P}}^{1-2\alpha_{I\!P}(0)}$ to take into account the observed Regge behaviour of the diffractive scattering total cross section.

The scalar-pomeron cross section, with full electron–proton phase space and flux factor, is

$$\begin{aligned} \mathrm{d}\sigma = \; & \frac{\mathrm{d}^3 \underline{p}_A}{2{p_A}^0} \frac{\mathrm{d}^3 \underline{p}_B}{2{p_B}^0} \frac{\mathrm{d}^3 \underline{p}'_e}{2{p'_e}^0} \frac{\mathrm{d}^3 \underline{P}'}{2P'^0} \, \delta^4(p_e + P' - p_A - p_B - p'_e) \\ & \Bigg[-Q^2 \, \frac{(Q^2 + M_X^2)^2 - P_{I\!P}^4}{u\,t} + \\ & P_{I\!P}^2 Q^4 \left(\frac{1}{u^2} + \frac{1}{t^2}\right) - 8 P_{I\!P} \cdot p_e \left(\frac{1}{u} + \frac{1}{t}\right) \\ & \left\{ \frac{p_e \cdot p_A \, (P_{I\!P}^2 - t)}{t} + \frac{p_e \cdot p_B \, (P_{I\!P}^2 - u)}{u} \right\} \\ & + \, 8\frac{(P_{I\!P} \cdot p_e)^2 M_X^2}{u\,t} + 8 p_A \cdot p_e \, p_B \cdot p_e \, P_{I\!P}^2 \left(\frac{1}{u} + \frac{1}{t}\right)^2 \Bigg] \\ & \frac{(2\pi)^4}{(2\pi)^{12}} \, 2^2 \, \frac{9 e_q^2 \, e^4 \, g_{I\!Pqq}^4 [F_1(t_{I\!P})]^2 m_P^2}{Q^4 (S_{\mathrm{Tot}} - m_P^2)} \,. \end{aligned} \tag{B.3.41}$$

Neglecting terms of order $P_{I\!P}^2 = m_P^2 {x_{I\!P}}^2$ gives (for $S_{\mathrm{Tot}} >> m_P^2$)

$$\begin{aligned} \mathrm{d}\sigma = \; & \frac{\mathrm{d}^3 \underline{p}_A}{2{p_A}^0} \frac{\mathrm{d}^3 \underline{p}_B}{2{p_B}^0} \frac{\mathrm{d}^3 \underline{p}'_e}{2{p'_e}^0} \frac{\mathrm{d}^3 \underline{P}'}{2P'^0} \, \delta^4(p_e + P' - p_A - p_B - p'_e) \left[-Q^2 \, \frac{(Q^2 + M_X^2)^2}{u\,t} \right. \\ & \left. + 8 P_{I\!P} \cdot p_e \left(\frac{1}{u} + \frac{1}{t}\right) (p_e \cdot p_A + p_e \cdot p_B) + 8\frac{(x_{I\!P} P \cdot p_e)^2 M_X^2}{u\,t} \right] \end{aligned}$$

$$
\begin{aligned}
&\frac{36e^4 e_q^2\, g_{\mathit{IP}qq}^4 [F_1(t_{\mathit{IP}})]^2 m_P^2}{(2\pi)^8 Q^4 S_{\mathrm{Tot}}} \\
&= \frac{\mathrm{d}^3\underline{p}_A}{2p_A{}^0}\frac{\mathrm{d}^3\underline{p}_B}{2p_B{}^0}\frac{\mathrm{d}^3\underline{p}'_e}{2p'_e{}^0}\frac{\mathrm{d}^3\underline{P}'}{2P'^0}\delta^4(p_e+P'-p_A-p_B-p'_e)\frac{1}{ut}\left[-Q^2(Q^2+M_X^2)^2\right. \\
&\left. -8\frac{x_{\mathit{IP}} S_{\mathrm{Tot}}}{2}(Q^2+M_X^2)\left(\frac{x_{\mathit{IP}} S_{\mathrm{Tot}}}{2}-\frac{Q^2}{2}\right)+2\frac{x_{\mathit{IP}}{}^2 S_{\mathrm{Tot}}{}^2 M_X^2}{ut}\right] \\
&\frac{36e^4 e_q^2\, g_{\mathit{IP}qq}^4 [F_1(t_{\mathit{IP}})]^2 m_P^2}{(2\pi)^8 Q^4 S_{\mathrm{Tot}}} \\
&= \frac{\mathrm{d}Q^2\mathrm{d}M_X^2\mathrm{d}p_\perp^2\mathrm{d}x_{\mathit{IP}}\mathrm{d}t_{\mathit{IP}}\mathrm{d}\phi}{2^5(2\pi)^6 9m_P^2[F_1(t_{\mathit{IP}})]^2 M_X^2 Q^2}\;\frac{e^4 e_q^2 g_{\mathit{IP}qq}^4 x_{\mathit{IP}}\,(Q^2+M_X^2)}{\sqrt{1-\frac{4p_\perp^2}{M_X^2}}}[1+(1-y)^2]\,,
\end{aligned}
\tag{B.3.42}
$$

from which it can be seen that the diffractive structure function is entirely transverse. In the scalar-pomeron model calculations, an integral over the t_{IP}-dependence is assumed, which introduces a dimensionful constant into the overall normalisation[2], and the pomeron trajectory is replaced by the pomeron intercept $\alpha_{\mathit{IP}}(0)$.

The diffractive structure function can be read off from Eq. B.3.42. There is little difference in the Q^2 or β dependence of the diffractive structure function if the $p_\perp^2$ range is restricted by pseudo-rapidity gap data selection cuts from the unrestricted diffractive structure function.

B.3.6 Two-Gluon Model

Diehl [35,36,68] has calculated the cross section for diffractive lepton–proton scattering in the Landshoff-Nachtmann two-gluon model [34]. In this approach, the exchanged colour-singlet state is modelled by two non-interacting gluons with non-perturbative propagators. The cross section has been calculated by putting the strong coupling constant at scale $p_\perp^2$ in Diehl's calculations [35] equal to $\alpha_s(0)$ and assuming a sum over light quark flavours and is given by

$$
\begin{aligned}
\frac{\mathrm{d}^3\sigma_{T,L}}{\mathrm{d}t_{\mathit{IP}}\mathrm{d}x_{\mathit{IP}}\mathrm{d}p_\perp^2} &= \frac{16}{3}\alpha_{\mathrm{em}} e_q^2 x_{\mathit{IP}}{}^{1-2\alpha_{\mathit{IP}}(t_{\mathit{IP}})}[F_1(t_{\mathit{IP}})]^2\,\frac{1}{Q^2+M_X^2}\,\frac{1}{\sqrt{1-\frac{4(p_\perp^2+m_q^2)}{M_X^2}}}\mathcal{I}_{T,L} \\
&= \frac{9\alpha_{\mathrm{em}} e_q^2\beta_0^2}{Q^2}\,[F_1(t_{\mathit{IP}})]^2 x_{\mathit{IP}}{}^{1-2\alpha_{\mathit{IP}}(t_{\mathit{IP}})} F_{T,L}^{\mathit{IP}}(Q^2,\beta)\,,
\end{aligned}
\tag{B.3.43}
$$

where, for $p_{\perp\,\mathrm{min}}^2 \gtrsim 1\,\mathrm{GeV}^2$, $\mathcal{I}_T$ and $\mathcal{I}_L$ are

$$
\begin{aligned}
\mathcal{I}_T \approx\; & \frac{81\beta_0^4\mu_0^4}{16\pi^2}\,\frac{M_X^2}{(Q^2+M_X^2)^2}\,\frac{1}{(p_\perp^2+m_q^2)^2} \\
& \left\{\left(1-2\frac{p_\perp^2+m_q^2}{M_X^2}\right)\frac{p_\perp^2}{p_\perp^2+m_q^2}\left(1-\frac{M_X^2}{Q^2+M_X^2}\,\frac{p_\perp^2}{p_\perp^2+m_q^2}\right)^2\right. \\
& \left.+\frac{1}{4}\,\frac{m_q^2}{p_\perp^2+m_q^2}\left(1-2\frac{M_X^2}{Q^2+M_X^2}\,\frac{p_\perp^2}{p_\perp^2+m_q^2}\right)^2\right\}\,, \\
\mathcal{I}_L \approx\; & \frac{81\beta_0^4\mu_0^4}{16\pi^2}\,\frac{Q^2}{(Q^2+M_X^2)^2}\,\frac{1}{p_\perp^2+m_q^2}\left(1-2\frac{M_X^2}{Q^2+M_X^2}\,\frac{p_\perp^2}{p_\perp^2+m_q^2}\right)^2\,.
\end{aligned}
$$

[2] See Sect. 3.8.2 for a discussion of the t_{IP} integration.

$$(B.3.44)$$

Here m_q is the (light) quark mass (which can be neglected for large $p^2_{\perp\,\mathrm{min}}$ data with little loss of accuracy) and $\mu_0 \approx 1.2\,\mathrm{GeV}$. Neglecting the quark masses,

$$\begin{aligned}
\mathcal{I}_T &\approx \frac{81\beta_0^4\mu_0^4}{16\pi^2}\frac{Q^4M_X^2}{(Q^2+M_X^2)^4}\frac{1}{p_\perp^4}\left(1-2\frac{p_\perp^2}{M_X^2}\right), \\
\mathcal{I}_L &\approx \frac{81\beta_0^4\mu_0^4}{16\pi^2}\frac{1}{p_\perp^2}\frac{Q^2(Q^2-M_X^2)}{(Q^2+M_X^2)^3}\,.
\end{aligned} \tag{B.3.45}$$

The transverse and longitudinal contributions to the pomeron structure function are therefore (for $p^2_{\perp\,\mathrm{min}} >$ a few GeV^2)

$$\begin{aligned}
F_T^{I\!P} &= \int_{p_\perp^2}\frac{16\beta}{27\beta_0^2}\frac{1}{\sqrt{1-\frac{4p_\perp^2}{M_X^2}}}\mathcal{I}_T \\
&\approx \int_{p_\perp^2}\frac{3\beta_0^2\mu_0^4\beta^3}{\pi^2(Q^2+M_X^2)^2}\frac{1}{\sqrt{1-\frac{4p_\perp^2}{M_X^2}}}\frac{1}{p_\perp^4}\left(M_X^2-2p_\perp^2\right) \\
&\approx \frac{3\beta_0^2\mu_0^4\beta^4(1-\beta)}{\pi^2Q^2}\frac{1}{p^2_{\perp\,\mathrm{min}}}, \\
F_L^{I\!P} &= \int_{p_\perp^2}\frac{16\beta}{27\beta_0^2}\frac{1}{\sqrt{1-\frac{4p_\perp^2}{M_X^2}}}\mathcal{I}_L \\
&\approx \int_{p_\perp^2}\frac{3\beta_0^2\mu_0^4\beta^2}{\pi^2}\frac{1}{\sqrt{1-\frac{4p_\perp^2}{M_X^2}}}\frac{1}{p_\perp^2}\frac{(Q^2-M_X^2)}{(Q^2+M_X^2)^2} \\
&\approx \frac{3\beta_0^2\mu_0^4\beta^3(1-2\beta)}{\pi^2Q^2}\ln\left[\frac{Q^2}{4\beta p^2_{\perp\,\mathrm{min}}}(1-\beta)\right].
\end{aligned} \tag{B.3.46}$$

This is the strong β dependence which is visible in Figs. 4.3 and 4.6 in Chap. 4. If the $p^2_{\perp\,\mathrm{min}}$ cut is removed, the Landshoff-Nachtmann two-gluon model has the same β behaviour in the structure function as the Donnachie-Landshoff form factor model [35], namely

$$F_2^{I\!P} \sim \beta(1-\beta)\,. \tag{B.3.47}$$

Bibliography

[1] J. Ellis, G. G. Ross, and J. Williams, Eur. Phys. J. **C10**, 443 (1999).

[2] J. Ellis and G. G. Ross, Phys. Lett. **B384**, 293 (1996).

[3] J. Williams, Prepared for Workshop on Monte Carlo Generators for HERA Physics (Plenary Starting Meeting), Hamburg, Germany, 27-30 Apr 1998.

[4] J. Williams, Nucl.Phys.B.Proc.Suppl. **79**, 305 (1999).

[5] J. C. Williams, hep-ph/9910322.

[6] R. G. Roberts, *The Structure of the Proton: Deep Inelastic Scattering* (Cambridge University Press, Cambridge, England, 1993).

[7] F. Halzen and A. D. Martin, *Quarks and Leptons: An Introductory Course in Modern Particle Physics* (Wiley, New York, USA, 1984).

[8] H1, I. Abt *et al.*, Nucl. Instrum. Meth. **A386**, 310 (1997).

[9] ZEUS, ZEUS-STATUS-REPT-1993.

[10] ZEUS, M. Derrick *et al.*, Phys. Lett. **B315**, 481 (1993).

[11] ZEUS, M. Derrick *et al.*, Phys. Lett. **B332**, 228 (1994).

[12] H1, T. Ahmed *et al.*, Nucl. Phys. **B429**, 477 (1994).

[13] H1, T. Ahmed *et al.*, Phys. Lett. **B348**, 681 (1995).

[14] ZEUS, J. Breitweg *et al.*, Eur. Phys. J. **C1**, 81 (1998).

[15] H1, C. Adloff *et al.*, Z. Phys. **C76**, 613 (1997).

[16] H1, T. Ahmed *et al.*, Nucl. Phys. **B435**, 3 (1995).

[17] A. D. Martin, R. G. Roberts, W. J. Stirling, and R. S. Thorne, hep-ph/9805205.

[18] P. D. B. Collins, Phys. Rep. **1C**, 103 (1971).

[19] P. D. B. Collins, *An Introduction to Regge Theory and High Energy Physics* (Cambridge University Press, Cambridge, England, 1978).

[20] A. D. Martin and T. D. Spearman, *Elementary Particle Theory* (North-Holland, Amsterdam, 1970).

[21] WA91, S. Abatzis *et al.*, Phys. Lett. **B324**, 509 (1994).

[22] P. V. Landshoff and J. C. Polkinghorne, Nucl. Phys. **B32**, 541 (1971).

[23] G. A. Jaroszkiewicz and P. V. Landshoff, Phys. Rev. **10**, 170 (1974).

[24] A. Donnachie and P. V. Landshoff, Nucl. Phys. **B231**, 189 (1984).

[25] A. Donnachie and P. V. Landshoff, Nucl. Phys. **B244**, 322 (1984).

[26] A. Donnachie and P. V. Landshoff, Nucl. Phys. **B267**, 690 (1986).

[27] A. Donnachie and P. V. Landshoff, Phys. Lett. **B296**, 227 (1992).

[28] This figure was taken from the official ZEUS events site maintained by Nicolo Cartiglia `http://www-zeus.desy.de/~ nicolo/diffr/diagrams.html`.

[29] G. Ingelman and P. E. Schlein, Phys. Lett. **152B**, 256 (1985).

[30] F. E. Low, Phys. Rev. **D12**, 163 (1975).

[31] S. Nussinov, Phys. Rev. Lett. **34**, 1286 (1975).

[32] S. Nussinov, Phys. Rev. **D14**, 246 (1976).

[33] N. Nikolaev and B. G. Zakharov, Z. Phys. **C53**, 331 (1992).

[34] P. V. Landshoff and O. Nachtmann, Z. Phys. **C35**, 405 (1987).

[35] M. Diehl, Z. Phys. **C66**, 181 (1995).

[36] M. Diehl, Eur. Phys. J. **C6**, 503 (1999).

[37] M. Genovese, N. N. Nikolaev, and B. G. Zakharov, J. Exp. Theor. Phys. **81**, 625 (1995).

[38] J. Bartels, C. Ewerz, H. Lotter, M. Wusthoff, and M. Diehl, hep-ph/9609239.

[39] J. Bartels, H. Lotter, and M. Wusthoff, Phys. Lett. **B379**, 239 (1996).

[40] A. Bialas and R. Peschanski, Phys. Lett. **B378**, 302 (1996).

[41] E. Gotsman, E. Levin, and U. Maor, Nucl. Phys. **B493**, 354 (1997).

[42] W. Buchmüller and A. Hebecker, Phys. Lett. **B355**, 573 (1995).

[43] W. Buchmüller and A. Hebecker, hep-ph/9506447.

[44] Y. Y. Balitskii and L. N. Lipatov, Sov. J. Nucl. Phys. **28**, 822 (1978).

[45] E. A. Kuraev, L. N. Lipatov, and V. S. Fadin, Sov. Phys. JETP **44**, 443 (1976).

[46] A. Donnachie and P. V. Landshoff, Phys. Lett. **185B**, 403 (1987).

[47] A. Donnachie and P. V. Landshoff, Phys. Lett. **191B**, 309 (1987).

[48] J. Vermaseren, F. Barreiro, L. Labarga, and F. J. Yndurain, Phys. Lett. **B418**, 363 (1998).

[49] H1, C. Adloff *et al.*, Eur. Phys. J. **C1**, 495 (1998).

[50] S. Wolfram, *The Mathematica Book*, 3 ed. (Wolfram Media (Il. USA) and Cambridge University Press, Cambridge, England, 1996).

[51] R. Mertig, M. Bohm, and A. Denner, Comput. Phys. Commun. **64**, 345 (1991).

[52] J. Vermaseren, Axodraw, available from `http://norma.nikhef.nl/~ t68/axodraw/`.

[53] ZEUS, M. Derrick *et al.*, Z. Phys. **C68**, 569 (1995).

[54] ZEUS, J. Breitweg *et al.*, Phys. Lett. **B421**, 368 (1998).

[55] ZEUS, J. Breitweg *et al.*, Eur. Phys. J. **C6**, 43 (1999).

[56] A. Donnachie and P. V. Landshoff, Phys. Lett. **B437**, 408 (1998).

[57] J. P. Phillips, *The Deep-Inelastic Structure of Diffraction*, PhD thesis, University of Manchester, 1995, available from `http://www-h1.desy.de/h1/www/h1work/dif/publications.html`.

[58] M. Wusthoff, Phys. Rev. **D56**, 4311 (1997).

[59] J. Bartels, J. Ellis, H. Kowalski, and M. Wusthoff, Eur. Phys. J. **C7**, 443 (1999).

[60] J. Bartels and C. Royon, Mod. Phys. Lett. **A14**, 1583 (1999).

[61] J. Bartels, H. Jung, and M. Wusthoff, Eur. Phys. J. **C11**, 111 (1999).

[62] ZEUS, M. Derrick *et al.*, Z. Phys. **C70**, 391 (1996).

[63] F. Hautmann, Z. Kunszt, and D. E. Soper, Phys. Rev. Lett. **81**, 3333 (1998).

[64] J. Forshaw and D. A. Ross, *The QCD Pomeron* (Cambridge University Press, Cambridge, England, 1997).

[65] V. S. Fadin and L. N. Lipatov, Phys. Lett. **B429**, 127 (1998).

[66] V. S. Fadin, hep-ph/9807527.

[67] J. Bartels, Private communication.

[68] M. Diehl, *Diffraction in Electron–Proton Collisions*, PhD thesis, Darwin College, Cambridge, 1996.

[69] J. C. Collins, Phys. Rev. **D57**, 3051 (1998).

[70] J. Forshaw, Private communication.

[71] N. N. Nikolaev, hep-ph/9905562.